THERMAL RADIATION FROM ISOLATED NEUTRON STARS: SPECTRA AND POLARIZATIONS

A Dissertation

Presented to the Faculty of the Graduate School

of Cornell University

in Partial Fulfillment of the Requirements for the Degree of

Doctor of Philosophy

by

Matthew Isaac van Adelsberg

January 2007

THERMAL RADIATION FROM ISOLATED NEUTRON STARS: SPECTRA AND POLARIZATIONS

Matthew Isaac van Adelsberg, Ph.D.

Cornell University 2007

Recent observations of surface emission from isolated neutron stars (NSs) provide unique challenges to theoretical modeling of thermal radiative processes. We construct models of thermal emission from strongly magnetized NSs in which the outermost layer of the NS is in a condensed liquid or solid form, or is an ionized H or He atmosphere.

We calculate the emission properties (spectrum and polarization) of NSs with condensed Fe and H surfaces using a generalized form of Kirchhoff's Law, in the regimes where condensation may be possible. For smooth condensed surfaces, the overall emission is reduced from blackbody by less than a factor of two. The spectrum exhibits modest deviation from blackbody across a wide energy range, and shows mild absorption features associated with the electron plasma and ion cyclotron frequencies in the condensed matter. The roughness of the solid Fe condensate decreases the reflectivity of the surface, making the emission spectrum even closer to blackbody.

We provide an accurate treatment of vacuum polarization effects in magnetized NS atmosphere models. We treat the conversion of photon modes (due to "vacuum resonance" between plasma and vacuum polarizations), employing both the modal radiative transfer equations (coupled with an accurate mode conversion

probability at the vacuum resonance) and the full radiative transfer equations for the photon Stokes parameters. We are able to quantitatively calculate the atmosphere structure, emission spectra, beam patterns, and polarizations for the range of magnetic field strengths $B = 10^{12} - 10^{15}$ G. In agreement with previous studies, we find that for NSs with magnetic field strengths $B/2 \gtrsim B_l \simeq 7 \times 10^{13}$ G, vacuum polarization reduces the widths of spectral features and softens the hard tail of magnetized atmosphere models. For $B \lesssim B_l/2$, vacuum polarization does not change the emission spectra, but can affect the polarization signals.

We investigate the propagation of photon polarization in NS magnetospheres, and show that vacuum polarization induces a unique energy-dependent linear polarization signature, and can generate circular polarization in the magnetospheres of rapidly rotating NSs. We discuss the implications of our results for observations of thermally emitting isolated NSs and magnetars, and the prospects for future spectral and polarization studies.

BIOGRAPHICAL SKETCH

Matthew Isaac van Adelsberg was born with a complicated last name in Glendale, California during the summer of 1979. In 1981, his parents, Rick and Gail, relocated the family to Hayward, California, which finished a close second to Oakland in the 1983 West Coast Crime Capital of the Year awards. Despite a heavy recruitment pitch from the A Street Gang, Matthew managed to finish his programs at Highland Elementary and Bret Harte Middle School, while simultaneously nurturing the world's worst haircut.

On impulse, Matthew's parents moved the family (which by this time included sister Stephanie) to Lima, Peru in August, 1993. The move proved to be one of the defining moments in Matthew's life, opening his eyes to a new culture, language, poverty, and geography. Attending high school at Franklin Delano Roosevelt American School opened a number of academic doors for the budding young scholar, yet Matthew also managed to find time to befriend a number of bad influences who would become life-long friends.

Matthew matriculated at Boston University in 1997, pursuing an eclectic program of study in acting at the School for Fine Arts. After spending a year reenacting the plot from *A Chorus Line*, he decided to broaden his college experience. Subsequent majors included: theatre studies, creative writing, history, psychology, pre-med, and archaeology. Upon learning that studying archaeology would not transform his life into an Indiana Jones film, he decided to pursue a burgeoning passion for science and study chemistry. In May, 2001, after graduating with a major in chemistry and a minor in physics, he chose to continue academic work in physics at Cornell University.

Matthew obtained his M.S. in astrophysics in April, 2005, and will be awarded

the degree of Ph.D. in January, 2007. Apart from his scientific work, he enjoys reading, writing, travel, dance, karaoke, soccer, basketball, and spending time with friends and family. In addition, he devotes much of his time to science outreach, in an attempt to fight for the forces of rationality, critical thinking, and the skeptical way.

This work is dedicated to Rick, Gail, and Stephanie van Adelsberg.

ACKNOWLEDGEMENTS

My parents have provided me with so much support during my five years in graduate school (and over the course of my life) that I cannot imagine having completed this work without them. I am unable to express my appreciation in words, and can only hope that they know how much they mean to me. And notice that I acknowledged them first.

Stephanie van Adelsberg has always been an incredible sister and a great listener. She is a true humanitarian who leads by example; I hate to think of the kind of person I would have been without her friendship.

Dong Lai was an exceptional thesis advisor, showing patience and a willingness to teach above and beyond the call of duty; he is extremely knowledgeable and committed to his students' development.

I wish I could say that my best friends helped me finish this dissertation. The reality is that I finished it in spite of their influence, which, all joking aside, has kept me sane since high school. To Tom "Tuna" Akers, Giancarlo "La Bestia" Baldino, Sandro "Alcahuete" Callirgos, Tim "Partyboy" Farris, Mike "The Silver Fox" Foley, Chris "Parlantes" Lee, and Trevor "T-Dogg" Vonnegut: I'm thankful and proud to call you guys my friends and my brothers. I know that I'd never be able to get rid of you, even if I wanted to.

Trev, Marci, Sam, and Jack van Adelsberg always provided me with a place to catch my breath during college and graduate school; I'm so fortuante to have them as friends and family. In fact, it was at their home that I first realized I wanted to study science!

My grandparents Michael and Beverle Singer, and Hetty van Adelsberg are wonderful people who have also provided me with an incredible amount of support

and confidence. They've enriched my life in too many ways to spell out here.

I'd also like to thank Wynn Ho, Sasha Potekhin, and the members of my Special Committee: Jim Cordes, Saul Teukolsky, and Ira Wasserman.

TABLE OF CONTENTS

LIST OF TABLES

LIST OF FIGURES

Chapter 1

Introduction

Neutron stars are a natural laboratory for studying exotic physics. Young, cooling neutron stars (NSs) provide a probe into matter compressed to super-nuclear densities. Putative NS interiors can obey a wide variety of equations of state, with varying stiffness or unconventional phases of quark or strange matter (see, e.g., Lattimer & Prakash, 2001). A wide range of predicted NS cooling histories exist due to uncertainties in neutrino production mechanisms in NS cores and ambiguities in the treatment of superfluid protons and neutrons throughout the interior (Lattimer et al., 1991; Prakash et al., 1992; Kaminker et al., 2002; Yakovlev et al., 2004). Many NSs have strong magnetic fields ($B \gtrsim B_Q \approx 4.4 \times 10^{13}$ G, where B_Q is the quantum critical field), in which QED effects directly influence radiation emitted from the NS surface (Gnedin et al., 1978; Ventura et al., 1979; Bulik & Miller, 1997; Heyl & Hernquist, 1997).

While observations of non-thermal emission from isolated pulsars and magnetars (see below) yield important information about the structure and radiative processes of NS magnetospheres, thermal radiation emerging directly from the surface can constrain the equation of state and cooling properties of a NS. For most observed NSs, non-thermal magnetospheric emission or the presence of accretion in binaries complicates the interpretation of thermal spectra. Nevertheless, semi-reliable effective surface temperatures have been derived from observational data for several pulsars and radio-quiet central compact objects in supernova remnants (see, e.g., Table 2 of Yakovlev & Pethick, 2004). These objects roughly fit basic models of NS cooling without superfluidity (Fig. 1 of Yakovlev & Pethick, 2004).

In addition, atmosphere modeling, coupled with identification of atomic transitions or cyclotron resonance in the NS emission spectrum, yields information about the NS M/R ratio. This information is combined with distance measurements (using parallax or identification with a star forming region) to constrain the NS radius. For a large range of masses the group of equation of state models predict a small range of radii that can be compared with observation (Lattimer & Prakash, 2001). Furthermore, timing measurements of the NS rotation period and its derivative are used to estimate the NS (dipole) magnetic field strength and characteristic age, while phase-resolved spectroscopy provides constraints on the magnetic field geometry and temperature distribution. Unfortunately, the procedures outlined above are complicated by discrepancies between atmosphere calculations and observations, as well as ambiguities in the identification of spectral features.

Observations of thermal emission from isolated NSs began in the early 1980s with the *Einstein* satellite, which detected thermal X-rays from several objects, including radio pulsars 1E 2259+586, PSR 1055-52, 1E 1048.1-5937, and PSR 0656+14 (see, e.g., the review by Ogelman, 1995). The ROSAT survey of the 1990s continued the search for soft X-ray sources. Several authors predicted the discovery of a population of old NSs accreting from the ISM (Treves & Colpi, 1991; Blaes & Madau, 1993). ROSAT and later missions did not identify this population of old accretors, instead locating seven dim, radio-quiet, thermal X-ray emitters, now referred to as X-ray dim isolated NSs (XDINSs; see Treves et al., 2000). These sources provide a unique opportunity to model thermal emission without complications from accretion or magnetospheric emission. Another population of NSs, the magnetars, was identified in the mid 1990s (Thompson & Duncan, 1995, 1996; Woods & Thompson, 2004). During quiescence, magnetars also emit

uncontaminated thermal spectra and are excellent candidates for the study of NS surfaces (see below).

In the last decade, the *XMM-Newton* and *Chandra* observatories have achieved significant improvements in the quality and quantity of data from radio pulsars, central compact objects in supernova remnants, XDINSs, and magnetar sources (for recent reviews, see Pavlov et al., 2004; Woods & Thompson, 2004; Haberl, 2005). The nature of these objects, and the percentage of the overall NS population represented by them, as well as possible evolutionary connections between magnetars, XDINSs, and pulsars are intriguing, unsolved questions. We review basic properties of thermal emission from these sources and highlight some of the observational puzzles that challenge current theoretical work.

1.1 Observations of Thermal Radiation from Isolated Neutron Stars

1.1.1 X-ray Dim Isolated Neutron Stars

The XDINS population consists of the seven nearby radio-quiet X-ray sources originally identified by the ROSAT survey.[1] Optical counterparts have been identified for several of these sources, and periodicity has been detected in all but two (RX J1856.5-3754 and RX J1605.3+3249). XDINS are characterized by long periods ($\sim 8.4 - 11.4$ s), large X-ray to optical flux ratios [$\log(f_X/f_O) \sim 3 - 5$], and nearly thermal soft X-ray spectra with temperatures $k_B T_{bb}^{\infty} \sim 50 - 120$ eV (where

[1]It has been suggested that the recently discovered population of Rotating Radio Transients is part of, or has connections to the XDINSs (see McLaughlin et al., 2006; Popov et al., 2006). Futher searches for isolated NS candidates are currently underway (see, e.g., Agüeros et al., 2006).

T_{bb}^{∞} is the effective blackbody temperature measured by the observer). Proper motion has been measured for three of the sources (Kaplan et al., 2002; Motch et al., 2003, 2005). The nature of XDINSs is unclear at present: they could be young cooling NSs, older NSs kept hot by accretion from the ISM, or magnetars and their descendents (van Kerkwijk & Kulkarni, 2001; Mori & Ruderman, 2003; Haberl, 2005), though the large proper velocities and optical observations tend to rule out the accretion hypothesis (Treves et al., 2000; Haberl, 2005).

Spectroscopic studies of the XDINSs initially revealed featureless, blackbody spectra (see, e.g., Paerels et al., 2001; Drake et al., 2002; Burwitz et al., 2003). However, recent observations have identified absorption features at $E \simeq 0.2 - 2$ keV from at least three of the sources: RX J0720.4-3125 (Haberl et al., 2004b), RX J1605.3+3249 (van Kerkwijk et al., 2004), RX J1308.6+2127 (Haberl et al., 2003), and possibly RX J0806.4-4123, RX J0420.0-5022 (Haberl et al., 2004a), and RX J2143.0+0654 (Zane et al., 2005). The equivalent widths (EWs) of these features vary strongly across the sources despite their similar effective temperatures (see Chapter 5). The identification of these features remains uncertain, due to degeneracies in the spectral flux between magnetic field strength and geometry, red shift, and the energies and EWs of electron or ion cyclotron lines and atomic transitions of H, He, or mid-Z atoms in strong magnetic fields (Ho & Lai, 2004; van Kerkwijk et al., 2004; Pavlov & Bezchastnov, 2005; Mori et al., 2005; Zane et al., 2005).

Of the ROSAT sources, RX J1856.5-3754 and RX J0720.4-3125 are the best studied. RX J1856.5-3754 was discovered by Walter et al. (1996), and observed extensively with *Chandra* and *XMM-Newton* (for an overview, see Burwitz et al., 2003). Its X-ray spectrum is fit by a blackbody with $k_B T_{bb}^{\infty} \approx 64$ eV (7×10^5 K).

No feature or variation in the X-ray flux has been detected (see the discussion in Chapter 2). Astrometric measurements yield a distance $d \approx 120$ pc (Kaplan et al., 2002).[2] The published distance and blackbody fit to the X-ray flux yields the NS radius at infinity $R_{bb}^{\infty} \approx 5$ km. If the emission is from the entire star surface, this value is puzzling, as it is smaller than the allowed radii for any baryonic NS equation of state.

A dim, thermal optical counterpart to RX J1856.5-3754 was identified by Walter & Matthews (1997). Fitting the entire spectrum with a single model is difficult, as extrapolation of the X-ray blackbody to low energies underpredicts the optical flux by a factor of six, while atmosphere fits to the X-ray data tend to overpredict the optical flux (see Zavlin & Pavlov, 2002, and the references therein). A successful fit to the spectrum of RX J1856.5-3754 can be achieved using a two-temperature blackbody model (Pons et al., 2002; Burwitz et al., 2003). In this case, the X-rays are emitted by a hot polar cap, while the optical photons emerge from the colder bulk of the NS. While this model provides an excellent fit to the observations, it is not obvious that this temperature profile is realistic, or why RX J1856.5-3754 emits as a perfect blackbody.

Another well-studied XDINS, RX J0720.4-3125, was identified by Haberl et al. (1997). Subsequent studies confirmed a thermal soft X-ray component with $k_B T_{bb}^{\infty} \approx 81$ eV (9×10^5 K), and identified an optical counterpart (see Haberl et al., 2004b, and the references therein). An absorption feature was detected by Haberl et al. (2003) at energy $E \sim 270$ eV, with a phase dependent EW ~ -40 eV. This phase dependence is of particular interest, as the EW of the feature and the hardness ratio of the phase-resolved spectra are anti-correlated with the pulse amplitude

[2]Note that a revised parallax will be available soon, correcting the distance to $d \approx 170$ pc (Kaplan, 2005).

maximum (Haberl et al., 2004b). A blackbody fit to the X-ray portion of the RX J0720.4-3125 spectrum underpredicts the optical flux by a factor of six, while atmosphere fits predict an excess, as in the case of RX J1856.5-3754. Kaplan et al. (2003) have identified a non-thermal component to the optical spectrum, which could be due to energy dependent absorption, or emission from the magnetosphere. It is clear that in the case of RX J0720.4-3125, a simple blackbody model is not sufficient to explain the optical data.

XDINS sources display great variability in their lightcurves: RX J1856.5-3754 and RX J1605+3249 show no pulsations, with pulse fractions constrained to within $\lesssim 1\%$ for the former (Burwitz et al., 2003), and $\lesssim 3\%$ for the latter (van Kerkwijk et al., 2004); RX J2143.7+0654 shows sinusoidal single-peaked pulsations ($P = 9.4$ s) with pulse fraction $\sim 4\%$ (Zane et al., 2005), though this result is unconfirmed; RX J0720-3125 shows sinusoidal single-peaked pulsations ($P = 3.39$ s) with pulse fraction $\sim 11\%$, the spectral hardness and line width both varying with the pulse phase (Haberl et al., 2004b); RX J0806.4-4123 and RX J0420.0-5022 show sinusoidal single-peaked pulsations ($P = 11.4$ s and $P = 3.5$ s) with pulse fractions $\sim 6\%$ and $\sim 13\%$, respectively, the spectral hardness of the latter varying with the pulse phase (Haberl et al., 2004a); and RX J1308+2127 shows double-peaked pulsations ($P = 10.3$ s) with pulse fraction $\sim 18\%$ (Haberl et al., 2003). Long-term spectral variations in RX J0720.4-3125 were recently reported by de Vries et al. (2004). This variation bears some similarity to that seen in certain AXPs, and is as yet unexplained, though a recent paper interprets it as precession of the NS spin axis (Haberl et al., 2006).

1.1.2 Magnetars

Anomalous X-ray Pulsars (AXPs) and Soft Gamma-ray Repeaters (SGRs) form two populations of isolated NSs with similar characteristics. There are five confirmed SGRs, all in the galactic plane (except for one source in the LMC). In quiescence, SGRs have a thermal soft X-ray component, with $k_B T_{bb}^{\infty} \sim 0.5 - 0.6$ keV, and a non-thermal hard X-ray power-law, with $\alpha_{ph} \sim 2-3$ ($F_\nu \propto \nu^{-\alpha_{ph}}$). Quiescent SGR luminosities range from $L_X \sim 0.8 - 3 \times 10^{35}$ erg s^{-1}. Three SGRs have confirmed pulsations, two observed during quiescence, with periods $P \sim 5 - 8$ s (Kouveliotou et al., 1998, 1999). Assuming standard magnetic dipole spin-down, SGRs have magnetic field strengths $B \lesssim 10^{15}$ G. Somewhat surprisingly, the observed thermal emission does not show any of the expected spectral features at these field strengths, such as the ion cyclotron line around 1 keV.

The characteristic features of SGRs are repeating, short, soft Gamma and X-ray bursts (with timescales $\sim$ 100 ms), which can have much larger luminosities ($\sim 10^{41}$ erg s^{-1}) than the quiescent emission. The burst spectra can be fit by a non-thermal power-law, modeled by optically thin bremsstrahlung ($k_B T^{\infty} \sim 20 - 50$ eV), and are typically harder than the quiescent spectra. (see GöğüŞ et al., 1999). Such bursting activity can follow years of quiescent emission. Occasionally, SGRs undergo giant bursts which achieve luminosities $L > 10^{44}$ erg s^{-1}; three such bursts have been observed: from SGR 0525-66 in March, 1979 (Evans et al., 1979), SGR 1900+14 in August, 1998 (Cline et al., 1998), and SGR 1806-20 in December, 2004 (Hurley et al., 2005).

There are five confirmed AXPs, all in the galactic plane. In quiescence, AXPs have a pulsed thermal soft X-ray component, with $k_B T_{bb}^{\infty} \sim 0.41 - 0.7$ keV, and a hard non-thermal power-law with $\alpha_{ph} \sim 2 - 3.6$. Quiescent AXP luminosities

range from $L_X \sim 10^{33} - 10^{35}$ erg s^{-1}. In addition, optical and IR counterparts to several AXPs have been discovered, as well as significant pulsed flux at ~ 100 keV from several of the sources (Israel et al., 2004; Kuiper et al., 2004, 2006). All AXPs are spinning down, with periods $P \sim 6 - 12$ s. Assuming standard dipole spin-down, AXPs have magnetic field strengths $B \sim 0.5 - 7 \times 10^{14}$ G. As in the SGR case, AXPs do not show any features in their thermal spectra. Recently, SGR-like bursts have been detected from AXP sources 1E 1048.1-5937 (Gavriil et al., 2002) and 1E 2259+586 (Kaspi et al., 2003).

SGRs and AXPs have a significantly high pulsed fraction, from 4-60% (rms) (see Table 14.2 of Woods & Thompson, 2004). The pulsed fraction is constant over the energy range 0.5-10 keV, while the contribution of the blackbody component relative to the total flux varies from 0-70%. Several AXPs and SGRs are associated with supernova remnants; for a summary of associations and inferred distances, see Table 14.4 of Woods & Thompson (2004). For comparisons of AXP and SGR properties, see Woods et al. (2002); Kulkarni et al. (2003); Kaspi (2004). For a recent review of magnetar properties, see Woods & Thompson (2004).

Both SGRs and AXPs have been identified as magnetars. In the magnetar model, the quiescent and burst luminosities are driven by the decay of super-strong magnetic fields with $B \gtrsim 10^{15}$ G in the NS interior (Duncan & Thompson, 1992; Paczynski, 1992; Thompson & Duncan, 1995, 1996). Several pieces of evidence provide support for the magnetar hypothesis (reviewed by Kaspi, 2004): (1) The energy required to produce SGR giant flares exceeds the energy available from rotation by many orders of magnitude, but is plausibly produced by the release of energy confined in a large magnetic field; (2) A large magnetic field is required to slow SGR 0525-66 to $P = 8$ s in 10^4 yrs (this age is inferred through

association with a supernova remnant); (3) Strong magnetic fields greatly reduce the Thomson cross-section of photon-electron scattering, allowing the observed super-Eddington flux from giant flares to escape from the NS; (4) Magnetic fields provide confinement of burst energy (for over several minutes) during the observed quasi-exponential decay of giant flares; (5) Rotation is insufficient to power quiescent AXP emission; (6) Decay of strong magnetic fields is consistent with the low inferred ages of AXPs from spin-down measurements; (7) AXPs exhibit bursting behavior similar to that observed in SGRs.

Thus, a variety of indirect evidence supports the hypothesis that magnetar sources are endowed with magnetic fields $B \gtrsim 10^{15}$ G, though there are currently no direct observations of these large fields. Recent observations of radio pulsars with magnetic fields strengths slightly less than those of the magnetar population demonstrate that the former sources are rotation-powered (i.e., their luminosities are less than the energy budget available from NS spin; see, e.g., McLaughlin et al., 2003). Therefore, magnetars and pulsars are differentiated by more than just the strength of their magnetic fields. One possibility is that they also differ in magnetic field structure; while magnetars may have the same dipole magnetic field as high field radio pulsars, they may in addition have a stronger quadrupole component.

Due to these uncertainties, the development of independent methods to measure properties of magnetar magnetic fields is extremely important. One promising method is the identification of transient spectral features, which have been observed during outburst in AXPs 1RXS J170849-400910 (Rea et al., 2003), and 1E 1048.1-5937 (Gavriil et al., 2002), and SGRs 1806-20 (Ibrahim et al., 2002, 2003), and 1900+14 (Strohmayer & Ibrahim, 2000). Identification of these features with proton cyclotron resonance implies magnetic field strengths roughly consistent with

those calculated from dipole spin-down, nevertheless, identification of these features remains ambiguous.

1.1.3 Pulsars and Central Compact Objects

The spectra of a number of radio pulsars (e.g., PSR B1055-52, B0656+14, Geminga and Vela) are observed to possess thermal components that can be attributed to emission from NS surfaces and, in some cases, heated polar caps (Becker & Pavlov, 2002). Phase-resolved spectroscopic observations constrain the surface magnetic field geometry and emission radius of the pulsar (see Caraveo et al., 2004; De Luca et al., 2005; Jackson & Halpern, 2005). The thermal emission from most radio pulsars is fit well by a blackbody, and is featureless (see, e.g., Marshall & Schulz, 2002).

Chandra has also uncovered a number of compact sources in supernova remnants with spectra consistent with thermal emission from NSs (see Pavlov & Zavlin, 2003), from which useful constraints on NS cooling physics have been obtained (Slane et al., 2002; Yakovlev & Pethick, 2004). A particularly interesting object is 1E 1207.4-5209, an isolated X-ray source lying in the supernova remnant G296.5+10.0. Timing studies have uncovered pulsations with $P = 0.424$ s (Zavlin et al., 1998), and an inferred magnetic field strength of $B \sim 3 \times 10^{12}$ G (Pavlov et al., 2002). Successful fits to the spectrum of 1E 1207.4-5209 have been achieved with both blackbody and H atmosphere models (Mori et al., 2005). 1E 1207.4-5209 is unique among isolated NSs in that it has two confirmed absorption features in its spectrum, at 0.7 and 1.4 keV (Sanwal et al., 2002; Mori & Hailey, 2003; Mori et al., 2005). Several possible interpretations of these features include atomic transitions of singly-ionized He in a NS atmosphere with $B \sim 10^{14}$ G (Sanwal et al., 2002),

transitions of mid-Z oxygen or neon in a $B \sim 10^{12}$ G field (Mori & Hailey, 2002), or transitions of high-Z metals at $B \sim 10^{12}$ G.

1.2 This Work

As discussed above, many fundamental questions about isolated NSs remain unanswered: What are the natures of XDINSs and magnetars and are there evolutionary connections between them? Why is the emission from RX J1856.5-3754 featureless and without pulsation? Can a unifying picture be developed to explain the absorption lines from XDINSs? What differentiates magnetars from high-field radio pulsars? Can the strength of magnetar magnetic fields be observed directly? For progress to be made, reliable models of thermal emission from NS surfaces must be developed. The goal of this dissertation is to provide new, more accurate models of NS thermal emission which can be used to better understand the observational data. The dissertation is organized as follows: Chapter 2 discusses thermal emission from the condensed surface of a magnetized NS; Chapter 3 contains a new, quantitative treatment of vacuum polarization effects in NS atmosphere modeling; Chapter 4 uses these models to calculate the observed polarization signal from a rotating NS hotspot, including a new calculation of circular polarization generated in the NS magnetosphere; and Chapter 5 discusses the implications of our calculations to observations of isolated NSs.

Chapter 2

Condensed Surfaces of Strongly Magnetized Neutron Stars

With the exception of 5-6 sources, the thermal spectra of many isolated NSs are featureless and well fit by a blackbody. As discussed above, deep observations with *Chandra* and *XMM-Newton* show that the soft X-ray (0.15-1 keV) spectrum of the XDINS RX J1856.5−3754 (Walter et al., 1996) can be fit with an almost perfect blackbody at $k_B T_{bb}^{\infty} = 64$ eV (e.g., Drake et al., 2002; Burwitz et al., 2003). The optical data of RX J1856.5−3754 is well represented by a Rayleigh-Jeans spectrum, but the observed flux is a factor of 7 higher than the extrapolation from the X-ray blackbody (see Pons et al., 2002). Thus, the spectrum of RX J1856.5−3754 is best fit by a two-temperature blackbody model. Using this model as well as the observational upper limit (1.3% at 2σ) of X-ray pulsation (Burwitz et al., 2003), Braje & Romani (2002) obtained several constraints on the viewing geometry, mass-to-radius ratio, and temperature distribution. Another well-studied, XDINS, RX J0720.4−3125, also shows an X-ray spectrum fit by a blackbody at $T_{bb}^{\infty} \simeq$ 1 MK (Paerels et al. 2001; but see Haberl et al. 2004b for identification of spectral features).

The featureless, and in some cases "perfect" blackbody spectra observed in isolated NSs are puzzling. This is because a NS atmosphere, like any stellar atmosphere, is not a perfect blackbody emitter due to its non-grey photon opacities. On the one hand, a heavy-element (e.g., Fe) atmosphere would produce many spectral lines in the X-ray band (Rajagopal & Romani, 1996; Pons et al., 2002). On the other hand, a light-element (H or He) atmosphere would result in an appreciable

hard tail relative to blackbody (Shibanov et al., 1992).

One physical effect that may help explain the observations is vacuum polarization. The treatment of vacuum polarization in NS atmosphere modeling is discussed in Chapter 3.

Recently, several groups have suggested that the spectrum of RX J1856.5−3754 might be explained if the NS has a condensed surface with no atmosphere above it (Burwitz et al., 2001, 2003; Mori & Ruderman, 2003; Turolla et al., 2004). The notion that an isolated magnetic NS has a condensed surface was first put forward in the 1970s (see Ruderman, 1971; Flowers et al., 1977), although these early studies overestimated the cohesive energy of solid Fe at $B \sim 10^{12}$ G. Revised calculations yield a much smaller cohesive energy (Mueller, 1984; Jones, 1986; Neuhauser et al., 1987; Medin & Lai, 2006) making condensation unlikely for most observed NSs. Lai & Salpeter (1997) studied the phase diagram of a NS H surface layer and showed that for strong magnetic fields, if the surface temperature is below a critical value (which is a function of the magnetic field strength), the atmosphere can undergo a phase transition into a condensed state (see also Lai, 2001). For $B \gtrsim 10^{14}$ G, this may occur for temperatures as high as 10^6 K. This raises the possibility that the thermal radiation is emitted directly from the metal surface of the NS.

The thermal emission from condensed Fe surfaces of magnetic NSs was previously studied by Brinkmann (1980) (see also Itoh, 1975; Lenzen & Truemper, 1978) and shown to produce a rough blackbody with reduced emissivity and a spectral feature at the electron plasma energy. For the temperatures and magnetic fields considered by Brinkmann ($T \gtrsim 10^7$ K and $B = 10^{12-13}$G, appropriate for accreting X-ray pulsars), the Fe surface is not expected to be in the condensed

state. However, at the lower temperatures appropriate for XDINSs, or for the higher magnetic field strengths in magnetars, condensation remains a possibility (see Lai, 2001; Medin & Lai, 2006).

Motivated by recent observations of XDINSs, we calculate the emissivity of condensed Fe or H surfaces of magnetic NSs in the regime where we expect condensation might be possible. Our study goes beyond previous work (Brinkmann, 1980; Turolla et al., 2004) in that we calculate both the spectrum and polarization of the emission, and provide a more accurate treatment of the dissipative effect and transmitted radiation. In previous works, the ions have been treated as fixed; while the exact dielectric tensor of the condensed matter is currently unknown, we also consider the alternate limit of free ions (see §2.1.2).

Regardless of how the effect of ions in the dielectric tensor is treated, we find appreciable difference between our result and that of Turolla et al. (2004). We traced the difference to their neglect of the ion effect, and their "one-mode" treatment of the transmitted radiation in the low-energy regime (see §2.3.1).

2.1 Condensed Surface of Magnetic Neutron Stars

2.1.1 Condition for Condensation

It is well known that strong magnetic fields can qualitatively change the properties of atoms, molecules and condensed matter. For $B \gg B_0 = Z^2 e^3 m_e^2 c/\hbar^3 = 2.35\, Z^2 \times 10^9$ G (where Z is the nuclear charge number), the electrons in an atom are confined to the ground Landau level, and the atom is elongated, with greatly enhanced binding energy. Covalent bonding between atoms leads to linear molecular chains, and interactions between molecular chains can lead to the formation

of three-dimensional condensed matter (for a recent review, see Lai, 2001).

The phase diagram of H has been studied under a variety of conditions. Lai & Salpeter (1997) showed that in strong magnetic fields, there exists a critical temperature $T_{\rm crit}$ below which a phase transition from the gaseous to condensed state occurs, with $kT_{\rm crit}$ about 10% of the cohesive energy of the condensed H. Thus, $T_{\rm crit} \sim 8 \times 10^4$, 5×10^5, 10^6 K for $B = 10^{13}$, 10^{14}, 5×10^{14} G (Lai, 2001; Medin & Lai, 2006). An analogous "plasma phase transition" was also obtained in an alternative thermodynamic model for magnetized H plasma (Potekhin et al., 1999). While this model is more restricted than Lai & Salpeter (1997) in that it does not include long H_n chains, it treats more rigorously atomic motion across the strong B field and Coulomb plasma nonideality. In the Potekhin et al. (1999) model, the density of phase separation is roughly the same as in Lai & Salpeter (1997) (see eq. [2.1] below), but the critical temperature is several times higher. Thus, $T_{\rm crit}$ is probably uncertain by a factor of a few. However, there is no question that for $T \lesssim T_{\rm crit}/2$, the H surface of the NS is in the form of a condensed metallic state with negligible vapor above it.

For heavy elements such as Fe, no such systematic characterization of the phase diagram has been performed. Calculations so far have shown that at $10^{12} - 10^{13}$ G, a linear chain is unbound relative to individual atoms for $Z \gtrsim 6$ (Jones, 1986; Neuhauser et al., 1987; Medin & Lai, 2006) — contrary to earlier expectations (Flowers et al., 1977).[1] Therefore chain-chain interactions play a crucial role in determining whether 3D zero-pressure condensed matter is bound or not. Numerical results of Jones (1986), together with approximate scaling relations suggest an upper limit of the cohesive energy (for $Z \gtrsim 10$) is $Q_s \lesssim Z^{9/5} B_{12}^{2/5}$ eV, where

[1]For sufficiently large B, when $B \gg 10^{14}(Z/26)^3$ G, we expect the linear chain to be bound in a manner similar to the H chain (Lai, 2001).

$B_{12} = B/(10^{12}$ G). Thus for Fe, the critical temperature for phase transition is $T_{\rm crit} \lesssim 0.1 Q_s/k \lesssim 10^{5.5} B_{12}^{2/5}$ K (Lai, 2001).

The zero-pressure density of the condensed matter can be estimated as

$$\rho_s \simeq 560\,\eta\,A\,Z^{-3/5}\,B_{12}^{6/5}\ {\rm g\ cm^{-3}}, \tag{2.1}$$

where A is the mass number of the ion ($A \approx 1.007$ for H, $A \approx 55.9$ for Fe), and $\eta = 1$ corresponds to the uniform electron gas model in the Wigner-Seitz approximation (Kadomtsev, 1970). Other effects (e.g., the Coulomb exchange interaction, or non-uniformity of the electron gas) can reduce the density by up to a factor of ~ 2, and thus η may be as small as 0.5 (Lai, 2001; Potekhin & Chabrier, 2004). In our calculations below, we assume $\eta = 1$. The condensate will be in the liquid state when the Coulomb coupling parameter $\Gamma = (Ze)^2/(a_i kT) = 0.227\,Z^2(\rho_1/A)^{1/3}/T_6 < \Gamma_m$. Here, a_i is the ion sphere radius ($n_i = (4\pi a_i^3/3)^{-1}$, where n_i is the number density of ions), $\rho_1 = \rho_s/(1\ {\rm g\ cm^{-3}})$, $T_6 = T/(10^6$ K), and Γ_m is the characteristic value of Γ at which the Coulomb crystal melts. In the one-component plasma model (i.e., classical ions on the background of the uniform degenerate electron gas), $\Gamma_m = 175$, but electron gas non-uniformity (electron screening) introduces a dependence of Γ_m on ρ and Z; Γ_m is typically within the range $\Gamma_m \sim 160$–190 (Potekhin & Chabrier, 2000). From equation (2.1) we obtain $\Gamma \simeq 1.876\,\eta^{1/3} Z^{9/5} B_{12}^{2/5}/T_6$ at the condensed surface. Therefore, the surface will be solid when $T < 7 \times 10^4 \eta^{1/3}(175/\Gamma_m) B_{14}^{2/5}$ K for H (where $B_{14} = B/10^{14}$ G) and $T < 4 \times 10^6 \eta^{1/3}(175/\Gamma_m) B_{12}^{2/5}$ K for Fe. Therefore, if condensation occurs ($T < T_{\rm crit}$), we expect the Fe condensate to be solid. Note that we use the simple melting criterion above for the condensed phase only. It cannot be used for non-condensed iron at $T \lesssim 10^7$ K (e.g., when T is only slightly above $T_{\rm crit}$) because in this case the state of matter is affected by partial ionization.

2.1.2 Dielectric Tensor of Condensed Matter

The emissivity of the condensed NS surface depends on its dielectric properties. As a first approximation, we use the free electron gas model to determine the (complex) dielectric tensor for condensed matter (Ashcroft & Mermin, 1976). In the coordinate system with magnetic field $\mathbf{B}$ along the z-axis, the dielectric tensor takes the form (cf. Ginzburg 1970)[2]

$$\left[\boldsymbol{\epsilon}\right]_{\hat{\mathbf{z}}=\hat{\mathbf{B}}} = \begin{pmatrix} \epsilon & i\,g & 0 \\ -i\,g & \epsilon & 0 \\ 0 & 0 & \eta \end{pmatrix}, \tag{2.2}$$

where

$$\epsilon \pm g \simeq 1 - \frac{v_e}{(1 \pm u_e^{1/2})(1 \mp u_i^{1/2}) + i\,\gamma_{ei}^{(tr)}}, \tag{2.3a}$$

$$\eta \simeq 1 - \frac{v_e}{1 + i\,\gamma_{ei}^{(l)}}. \tag{2.3b}$$

In eqs. (2.3), the dimensionless quantities $u_e = (E_{Be}/E)^2$, $u_i = (E_{Bi}/E)^2$, $v_e = (E_{pe}/E)^2$ are used, where $E = \hbar\omega$ is the photon energy, E_{Be}, E_{Bi} are the electron and ion cyclotron energies, and E_{pe} is the electron plasma energy. These energies take the values:

$$E_{Be} = \frac{\hbar e B}{m_e c} = 1158\, B_{14}\ \text{keV}, \tag{2.4a}$$

$$E_{Bi} = \frac{\hbar Z e B}{m_i c} = 0.635\, B_{14} \left(\frac{Z}{A}\right)\ \text{keV}, \tag{2.4b}$$

$$\begin{aligned} E_{pe} &= \left(\frac{4\pi\hbar^2 e^2 n_e}{m_e}\right)^{1/2} = 0.0288 \left(\frac{Z}{A}\right)^{1/2} \rho_1^{1/2}\ \text{keV} \\ &= 10.8\, \eta^{1/2} Z^{1/5} B_{14}^{3/5}\ \text{keV}, \end{aligned} \tag{2.4c}$$

[2]See also Lai & Ho 2003a. Note that eq. (13) of Lai & Ho 2003a is incorrect: $\gamma_{ei}^{\pm}$ should simply be $\gamma_{ei}(1 + Zm_e/Am_p)$. We neglect the factor $1 + Zm_e/Am_p$ in eq. (2.3a) since it provides a negligible correction relative to the uncertainty in the collisional damping (see §2.3).

where n_e is the electron number density, m_i is the ion mass, and we have substituted eq. (2.1) for ρ. The collisional damping is calculated for transverse and longitudinal motions with respect to the magnetic field. The dimensionless damping rates $\gamma_{ei}^{(tr)}$ and $\gamma_{ei}^{(l)}$ are obtained from the collisional damping rates $\nu_{ei}^{(tr)}$ and $\nu_{ei}^{(l)}$ (see §2.1.3) through $\gamma_{ei}^{(tr)} = \hbar\nu_{ei}^{(tr)}/E$ and $\gamma_{ei}^{(l)} = \hbar\nu_{ei}^{(l)}/E$.

Equations (2.3) give the elements of the dielectric tensor for a cold, magnetized plasma. While the expressions were derived classically, the quantum calculation, incorporating the quantized nature of electron motion transverse to the magnetic field, yields identical results (Canuto & Ventura, 1972; Pavlov et al., 1980). More significantly, the expressions (2.3) assume that the electrons and ions are subject to the pairwise Coulomb attraction, the interaction with the stationary magnetic field, and the periodic force from the propagating electromagnetic wave. At high densities, however, other interactions can also be important. For instance, the ions are strongly coupled to each other when the Coulomb parameter Γ is large. It is this coupling that leads to the liquid-solid phase transition mentioned in §2.1.1. It has been suggested by Turolla et al. (2004) that in the solid phase the ion motion should be frozen (by setting the ion mass $m_i = \infty$), however, this treatment is not exactly correct. It is known that optical modes of a crystal lattice (at $B = 0$) can be derived from a polarizability of the form given by equation (2.3) with an additional term in the denominator which specifies the binding of the ions (see, e.g., Ziman, 1979). According to the harmonic model of the Coulomb crystal (Chabrier, 1993), the characteristic ion oscillation frequency (the Debye frequency of acoustic phonons) is $\omega_D \approx 0.4E_{pi}/\hbar$, where $E_{pi} = 6.75 \times 10^{-4}\,(Z/A)\,\rho_1^{1/2}$ keV is the ion plasma energy. The magnetic field appreciably affects the motion of the ions in the Coulomb crystal if $\hbar\omega_D/E_{Bi} \lesssim 1$ (or $E_{pi} \lesssim E_{Bi}$, see Usov et al. 1980).

From eqs. (2.4) we find $\hbar\omega_D/E_{Bi} \approx 1.6\eta^{1/2}A^{1/2}Z^{-0.3}B_{14}^{-0.4}$, which shows that the magnetic forces on the ions are not completely negligible compared to the Coulomb lattice forces.

Needless to say, our current understanding of condensed matter in strong magnetic fields is crude, and equations (2.3) are only a first approximation to the true dielectric tensor of the magnetized medium. In our calculations below, in addition to the case of of quasi-free ions described by eqs. (2.3), we will also consider the case where the motion of the ions is neglected (formally obtained by setting $m_i = \infty$). It is reasonable to expect that, in reality, the surface radiation spectra lie between the results obtained for these two limiting cases. Nevertheless, future work is needed to evaluate the reliability of our results at low frequencies.

2.1.3 Collisional Damping Rate in Condensed Matter

For the collisional damping rates $\gamma_{ei}^{(l,tr)}$, different approximations can be used in different ranges of frequency ω and density ρ. For $E \gg E_{pe}$, the electron-ion collisions are considered to be independent, and $\gamma_{ei}^{(l,tr)}$ are determined by the effective rates of free-free transitions of a single electron-ion pair. However, this approximation fails for $E \lesssim E_{pe}$, where collective effects become important and electron degeneracy in the condensed surface should be taken into account. In general, the complex dielectric tensor $\boldsymbol{\epsilon}$ for arbitrary ω can be obtained from kinetic theory, at least in principle (see, e.g., Ginzburg, 1970). Since such an expression for $\boldsymbol{\epsilon}$ is presently unknown, we shall approximate $\gamma_{ei}^{(l,tr)}$ in the $E \lesssim E_{pe}$ regime using the result of Potekhin (1999), who obtained the zero-frequency conductivity tensor for degenerate Coulomb plasmas (liquid and solid) in arbitrary magnetic fields. Specifically, we set $\nu_{ei}^{(l)} = 1/\tau_{\parallel}$, $\nu_{ei}^{(tr)} = 1/\tau_{\perp}$, where $\tau_{\parallel}$ and $\tau_{\perp}$ are the effective

collision times given by eqs. (28) and (39) of Potekhin (1999), respectively. Figure 2.1 shows $\hbar\nu_{ei}^{(tr)}$ and $\hbar\nu_{ei}^{(l)}$ as a function of magnetic field strength for a condensed Fe surface at $T = 10^6$ K, over the range $B = 10^{12} - 10^{14}$ G.

The calculations of $\nu_{ei}^{(l)}$ and $\nu_{ei}^{(tr)}$ adopted in our paper neglect the influence of the magnetic field on the motion of the ions. Therefore, these calculations apply only in the $u_i \to 0$ limit (this corresponds to the "fixed" ion limit of §2.1.2), or to the regime $E \gg E_{Bi}$. We note, however, that the emissivity at $E \lesssim E_{Bi}$ does not depend sensitively on the damping rates (see §2.3; in particular, Fig. 2.2 shows that the emissivity at such low energies is almost the same with or without damping). Thus, unless the true values of $\nu_{ei}^{(l)}$, $\nu_{ei}^{(tr)}$ at such low energies are many orders of magnitude larger than our adopted values, our emissivity results will not be affected by this uncertainty (indeed, as discussed in §2.1.2, the main uncertainty at such low energies lies in whether to treat the ions as "free" or "fixed").

2.2 Emission From Condensed Matter: Method

We consider the regime where a clear phase separation occurs at the NS surface (i.e., for T at least a few times lower than $T_{\rm crit}$), so that the vapor (gas) above the condensed surface has negligible density and optical depth to photons. In this case the radiation emerges directly from the condensed matter.

2.2.1 Kirchhoff's Law for a Macroscopic Object

A macroscopic body at temperature T produces an intrinsic thermal emission, with specific intensity $I_\nu^{(e)}$. To calculate this intensity, consider the body placed inside a blackbody cavity also at temperature T. The body is in thermodynamic equilibrium with the surrounding radiation field, which has an intensity given by

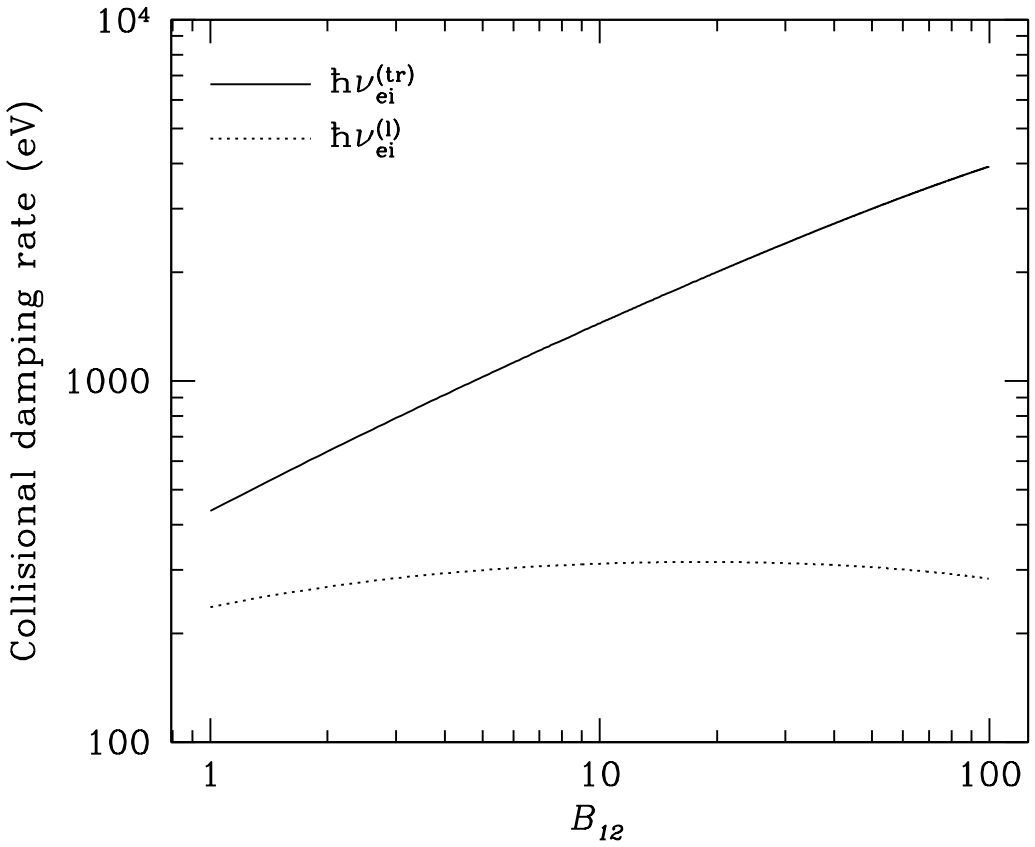

Figure 2.1: Transverse and longitudinal damping rates $\hbar\nu_{ei}^{(tr)}$ and $\hbar\nu_{ei}^{(l)}$ as a function of magnetic field strength $B = 10^{12}B_{12}G$ for a condensed Fe surface at $T = 10^6$ K. The density is calculated using eq. (2.1), with $\eta = 1$.

the Planck function $B_\nu(T)$. Imagine a ray of the cavity radiation impinging on a surface element dA of the body. The radiation field is unpolarized, and the electric field of the incoming ray can be written in terms of two independent polarization states: $\mathbf{E}_1^{(\mathrm{i})} = \mathcal{A}\mathbf{e}_1^{(\mathrm{i})}$ and $\mathbf{E}_2^{(\mathrm{i})} = \mathcal{A}\mathbf{e}_2^{(\mathrm{i})}$, where $\mathcal{A} = \sqrt{B_\nu/2}$, and $\mathbf{e}_1^{(i)}$ and $\mathbf{e}_2^{(i)}$ are the polarization eigenvectors of the incident wave. The ray is, in general, partially reflected, with each incoming polarization giving rise to a reflected field:

$$\mathbf{E}_1^{(r)} = \mathcal{A}\left(r_{11}\mathbf{e}_1^{(r)} + r_{12}\mathbf{e}_2^{(r)}\right), \tag{2.5a}$$

$$\mathbf{E}_2^{(r)} = \mathcal{A}\left(r_{21}\mathbf{e}_1^{(r)} + r_{22}\mathbf{e}_2^{(r)}\right), \tag{2.5b}$$

where $\mathbf{E}_1^{(\mathrm{r})}$ and $\mathbf{E}_2^{(\mathrm{r})}$ are the reflected electric fields due to incoming fields $\mathbf{E}_1^{(\mathrm{i})}$ and $\mathbf{E}_2^{(\mathrm{i})}$, respectively. Thus, the intensity of radiation in the reflected field with polarizations $\mathbf{e}_1^{(\mathrm{r})}$ and $\mathbf{e}_2^{(\mathrm{r})}$ is:

$$I_{\nu 1}^{(r)} = \frac{1}{2}\left(|r_{11}|^2 + |r_{21}|^2\right)B_\nu \equiv \frac{1}{2}R_1 B_\nu, \tag{2.6a}$$

$$I_{\nu 2}^{(r)} = \frac{1}{2}\left(|r_{12}|^2 + |r_{22}|^2\right)B_\nu \equiv \frac{1}{2}R_2 B_\nu. \tag{2.6b}$$

The energy in the incoming wave for a frequency band $\nu \to \nu + d\nu$ during time dt is $B_\nu\, dA\, d\Omega^{(i)}\, d\nu\, dt$, where $d\Omega^{(i)}$ is the solid angle element around the direction of the incoming ray. Similarly, the energy contained in the reflected wave (for each polarization) is $(1/2)R_{1,2}\, B_\nu\, dA\, d\Omega^{(r)}\, d\nu\, dt$, with $d\Omega^{(r)} = d\Omega^{(i)}$. To insure that the cavity radiation field remains an unpolarized blackbody, the intensities of the radiation emitted by the body (in the same direction as the reflected wave) with polarizations $\mathbf{e}_1^{(\mathrm{r})}$ and $\mathbf{e}_2^{(\mathrm{r})}$ must be:

$$I_{\nu 1}^{(e)} = \frac{1}{2}B_\nu - I_{\nu 1}^{(r)} = \frac{1}{2}(1 - R_1)B_\nu, \tag{2.7a}$$

$$I_{\nu 2}^{(e)} = \frac{1}{2}B_\nu - I_{\nu 2}^{(r)} = \frac{1}{2}(1 - R_2)B_\nu. \tag{2.7b}$$

Since $I_{\nu 1}^{(e)}$ and $I_{\nu 2}^{(e)}$ are intrinsic properties of the body, these equations should also apply even when the body is not in thermodynamic equilibrium with a blackbody

radiation field. Thus, a body at temperature T has emission intensity

$$I_\nu^{(e)} = (1-R)B_\nu(T) \equiv JB_\nu(T) \tag{2.8}$$

where $R \equiv (1/2)(R_1 + R_2)$ is the reflectivity, and $J = 1 - R$ is the dimensionless emissivity. The degree of linear polarization of the emitted radiation is

$$P \equiv \frac{I_{\nu 1}^{(e)} - I_{\nu 2}^{(e)}}{I_{\nu 1}^{(e)} + I_{\nu 2}^{(e)}} = \frac{1}{2}\frac{R_2 - R_1}{1-R}. \tag{2.9}$$

2.2.2 Calculation of Reflectivity

To calculate the reflectivity R, we set up a coordinate system as follows: the surface lies in the xy plane with the z-axis along the surface normal. The external magnetic field $\mathbf{B}$ lies in the xz plane, with $\hat{\mathbf{B}} \times \hat{\mathbf{z}} = \sin\theta_B \hat{\mathbf{y}}$, where θ_B is the angle between $\hat{\mathbf{B}}$ and $\hat{\mathbf{z}}$. Consider a ray (of given polarization, $\mathbf{e}_1^{(i)}$ or $\mathbf{e}_2^{(i)}$) impinging on the surface, with incident angle $\theta^{(i)}$ and azimuthal angle φ, such that the unit wave vector $\hat{\mathbf{k}}^{(i)} = (-\sin\theta^{(i)}\cos\varphi, -\sin\theta^{(i)}\sin\varphi, -\cos\theta^{(i)})$. The transmitted (refracted) and reflected rays lie in the same plane as the incident ray. Our goal is to calculate the field associated with the reflected ray.

Outside the condensed medium ($z > 0$), the dielectric and permeability tensors are determined by the vacuum polarization effect with $\boldsymbol{\epsilon} = a\boldsymbol{I} + q\hat{\mathbf{B}}\hat{\mathbf{B}}$ and $\boldsymbol{\mu}^{-1} = a\boldsymbol{I} + m\hat{\mathbf{B}}\hat{\mathbf{B}}$, where a, q, m are dimensionless functions of B (see Ho & Lai, 2003, and the references therein). Since $a \sim 1$ and $|q|,\ |m| \ll 1$ for $B \ll 5 \times 10^{16}$ G, the vacuum polarization effect is negligible. In our calculation (Appendix A), we choose $\mathbf{e}_1^{(i)}$ $\left(\text{and } \mathbf{e}_1^{(r)}\right)$ to be along the incident plane and $\mathbf{e}_2^{(i)}$ $\left(\text{and } \mathbf{e}_2^{(r)}\right)$ perpendicular to it.

Consider an incident ray with $\mathbf{E}^{(i)} = \mathbf{E}_1^{(i)} = \mathcal{A}\mathbf{e}_1^{(i)}$. The $\mathbf{E}$-field of the reflected

ray takes the form given by eq. (2.5a), while the transmitted wave has the form:

$$\mathbf{E}^{(t)} = \mathbf{E}_1^{(t)} = \mathcal{A}\left(t_{11}\mathbf{e}_1^{(t)} + t_{12}\mathbf{e}_2^{(t)}\right). \tag{2.10}$$

The eigenvectors of the transmitted wave, $\mathbf{e}_1^{(t)}$ and $\mathbf{e}_2^{(t)}$, depend on the refraction angles, $\theta_1^{(t)}$ and $\theta_2^{(t)}$, respectively; note that in general, these angles are complex and distinct from each other. The refraction angle $\theta_j^{(t)}$, the mode eigenvector $\mathbf{e}_j^{(t)}$ and the corresponding index of refraction $n_j^{(t)}$ $(j = 1, 2)$ satisfy Snell's law

$$\sin\theta^{(i)} = n_j^{(t)} \sin\theta_j^{(t)}, \tag{2.11}$$

and the mode equation[3]

$$\left[\boldsymbol{\epsilon} + (n_j^{(t)})^2\left(\hat{\mathbf{k}}_j^{(t)}\hat{\mathbf{k}}_j^{(t)} - \mathbf{I}\right)\right]\cdot\mathbf{E}_j^{(t)} = 0, \tag{2.12}$$

where $\mathbf{I}$ is the unit tensor, and $\hat{\mathbf{k}}_j^{(t)} = (-\sin\theta_j^{(t)}\cos\varphi, -\sin\theta_j^{(t)}\sin\varphi, -\cos\theta_j^{(t)})$ is the unit wavevector of the transmitted waves.

In the xyz coordinate system, the rotated dielectric tensor takes the form:

$$\left[\boldsymbol{\epsilon}\right] = \begin{pmatrix} \epsilon\cos^2\theta_B + \eta\sin^2\theta_B & ig\cos\theta_B & (\epsilon-\eta)\sin\theta_B\cos\theta_B \\ -ig\cos\theta_B & \epsilon & -ig\sin\theta_B \\ (\epsilon-\eta)\sin\theta_B\cos\theta_B & ig\sin\theta_B & \epsilon\sin^2\theta_B + \eta\cos^2\theta_B \end{pmatrix} \tag{2.13}$$

For eq. (2.12) to have a non-trivial solution, the determinant of the matrix $\boldsymbol{\epsilon} + \left(n_j^{(t)}\right)^2\left(\hat{\mathbf{k}}_j^{(t)}\hat{\mathbf{k}}_j^{(t)} - \mathbf{I}\right)$ must be equal to zero. This gives an equation involving powers of $n_j^{(t)}$, $\sin\theta_j^{(t)}$, and $\cos\theta_j^{(t)}$. Substituting eq. (2.11) into this equation, and squaring both sides yields a fourth-order polynomial in $\left(n_j^{(t)}\right)^2$, which allows for the determination of the indices of refraction (see Appendix A.1 for more details).

[3]The vacuum polarization effect is neglected in eq. (2.12), which is justified because the density of the condensed medium is much larger than the vacuum resonance density, $\rho_V \simeq 0.96(A/Z)B_{14}^2(E/\mathrm{keV})^2$ g cm^{-3} (see Lai & Ho, 2002).

Having determined $n_j^{(t)}$, eq. (2.12) can be used to calculate $\mathbf{e}_j^{(t)}$, while eq. (2.11) gives $\theta_j^{(t)}$. Once $\theta_j^{(t)}$, $\mathbf{e}_j^{(t)}$ and $n_j^{(t)}$ are known, r_{11}, r_{12}, t_{11} and t_{12} can be obtained using the standard electromagnetic boundary conditions:

$$\Delta\mathbf{D}\cdot\hat{\mathbf{z}}=0,\quad \Delta\mathbf{B}\cdot\hat{\mathbf{z}}=0,\quad \Delta\mathbf{E}\times\hat{\mathbf{z}}=0,\quad \Delta\mathbf{H}\times\hat{\mathbf{z}}=0, \tag{2.14}$$

where, e.g., $\Delta\mathbf{E}\equiv\mathbf{E}^{(i)}+\mathbf{E}^{(r)}-\mathbf{E}^{(t)}$, $\mathbf{D}^{(t)}=\boldsymbol{\epsilon}\cdot\mathbf{E}^{(t)}$, and

$$\mathbf{H}^{(t)}=\mathbf{B}^{(t)}=\mathcal{A}\left(n_1^{(t)}t_{11}\,\hat{\mathbf{k}}_1^{(t)}\times\mathbf{e}_1^{(t)}+n_2^{(t)}t_{12}\,\hat{\mathbf{k}}_2^{(t)}\times\mathbf{e}_2^{(t)}\right), \tag{2.15}$$

neglecting the vacuum polarization effect ($\boldsymbol{\mu}\simeq\mathbf{I}$). Note that eqs. (2.14) are not all independent, and only $\Delta\mathbf{E}\times\hat{\mathbf{z}}=0$ and $\Delta\mathbf{B}\times\hat{\mathbf{z}}=0$ are used in our calculation.

A similar procedure applies in the case when the incident wave is $\mathbf{E}^{(i)}=\mathbf{E}_2^{(i)}=\mathcal{A}\mathbf{e}_2^{(i)}$, yielding the reflection coefficients r_{21} and r_{22} (together with t_{21}, and t_{22}).

2.3 Emission from Condensed Surface: Results

In this section, we present the results of our surface emission calculations for three illustrative cases: Fe surfaces at $B=10^{12}$ G and 10^{13} G, and a H surface at 10^{14} G. As discussed in §2.1.1, the condensation temperature for these cases is around 10^6 K. Note that the dimensionless emissivity $J=1-R$ [see eq. (2.8)] depends weakly on T through the collisional damping rate (§2.1.3). For concreteness, we set $T=10^6$ K in all our calculations. Figures 2.2–2.4 show the emissivity J as a function of photon energy E for the three cases; in each, the B field is assumed to be normal to the surface ($\theta_B=0$). In all three cases, the emissivity is reduced (compared to blackbody) at low energies, and approaches unity for $E>$ a few$\times E_{pe}$. For the case of Fe, there are features associated with the ion cyclotron energy E_{Bi} and the electron plasma energy E_{pe}. For H, the electron plasma energy is too high

to be of interest for observation, but the feature around the ion cyclotron energy is evident.

The spectral feature in the emissivity J near E_{Bi} can be understood by considering the special case of normal incidence ($\theta^{(i)} = 0$). In this case the reflectivity takes the analytic form:

$$R = \frac{1}{2}\left|\frac{n_1 - 1}{n_1 + 1}\right|^2 + \frac{1}{2}\left|\frac{n_2 - 1}{n_2 + 1}\right|^2, \tag{2.16}$$

where n_1 and n_2 are the indices of refraction of the two modes in the medium, and are given by $n_1^2 = \epsilon + g$, $n_2^2 = \epsilon - g$. Consider energies around E_{Bi}, such that $v_e, u_e \gg 1$. We find

$$\begin{aligned} n_{1,2}^2 \;\approx\; & 1 \mp \frac{v_e(1 \mp u_i^{1/2})}{u_e^{1/2}(1 \mp u_i^{1/2})^2 + (\gamma_{ei}^{(tr)})^2} \\ & + i\frac{v_e \gamma_{ei}^{(tr)}}{u_e(1 \mp u_i^{1/2})^2 + (\gamma_{ei}^{(tr)})^2}. \end{aligned} \tag{2.17}$$

Although $\gamma_{ei}^{(tr)}$ can be greater than unity (see Fig. 2.1), a qualitative understanding of the spectral features can be achieved by neglecting the imaginary part of $n_{1,2}^2$, since $v_e/u_e \ll 1$ [see eq. (2.4)]. Then eq. (2.17) becomes

$$n_{1,2}^2 \approx 1 \mp \frac{v_e}{u_e^{1/2}(1 \mp u_i^{1/2})} \tag{2.18}$$

For $E < E_{Bi}$ ($u_i > 1$), both n_1 and n_2 are real and differ from unity, leading to $J < 1$. For $E > E_{Bi}$, n_1 is imaginary until $(v_e/u_e^{1/2})(1 - u_i^{1/2})^{-1} < 1$, which occurs at

$$E_C \approx E_{Bi} + E_{pe}^2/E_{Be}. \tag{2.19}$$

Thus, for $E_{Bi} < E < E_C$, n_1^2 increases from $-\infty$ to 0 (implying no mode propagation in the medium), giving rise to the broad depression in J (with $J \to 0.5$ as the energy nears E_C).

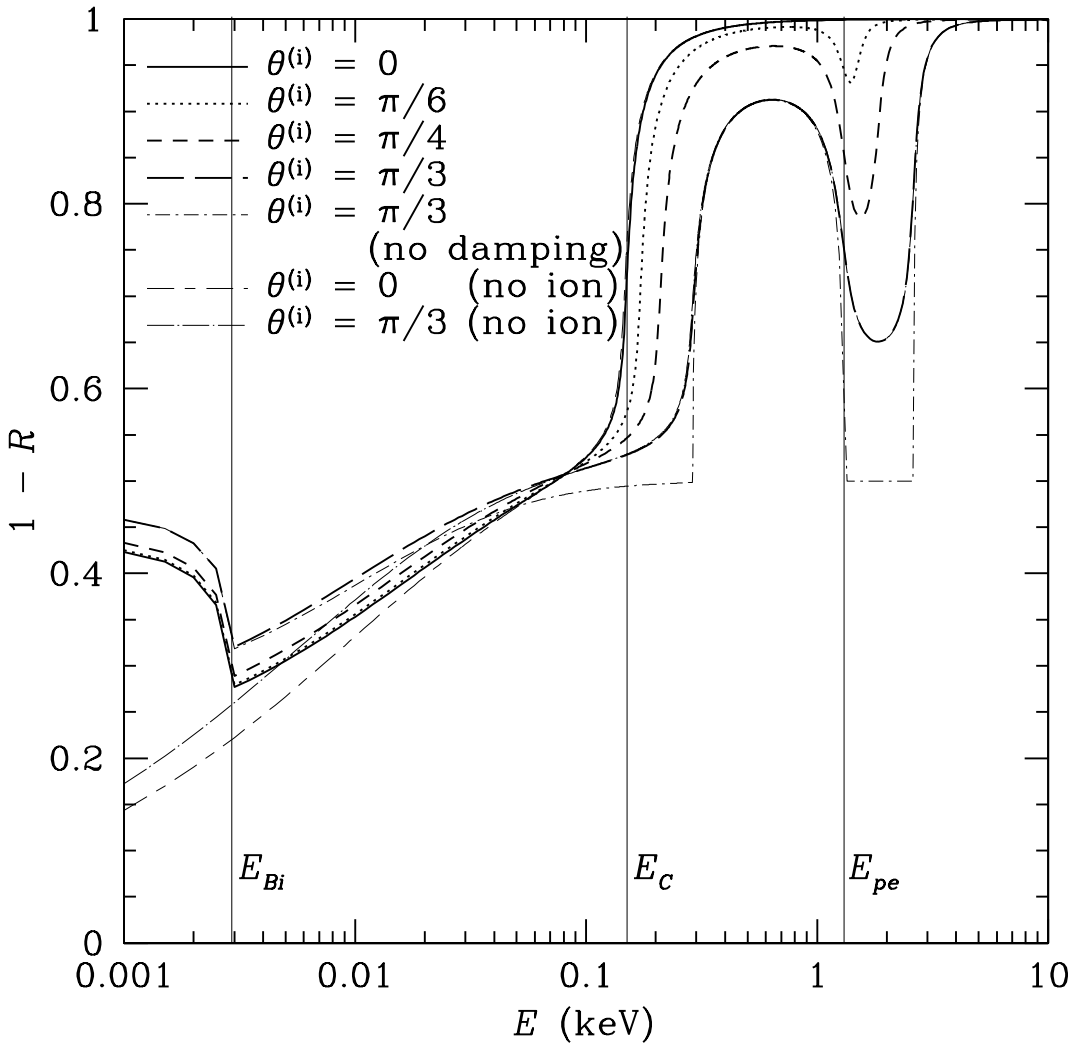

Figure 2.2: Dimensionless emissivity as a function of photon energy for a condensed Fe surface, at $B = 10^{12}$ G. The B field is normal to the surface. The different curves correspond to different angles $\theta^{(i)}$ between the incident photon direction and surface normal. The short-dashed-dotted line shows the result when the collisional damping is set to zero in the plasma dielectric tensor. The other light lines show the results when ion motion is neglected for two values of $\theta^{(i)}$ (by setting the ion mass to ∞; see §2.1.2). The three vertical lines denote the ion cyclotron energy E_{Bi}, the electron plasma energy E_{pe} [see eq. (2.4)] and E_c [eq. (2.19)].

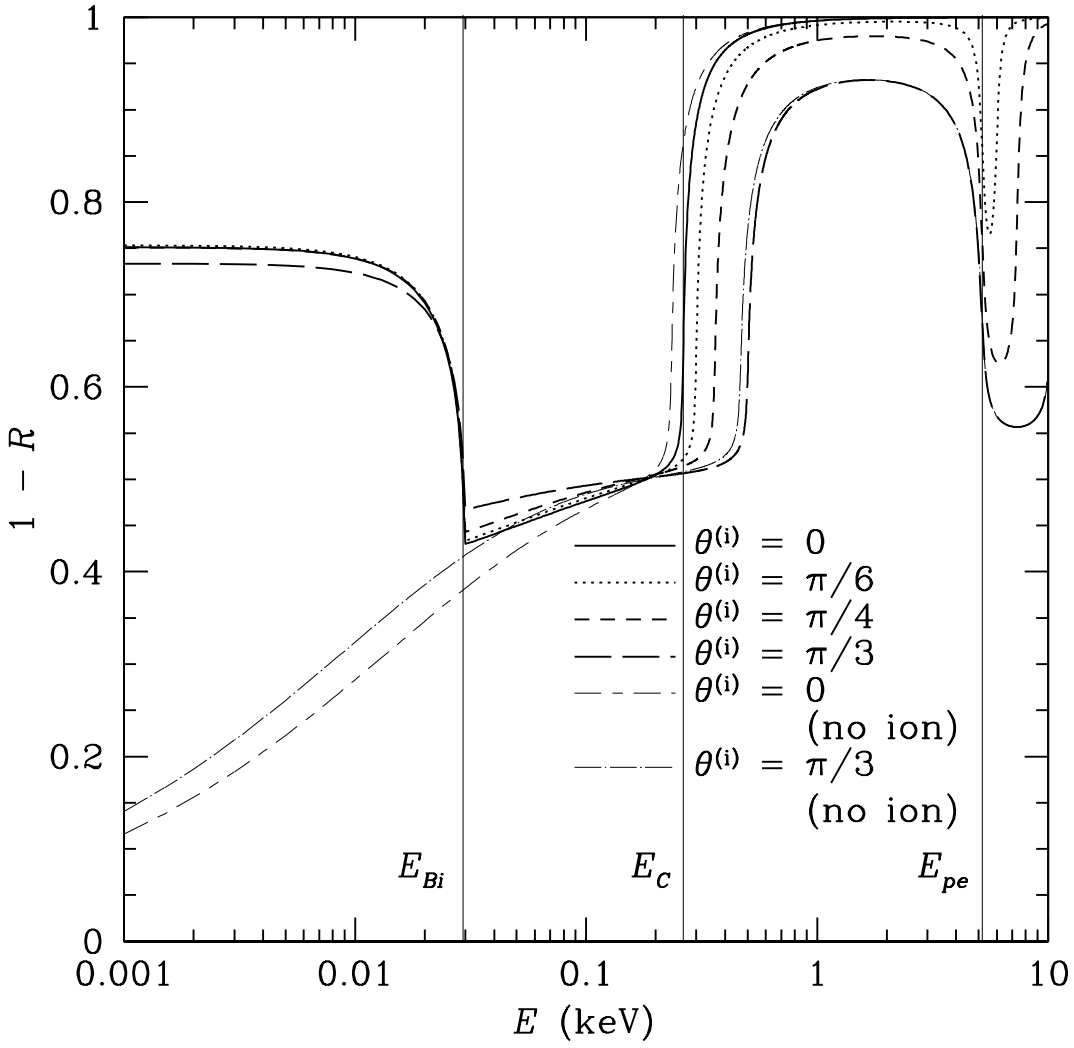

Figure 2.3: Same as Fig. 2.2, except for $B = 10^{13}$ G.

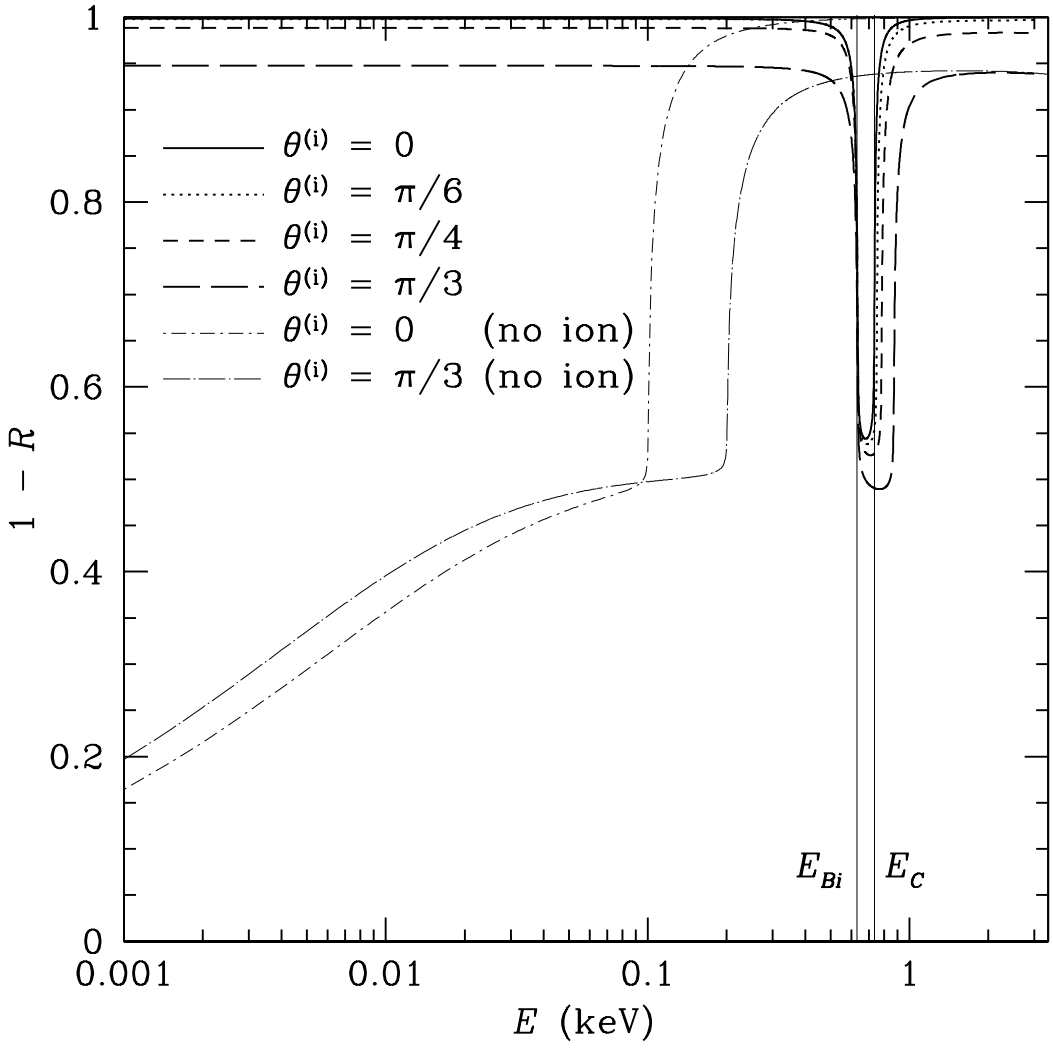

Figure 2.4: Same as Fig. 2.2, except for a H surface at 10^{14} G.

We can similarly understand the feature near the electron plasma energy. This feature appears only for $\theta^{(i)} \neq 0$. For energies around E_{pe}, $u_e \gg 1$, $u_i \ll 1$, and we have $\epsilon \approx 1 + v_e/u_e$ and $g \approx -v_e/u_e^{1/2}$. Substituting these values into (2.12) and neglecting terms to order v_e/u_e and higher, we find

$$n_1^2 \approx 1 + \frac{v_e}{(1 - v_e)} \sin^2 \theta^{(i)}, \quad n_2^2 \approx 1. \tag{2.20}$$

For $E > E_{pe}$, both n_1 and n_2 are real, while for $E < E_{pe}$, $n_1^2 < 0$. The reflectivity no longer takes the simple analytic form of (2.16). However, the basic behavior of the reflectivity is similar to the case of normal incidence: for one mode with imaginary n and the other with $n \approx 1$, the emissivity J attains a local minimum ($\simeq 0.5$ in the absence of collisional damping; see Fig. 2.2).

When calculating the emissivity, it is clear that the inclusion of the ion terms in eqs. (2.3) for the elements of the dielectric tensor can qualitiatively change the emission spectrum at low energies (see Figs. 2.2–2.7). As discussed in §2.1.2, complete neglect of ion effects is not justified; while the exact dielectric tensor is currently unknown, the true spectra should lie between the two limiting cases we present here. Without the ion terms, the broad feature around E_{Bi} is replaced by a stronger depression of J at low energies, up to $E \sim E_C$. At high energies, the ion effect is unimportant.

Figures 2.5 and 2.6 give some examples of our numerical results for the cases when the magnetic field is not perpendicular to the surface (i.e., $\theta_B \neq 0$). In these cases the emissivity J is no longer symmetric with respect to the surface normal, but depends on both $\theta^{(i)}$ and the azimuthal angle φ. Although the geometry is more complicated, the basic features of the emissivity are similar to those depicted in Figs. 2.2–2.4.

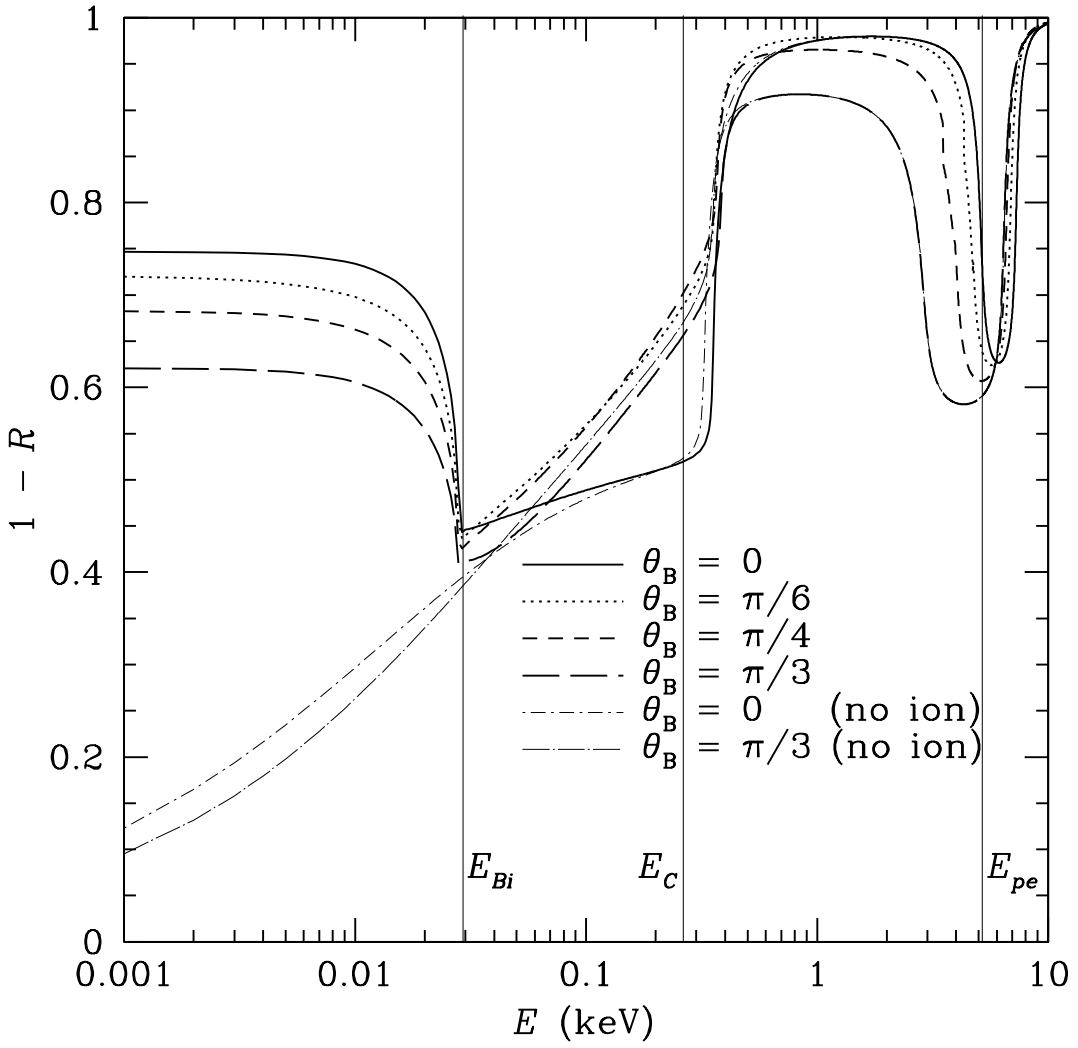

Figure 2.5: Dimensionless emissivity $J = 1 - R$ as a function of photon energy E for the case of a condensed Fe surface at $B = 10^{13}$ G. The incident angles are fixed at $\theta^{(i)} = \pi/4$ and $\varphi = \pi/4$. The different curves correspond to different magnetic field inclination angles (θ_B is the angle between $\mathbf{B}$ and the surface normal). As in Fig. 2.2, the light lines (labeled "no ion") show the results when ion motion is neglected in the plasma dielectric tensor.

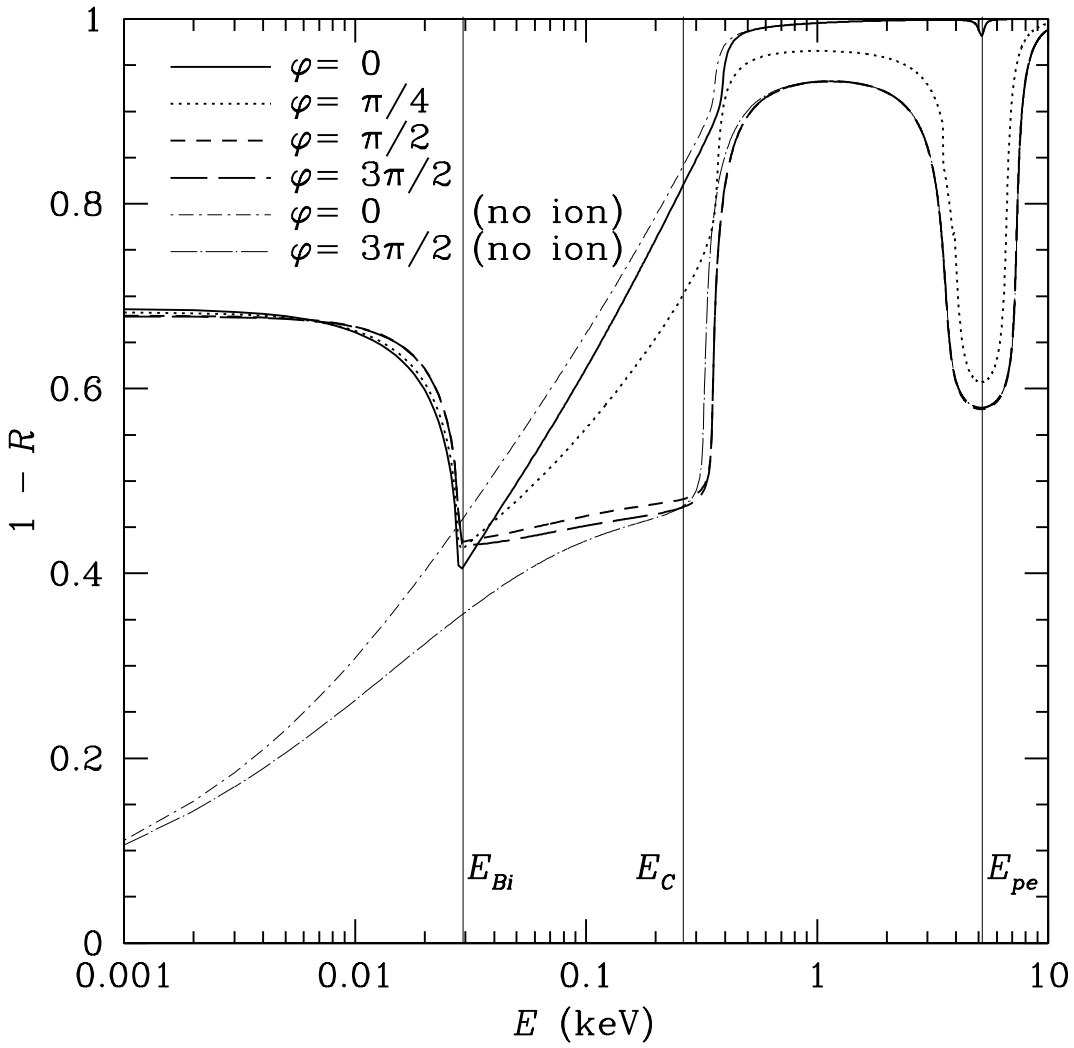

Figure 2.6: Same as Fig. 2.5, except that the geometry is fixed at $\theta^{(i)} = \pi/4$ and $\theta_B = \pi/4$, and the different curves correspond to different values of φ (the angle of the plane of incidence with respect to the xz plane; see §2.2.2).

The specific flux at the NS surface is:

$$F_\nu = \int_0^{2\pi} d\varphi \int_0^{\pi/2} d\theta^{(i)} \cos\theta^{(i)} \sin\theta^{(i)} J(\theta^{(i)}, \varphi)\, B_\nu(T). \tag{2.21}$$

F_ν is shown in Figure 2.7 as a function of photon energy for the three cases illustrated in Figs. 2.2–2.4. For the Fe surface, there is reduced emission (by a factor of 2 or so) around $E_{Bi} \lesssim E \lesssim E_c$ compared to blackbody at the same temperature. For the H surface at $B = 10^{14}$ G, the flux is close to blackbody at all energies except for a broad feature around E_{Bi}.

Radiation from a condensed surface is polarized. Figures 2.8 and 2.9 show the degree of linear polarization as a function of energy for the cases illustrated in Figures 2.3 and 2.4 (i.e., Fe at 10^{13} G and H at 10^{14} G). The degree of linear polarization P increases with angle of incidence, and is clearly peaked around E_{Bi} and E_{pe}. For the Fe surface, at energies below E_C, the polarization vector is parallel to the **k**-**B** plane. Above E_C, the sign of P changes, and the radiation is polarized perpendicular to the **k**-**B** plane. For H, there is a slight net linear polarization perpendicular to the **k**-**B** plane, except near E_{Bi}, where the polarization peaks with $P > 0$. These polarization properties of condensed surface emission are qualitatively different from those of atmosphere emission (see Chapter 4).

2.3.1 Comparison with Previous Work

Recently, Turolla et al. (2004) performed a detailed calculation of the emissivity of a solid Fe surface. Our results differ significantly from theirs in several respects. In particular, Turolla et al. found that collisional damping in the condensed matter leads to a sharp cut-off in the emission at low photon energies, especially when the magnetic field is inclined with respect to the surface normal. For comparison,

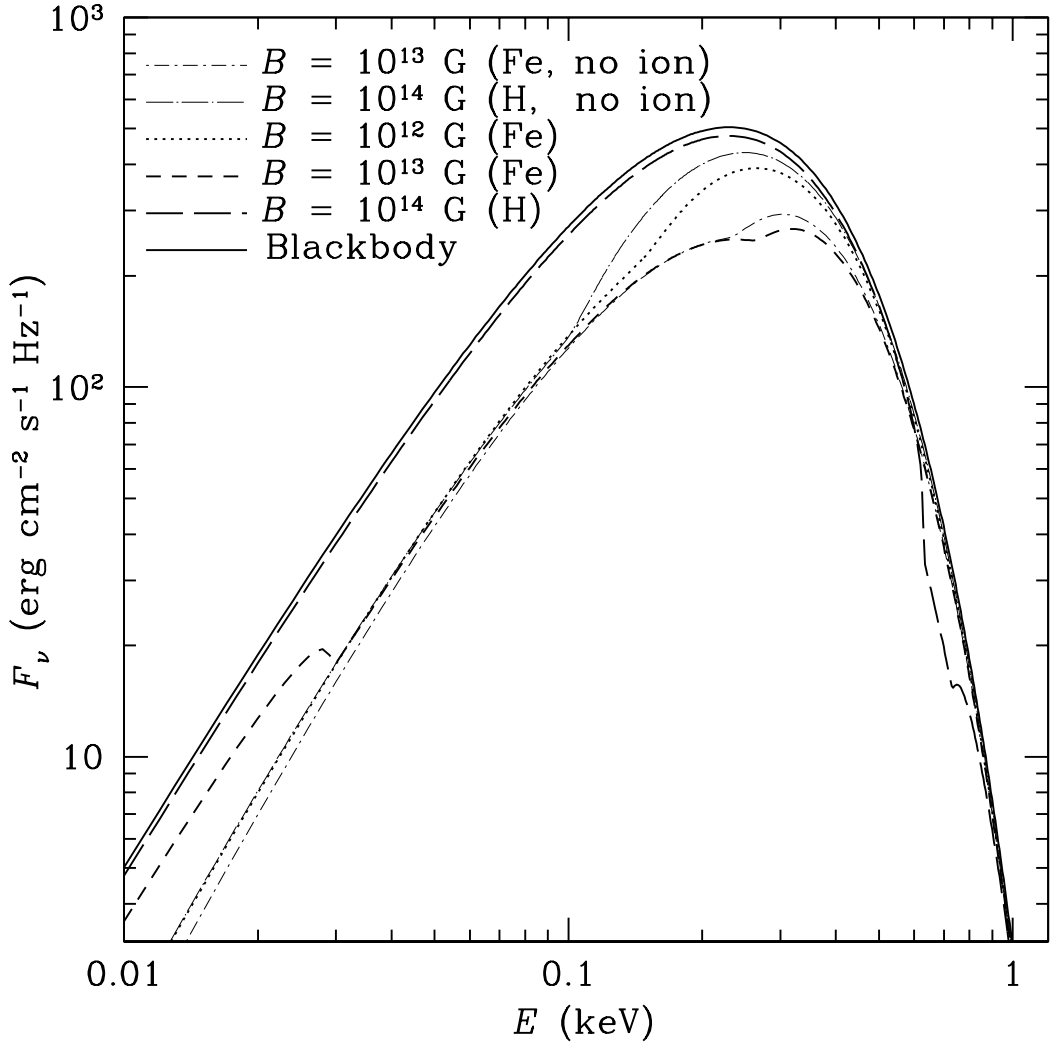

Figure 2.7: Spectral flux as a function of photon energy E for the cases of condensed Fe ($B = 10^{12}, 10^{13}$ G) and H ($B = 10^{14}$ G) surfaces, all at temperature $T = 10^6$ K. The light lines (labeled "no ion") show the flux for Fe and H surfaces when ion motion is neglected. The solid line shows the blackbody spectrum at 10^6 K. For all of the curves, the magnetic inclination angle $\theta_B = 0$.

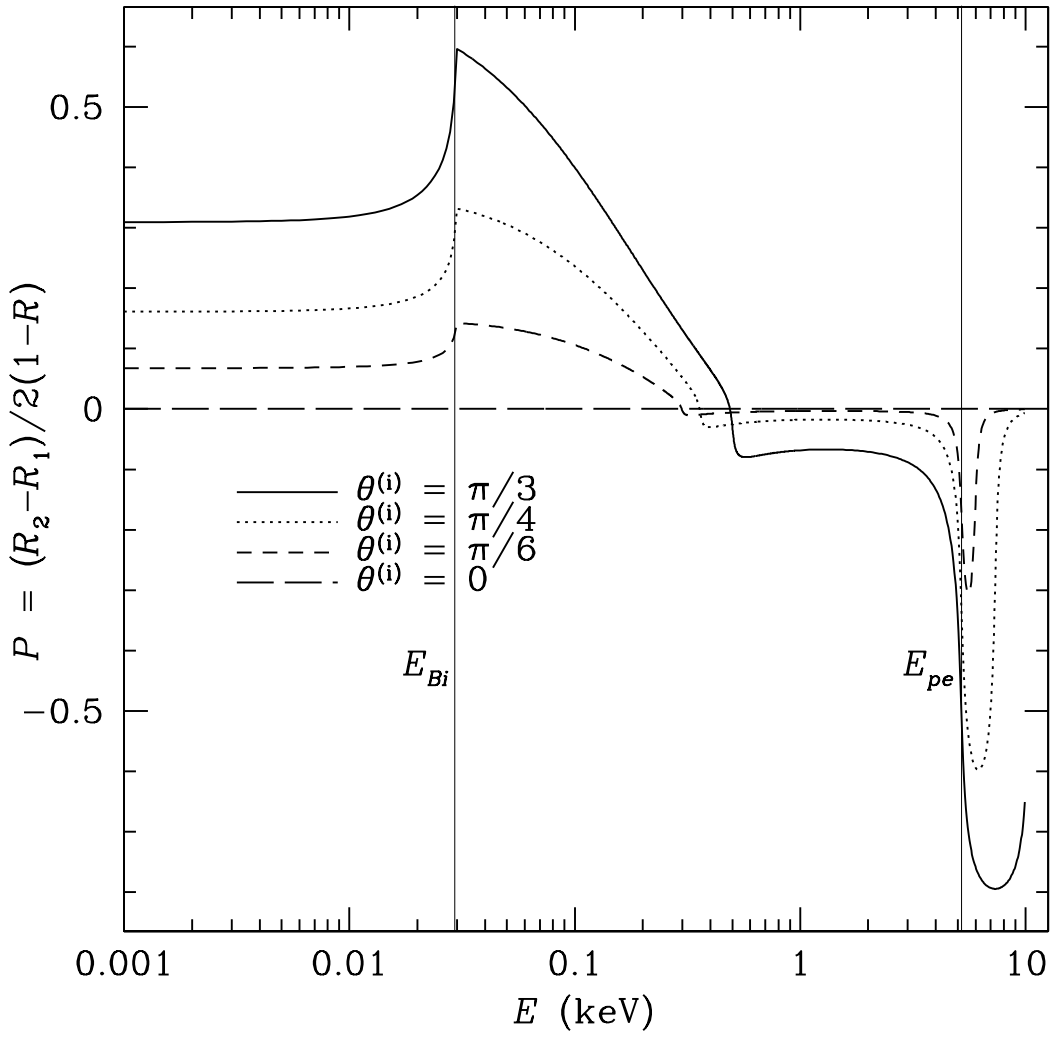

Figure 2.8: Degree of linear polarization P [see eq. (2.9)] as a function of photon energy E for the case of a condensed Fe surface with $B = 10^{13}$ G. The B field is normal to the surface, and the different curves correspond to different angles $\theta^{(i)}$ between the incident photon direction and surface normal. The net linear polarization is peaked around E_{Bi} and E_{pe}. Positive P corresponds to polarization parallel to the **k**-**B** plane, while negative P corresponds to polarization perpendicular the **k**-**B** plane. Note that P changes sign around E_C.

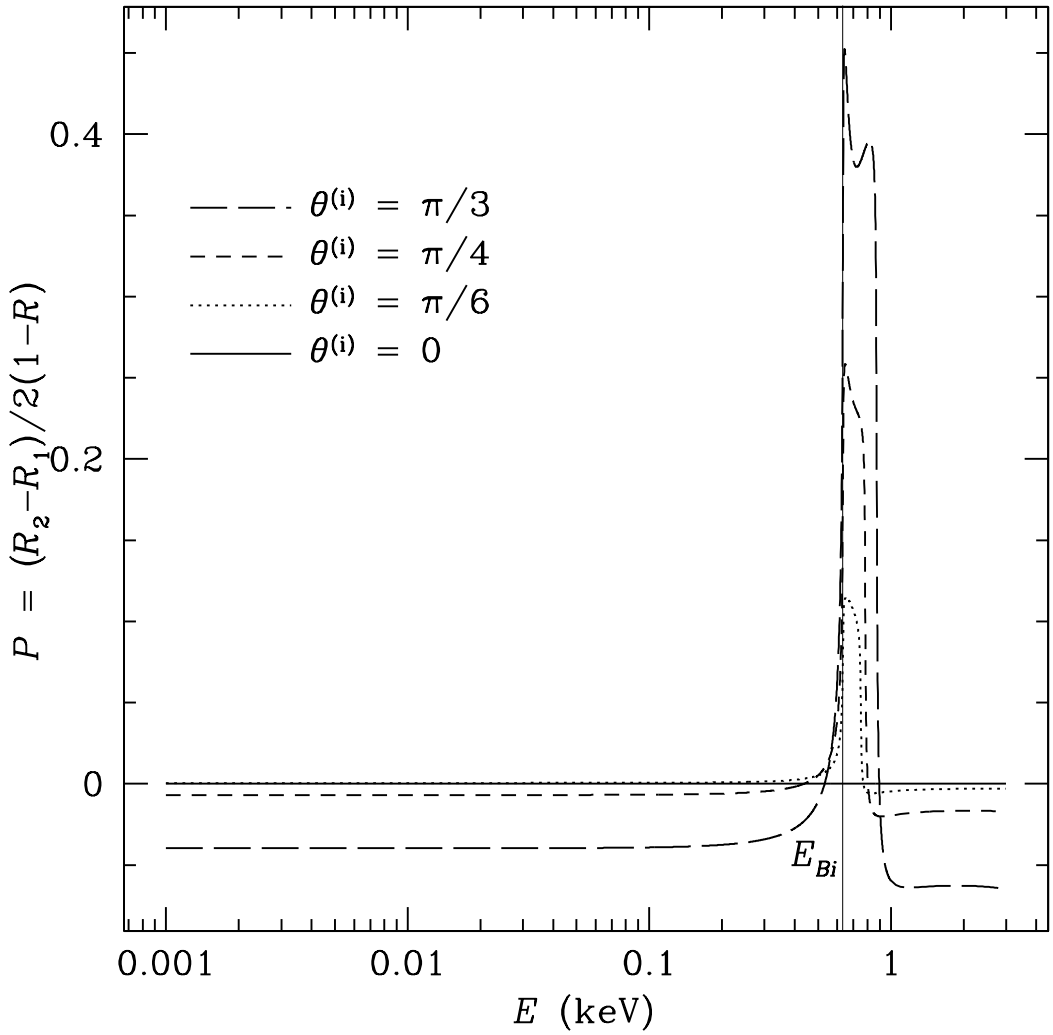

Figure 2.9: Same as Fig. 2.8, except for a H surface at $B = 10^{14}$ G. There is a slight net linear polarization perpendicular to the **k**-**B** plane ($P \sim -5\%$), except around E_{Bi} where the polarization peaks parallel to the **k**-**B** plane.

we show the angle-averaged emissivity, $\langle 1 - R \rangle = F_\nu / [\pi B_\nu(T)]$, for a specific case with $B = 5 \times 10^{13}$ G, $T = 10^6$ K and $\theta_B = 0.7 \times \pi/2$ (Fig. 2.10); this should be directly compared to Fig. 5 of Turolla et al. Their results show no emission below ~ 0.1 keV, and they find that this "cutoff" feature becomes more pronounced as the magnetic field inclination angle increases and the field strength decreases. Our calculations clearly do not show this behavior (see the solid line of Fig. 2.10).

These discrepancies stem from at least two differences in the reflectivity calculation: (1) Turolla et al. neglected the effect of ion motion in their expression for the plasma dielectric tensor (see the end of §2.1.2). This strongly affects the emissivity at $E \lesssim E_{Bi}$ (see also Figs. 2.2–2.7). (2) Even when the ion motion is neglected (by setting $m_i = \infty$), our result (see the dashed-line in Fig. 10) does not reveal any low-energy cutoff. It is most likely that this difference arises from the "one-mode" description for the transmitted radiation adopted by Turolla et al.: when the real part of the index of refraction of a mode is less than zero or the imaginary part of the index of refraction exceeds a threshold value, this mode is neglected by Turolla et al. in the transmitted wave. Such treatment is incorrect and can lead to significant errors in the reflectivity calculation. The inclusion of collisional damping gives rise to complex values for the index of refraction, which lead to transmitted waves with a propagating (oscillatory) part multiplied by a decaying amplitude (see Appendix A.2). While the damping factor for such waves can be large if the index of refraction has a large imaginary part, the propagating piece allows energy to be carried across the vacuum-surface boundary; these waves cannot be ignored in the reflectivity calculation.

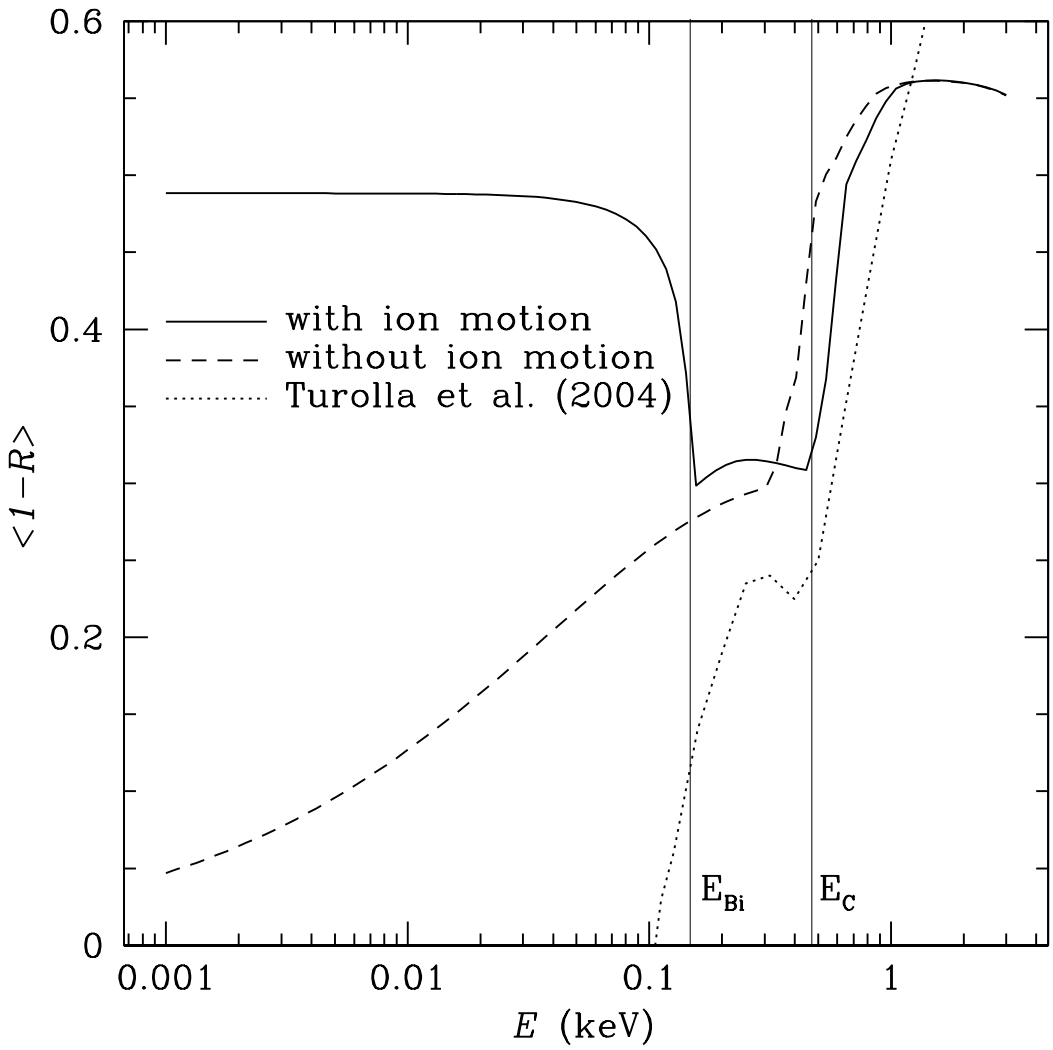

Figure 2.10: Angle-averaged intensity $\langle 1-R \rangle$ as defined in §2.3.1 for $B = 5\times10^{13}$ G, $T = 10^6 K$, $\theta_B = 0.7 \times \pi/2$. The solid line shows our result including the ion effect, while the dashed-line shows the results when the ion motion is neglected. For comparison, the dotted line shows data from Fig. 5 of Turolla et al. (2004).

2.4 Discussion

As discussed in Chapter 1, many isolated NSs display no spectral features in thermal emission, and are well fit by a blackbody spectrum. The most thoroughly studied object of this type is RX J1856.5−3754, which is well fit in the X-ray by a blackbody spectrum at temperature $kT_{bb}^{\infty} = 63.5$ eV, with emission radius $R_{\infty} = 4.4\,(d/120\text{ pc})$ km (where d is the distance). This X-ray blackbody underpredicts the optical flux by a factor of 7. Pavlov & Zavlin (2003) review several models involving a non-uniform temperature on the surface of the NS, in which the X-ray photons are emitted by a hot spot. By varying the temperature distribution and assuming blackbody emission from each surface element, a reasonable fit to the X-ray and optical data can be achieved (see also Braje & Romani, 2002; Trümper et al., 2004). Nevertheless, the nearly perfect X-ray blackbody spectrum of RX J1856.5−3754 is surprising.

If the NS surface is indeed in a condensed form (see §2.1.1), the emissivity will be determined by the properties of the condensed matter. Our calculations (§2.2 and §2.3) show that the emission spectrum resembles a diluted blackbody, with a reduction factor in the range of $J = 0.4 - 1$, depending on the photon energy (see Figs. 2.2–2.6). This would increase the inferred NS emission radius by a factor of $J^{-1/2}$. The weak "absorption" features in the emission spectrum are associated with the ion cyclotron and electron plasma frequencies in the condensed medium. We note that the emissivity and spectrum presented in this paper correspond to a local patch of the NS. When the emission from different surface elements are combined to form a synthetic spectrum, these absorption features are expected to be smoothed out further because of the magnetic field variation across the NS surface.

In our calculations, we have assumed a perfectly smooth surface. This is valid if the condensed matter is in a liquid state, as is likely to be the case for a H condensate (see §2.1.1). For Fe, the condensed surface is most likely a solid with a rough surface. Although it is not possible to predict the scale and shape of the surface irregularities, their maximum possible height $h_{\max}$ can be estimated from the requirement that the stress nonuniformity $\sim \rho g h$ is small compared to the shear stress $\mu\theta_s$. Using a shear modulus $\mu \simeq 0.1\, n_i\, (Ze)^2/a_i$ (Ogata & Ichimaru, 1990) and the maximum strain angle $\theta_s = 10^{-3}\theta_{-3}$, we find $h_{\max} \sim 2 \times 10^{-5}\, \theta_{-3}\, Z^2 A^{-4/3} \rho_1^{1/3} g_{14}^{-1}$ cm (where $g = 10^{14} g_{14}$ cm s^{-2} is the NS surface gravity). For a condensed Fe surface at the density given by eq. (2.1), we have $h_{\max} \sim 4 \times 10^{-4}\, \theta_{-3}\, B_{12}^{2/5}$ cm (for a NS with $R = 10$ km and $M = 1.4\, M_\odot$). Clearly, the scale of the surface roughness can easily be much larger than the photon wavelength (~ 10Å). As illustrated in Fig. 2.11, the surface may be much less reflective than the results shown in §2.3, and the emission will be closer to blackbody.

The emission from a condensed NS surface is distinct from atmospheric emission in several respects: (1) Atmospheric emission generally possesses a hard spectral tail (although this tail is somewhat suppressed by the QED effect for $B \gtrsim 10^{14}$ G; see Chapter 3), whereas the condensed surface emission does not; (2) The spectrum of a cool NS atmosphere can have both cyclotron and atomic absorption features which are suppressed for $B \gtrsim 10^{14}$ G–the broad (cyclotron and plasma) features of condensed surface emission persist even in the magnetar field regime (if they are not smoothed out by variations of surface B fields or by the rough surface effect); (3) The polarization signature of condensed matter emission is qualitatively different from that of atmospheric emission. All of these differences can serve as diagnostics for the physical condition of the emission region.

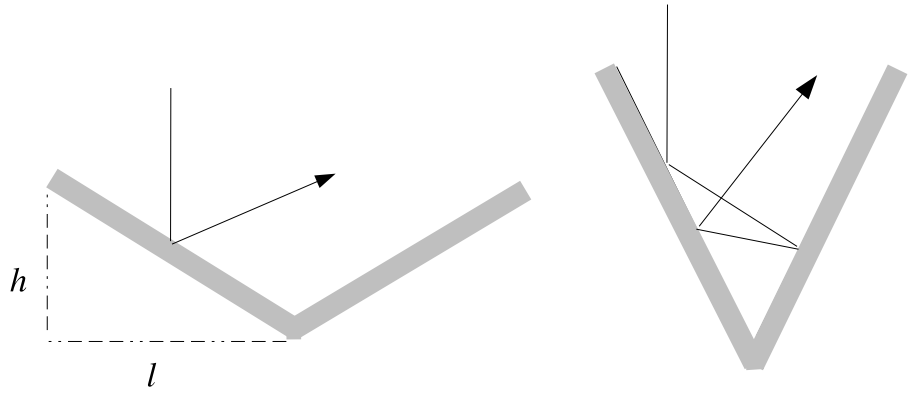

Figure 2.11: Effect of surface roughness on the reflectivity. The surface roughness is characterized by a vertical scale h and a horizontal scale l, both much larger than the photon wavelength. For the idealized "triangular" surface, a normal incident ray goes through at least two reflections if $\theta = \tan^{-1}(l/h) < 60°$, at least three reflections if $\theta < 36°$, at least four reflections if $\theta < 180°/7$, etc. Thus, the net reflectivity of the rough surface is $\ll 1$ if $h >$ a few $\times\, l$, and the emission spectrum will be close to blackbody.

At the surface temperature of AXPs and SGRs ($T \simeq 5 \times 10^6$ K), H is unlikely to be condensed, but Fe condensation is possible. The dim, isolated NSs have lower temperatures ($T \lesssim 10^6$ K), and if they possess magnetar-like fields, condensation is likely. In particular, the blackbody X-ray spectra of RX J1856.5−3754 ($kT \simeq$ 64eV) and RX J0420.0−5022 ($kT \simeq 45$eV; see Haberl et al. 2004a) could arise from condensed surface emission (a non-smooth Fe surface at $B \gtrsim 10^{12}$ G), although to account for the optical data, non-uniform surface temperatures are still needed.

Chapter 3

Atmosphere Models of Pulsars and Magnetars

In Chapter 1 we review current observational challenges to models of thermal emission from isolated NSs. For most NSs, the spectrum of thermal radiation is formed in the atmosphere layer (with scale height $\sim 0.1-10$ cm and density $10^{-3}-10^{3}$ g cm^{-3}) that covers the stellar surface. Thus, to properly interpret observations of NS surface emission, detailed modeling of NS atmospheres in strong magnetic fields is required. In recent years, a great deal of effort has been spent on the development of reliable NS atmosphere models. The first magnetic NS atmosphere models were constructed by Shibanov et al. (1992) (see also Pavlov et al., 1995; Zavlin & Pavlov, 2002) who focused on moderate field strengths $B \sim 10^{12}$–10^{13} G and assumed full ionization (see Zane et al., 2000, for atmosphere models with accretion). Similar ionized models for the magnetar field regime ($B \gtrsim 10^{14}$ G) were studied by Zane et al. (2001); Özel (2001); Ho & Lai (2001, 2003). An inaccurate treatment of the free-free opacities in the earlier models (Pavlov et al., 1995) was corrected by Potekhin & Chabrier (2003), and the correction has been incoporated into later models (Ho et al., 2003; Ho & Lai, 2004). Recent works (Lai & Ho, 2002, 2003a; Ho & Lai, 2003) have shown that in the magnetar field regime, the effect of strong-field quantum electrodynamics significantly influences the emergent atmosphere spectrum. In particular, vacuum polarization gives rise to a resonance phenomenon, in which photons can convert from the high-opacity mode to the low-opacity one and vice versa. This vacuum resonance tends to soften the hard spectral tail due to the non-greyness of the atmosphere and suppress the width

of absorption lines (for a qualitative explanation, see Lai & Ho, 2003a). Even for modest field strengths ($B \lesssim 10^{14}$ G), vacuum polarization can still leave a unique imprint on the X-ray polarization signal (see Lai & Ho 2003b and Chapter 4).

A strong magnetic field greatly increases the binding energies of atoms, molecules and other bound species (see Lai, 2001), therefore, these bound states may have appreciable abundances in the NS atmosphere (Lai & Salpeter, 1997; Potekhin et al., 1999). Recently, a thermodynamically consistent equation of state and opacities for magnetized ($B = 10^{12} - 10^{15}$ G), partially ionized H plasma have been obtained (Potekhin et al., 1999; Potekhin & Chabrier, 2003, 2004). The effect of bound atoms on the dielectric tensor of the plasma has also been studied (Potekhin et al., 2004). These have been incorporated into the first partially ionized, magnetic NS atmosphere models (Ho et al., 2003; Potekhin et al., 2004).

While previous works have clearly identified the importance and trend of the vacuum polarization effect (Lai & Ho, 2002, 2003a), so far the implementation of the effect in NS atmosphere models (Ho & Lai, 2003, 2004) has been based on approximations (see §3.1). All previous studies of magnetic NS atmospheres rely on solving the transfer equations for the specific intensities of the two photon modes. As discussed in Lai & Ho (2003a) and reviewed in §3.1 below, these equations cannot properly handle the vacuum-induced mode conversion phenomenon because mode conversion intrinsically involves interference between different modes.

We provide a new, quantitatively accurate treatment of vacuum polarization effects in radiation transfer for fully ionized NS atmospheres. Our work confirms the semi-quantitative results obtained in previous works based on an approximate treatment of the vacuum resonance (Ho & Lai, 2003; Lai & Ho, 2003a). Moreover, our new treatment allows us to quantitatively predict the spectral and polarization

properties of NS atmospheres with field strengths varying from 10^{12} G to 10^{15} G.

3.1 Effect of Vacuum Polarization on Radiative Transfer

Before describing our quantitative treatment of the vacuum polarization effect in NS atmospheres, it is useful to summarize the basic physics of the effect (see also Lai & Ho, 2003a) and discuss the limitations of previous treatments.

Photons in magnetized NS atmospheres (with energy $E \ll E_{Be} = \hbar eB/m_e c$, the electron cyclotron energy) usually propagate in two distinct polarization states, the ordinary mode (denoted by "O") and the extraordinary mode (denoted by "X"), which are polarized (almost) parallel and perpendicular to the plane made by the magnetic field and direction of photon propagation, respectively. In strong magnetic fields, the dielectric tensor describing the atmospheric plasma of a NS must be corrected for QED vacuum effects (Gnedin et al., 1978; Meszaros & Ventura, 1979; Pavlov & Shibanov, 1979; Meszaros, 1992). For a photon propagating in a medium of *constant* density ρ, the plasma and vacuum contributions to the dielectric tensor "cancel" each other out at a particular energy given by

$$E_V = 1.02\,(Y_e\,\rho_1)^{1/2}\,B_{14}^{-1} f_B \text{ keV}, \tag{3.1}$$

where $Y_e = Z/A$ ($Z,\ A$ are the atomic number and mass number, respectively), $\rho_1 = \rho/(1 \text{ g cm}^{-3})$, $B_{14} = B/(10^{14} \text{ G})$, and $f_B \sim 1$ is a slowly varying function of B [see eq. (2.41) of Ho & Lai (2003)]. At the resonance, both modes become circularly polarized. A number of previous papers (e.g., Meszaros, 1992) emphasized the sharp X-mode opacity feature associated with the resonance (see Fig. 3.1). It might seem that to understand the vacuum polarization effect in radiative transfer, all one needs to do is to include this spike in the opacity (e.g., Özel, 2003). However,

this treatment neglects the conversion of photon modes at the resonance.

A more useful way to understand the effects of the vacuum resonance is to consider a photon with given energy E, traversing the density gradient of a NS atmosphere. The photon will encounter the vacuum resonance at the density

$$\rho_V = 0.96\, Y_e^{-1} E_1^2\, B_{14}^2\, f_B^{-2}\ \mathrm{g\ cm^{-3}}, \tag{3.2}$$

where $E_1 = E/(1\ \mathrm{keV})$. Lai & Ho (2002) showed that the photon undergoes resonant mode conversion when the adiabatic condition $E \gtrsim E_{ad}$ is satisfied, with[1]

$$E_{ad} = 2.52 \left[f_B \tan\theta_{kB} \left| 1 - (E_{Bi}/E)^2 \right| \right]^{2/3} \left(\frac{1\ \mathrm{cm}}{H_\rho} \right)^{1/3}, \tag{3.3}$$

where θ_{kB} is the angle between the magnetic field and direction of propagation, $E_{Bi} = 0.63(Z/A)$ keV is the ion cyclotron energy, and $H_\rho \equiv |ds/d\ln\rho|$ is the density scale height along the ray. Thus, an adiabatic O-mode photon encountering the vacuum resonance will convert into an X-mode photon, and vice-versa. In general, for intermediate energies $E \sim E_{ad}$, photons undergo partial conversion, in which an O-mode converts to a X-mode (and vice-versa) with probability $1 - P_{\mathrm{jump}}$, where P_{jump} is the non-adiabatic jump probability given by

$$P_{\mathrm{jump}} = \exp\left[-\frac{\pi}{2} (E/E_{ad})^3 \right]. \tag{3.4}$$

Due to free-free absorption, the X-mode opacity is suppressed relative to the O-mode by a factor of $(E_{Be}/E)^2$, where the electron cyclotron energy is $E_{Be} = 1158\ B_{14}$ keV; thus, the mixing of photon modes at the resonance can have a drastic effect on the radiative transfer. For magnetic field strengths satisfying (Lai & Ho, 2003a; Ho & Lai, 2004)

$$B \gtrsim B_l \simeq 6.6 \times 10^{13}\, T_6^{-1/8} E_1^{-1/4} S^{-1/4}\ \mathrm{G}, \tag{3.5}$$

[1]Since E_{ad} depends on E, one needs to solve for $E \gtrsim E_{ad}$ to determine the adiabatic region. See Fig. 6 of Lai & Ho (2003a).

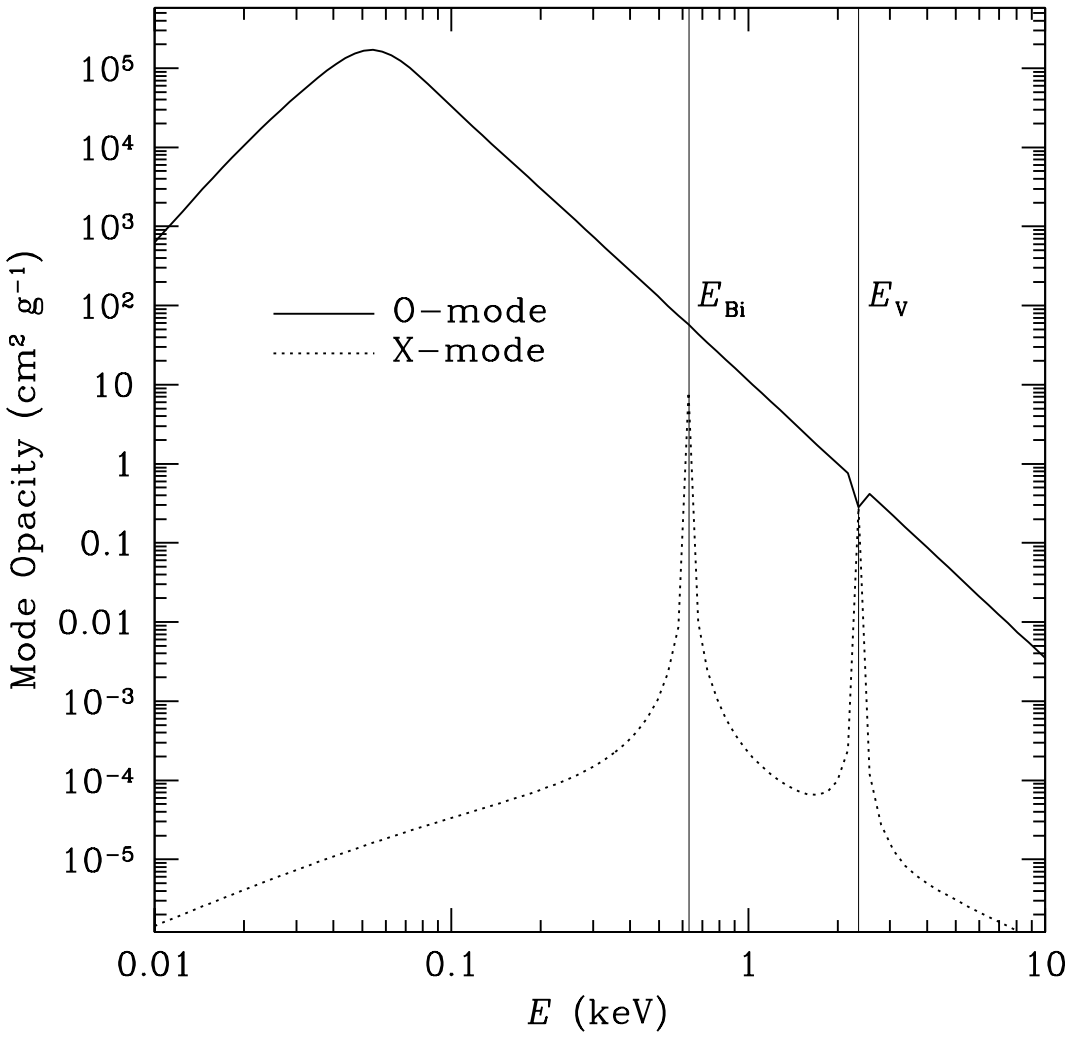

Figure 3.1: Photon free-free absorption opacities for X and O polarization modes as a function of energy at $B = 10^{14}$ G, $T = 10^6$ K, $\theta_{kB} = \pi/4$ and $\rho = 5.4$ g cm^{-3}. Vacuum polarization induces the sharp resonance feature for the X-mode opacity at E_V. This opacity spike can affect the emergent radiation spectrum from magnetized NSs, but does not include all the effects associated with the vacuum resonance.

where $T_6 = T/(10^6 \text{ K})$ and $S = 1 - e^{-E/kT}$, the vacuum resonance density lies between the X-mode and O-mode photospheres for typical photon energies, leading to suppression of spectral features and softening of the hard X-ray tail characteristic of ionized H atmospheres. For "normal" magnetic fields, $B \lesssim B_l$, the vacuum resonance lies outside both photospheres, and the emission spectrum is unaltered by the vacuum resonance, although the observed polarization signals are still affected (Lai & Ho, 2003b).

In their implementation of the vacuum resonance effect in NS atmosphere models, Ho & Lai (2003) considered two limiting cases: (1) complete mode conversion ($P_{\rm jump} = 0$), which is equivalent to assuming that $E \gg E_{ad}$ is satisfied for all photon energies; (2) no conversion ($P_{\rm jump} = 1$), which is equivalent to assuming $E \ll E_{ad}$ for all photons. In the former case, all X-mode photons are converted to the O-mode at the resonance (and vice-versa), whereas in the latter, such conversion is neglected. In both cases, radiative transfer equations based on photon modes can be used, as long as one properly defines the modes across the resonance (Ho & Lai, 2003). We expect that the complete and no conversion limits bracket the correct solution. Case (2) only includes the narrow opacity spike associated with the resonance. Lai & Ho (2002) estimated the width of this opacity spike and emphasized the importance of resolving it. In both limits, vacuum resonance has the same qualitative effects on the emergent spectrum, e.g., suppression of lines and softening of hard spectral tails (Lai & Ho, 2002; Ho & Lai, 2003), although for $B \sim (\text{a few} \times 10^{13}) - 10^{14}$ G, appreciable quantitative differences in the spectra using the two limits are produced (Ho & Lai, 2004).

As mentioned before, all studies of radiative transfer in magnetized NS atmospheres have relied on solving the transfer equations for the specific intensities of

the two photon modes (e.g., Meszaros, 1992; Zavlin & Pavlov, 2002). These equations cannot properly handle the vacuum-induced mode conversion phenomenon. In particular, photons with energies 0.3-2 keV are only partially converted across the vacuum resonance (this is the energy range in which the bulk of the radiation emerges and spectral lines are expected for $B \sim 10^{14}$ G). In addition, the phenomenon of mode collapse (when the X and O-modes become degenerate) occurs when dissipative effects are included in the plasma dielectric tensor, and the concomitant breakdown of the Faraday depolarization condition near the resonance further complicates the standard treatment of radiative transfer based on normal modes. As shown by Gnedin & Pavlov (1974), the modal description of radiative transfer is valid only in the limit $|\mathrm{Re}(n_\mathrm{X} - n_\mathrm{O})| \gg |\mathrm{Im}(n_\mathrm{X} + n_\mathrm{O})|$, where n_X and n_O are the indices of refraction corresponding to the X and O-modes, respectively. Ho & Lai (2003) showed that, for a narrow range of energies around the vacuum resonance, this condition can be violated, and the violation becomes especially pronounced in the magnetar field regime. It is not obvious whether the mode collapse significantly alters the radiative transfer. Thus, to account for the vacuum resonance effect in a quantitative manner, one must solve the transfer equations in terms of the photon intensity matrix (Lai & Ho, 2003a) and properly take into account the probability of mode conversion.

3.2 Method

3.2.1 Partial Mode Conversion using Mode Equations

Radiative Transfer Equation

For our models, we consider plane-parallel, fully ionized H or He atmospheres, with the magnetic field oriented normal to the surface. The standard method used in all previous work involves solving the coupled radiative transfer equations for the two modes of photon propagation. These are given by

$$\pm\mu\frac{\partial I_\nu^j(\tau,\pm\mu)}{\partial\tau} = \frac{\kappa_j^{tot}}{\kappa_T}\left[I_\nu^j(\tau,\pm\mu) - S_\nu^j(\tau,\pm\mu)\right] \tag{3.6}$$

where $I_\nu^j(\tau,\mu)$ is the specific intensity for mode j, $\mu = \hat{\mathbf{k}}\cdot\hat{\mathbf{z}} \geq 0$, $\kappa_j^{tot} = \kappa_j^{\rm ff} + \kappa_j^{\rm sc}$ is the total opacity (with contributions from free-free absorption and scattering, see below), $\kappa_T = 0.4$ cm^2 g^{-1} is the Thomson scattering opacity, τ is the Thomson optical depth (defined by $d\tau = -\rho\,\kappa_T\,dz$), and S_ν^j is the source function, defined below. Eq. (3.6) is solved subject to the constraints of hydrostatic and radiative equilibria, as well as constant radiative flux $F_{\rm rad}$, given by:

$$P = \frac{g}{\kappa_T}\tau, \tag{3.7}$$

$$\int_0^\infty d\nu \sum_{j=1}^{2}\kappa_j^{abs}\left(\frac{B_\nu}{2} - J_\nu^j\right) = 0, \tag{3.8}$$

$$F_{\rm rad} = 2\pi\sum_{j=1}^{2}\int_0^\infty d\nu\int_0^1 d\mu\mu\left[I_\nu^j(\mu) - I_\nu^j(-\mu)\right] = \sigma_{\rm sb}T_{\rm eff}^4 \tag{3.9}$$

where P is the pressure of electrons and ions, $g = \left(\frac{GM}{R^2}\right)\left(1-\frac{2GM}{Rc^2}\right)^{-1/2} = 2.4\times 10^{14}$ cm s^{-2} is the surface gravitational acceleration (we adopt $M = 1.4$ M$_\odot$ and $R = 10$ km throughout our calculations), $J_\nu^j \equiv (1/2)\int_0^1 d\mu\,[I_\nu^j(\mu) + I_\nu^j(-\mu)]$ is the

mean specific intensity, B_ν is the Planck function, and $T_{\rm eff}$ is the effective temperature of the atmosphere. To integrate eq. (3.6) subject to the conditions of (3.7)-(3.9), we assume the ideal gas equation of state for both protons and electrons; that is, electron degeneracy effects are neglected. For the regime investigated below ($B \sim 10^{13} - 5 \times 10^{14}$ G, $T_{\rm eff} \sim 10^6 - 5 \times 10^6$ K), the field is strongly quantizing (the electrons are restricted to the ground Landau level), and the temperature is less than the critical magnetic temperature at which the effects of Landau quantization are smeared out (Lai, 2001). However, in all but the deepest layers of the atmosphere, the temperature is much larger than the Fermi temperature, and the ideal gas equation of state may be used to describe the electron pressure (see Fig. 6 of Lai, 2001). Numerical calculations by Ho & Lai (2001) show that the effect of this approximation on the atmosphere is negligible.

In general, thermal conduction due to electrons also contributes to the total flux. However, we show in Appendix B that the conduction flux is always less than a few percent of the total flux in the atmosphere region of interest, and is therefore neglected.

Photon Modes and Opacities

The properties of magnetized atmospheric plasma can be described by a complex dielectric tensor (Ginzburg, 1970). In a coordinate system with the magnetic field aligned with the z-axis, the plasma contribution to the dielectric tensor takes the

form (Lai & Ho, 2003a):[2]

$$\left[\boldsymbol{\epsilon}^{(pl)}\right] = \begin{pmatrix} \epsilon & i\,g & 0 \\ -i\,g & \epsilon & 0 \\ 0 & 0 & \eta \end{pmatrix}, \tag{3.10}$$

where

$$\epsilon \pm g \approx 1 - \frac{v_e(1+i\gamma_{ri}) + v_i(1+i\gamma_{re})}{(1+i\gamma_{re} \pm u_e^{1/2})(1+i\gamma_{ri} \mp u_i^{1/2}) + i\gamma_{ei}^{\perp})} \tag{3.11}$$

$$\eta \approx 1 - \frac{v_e}{1+i(\gamma_{ei}^{\parallel}+\gamma_{re})} - \frac{v_i}{1+i(\gamma_{ei}^{\parallel}+\gamma_{ri})}. \tag{3.12}$$

In eqs. (3.11)–(3.12) we have defined the dimensionless ratios $u_e \equiv (E_{Be}/E)^2$, $u_i \equiv (E_{Bi}/E)^2$, $v_e \equiv (E_{pe}/E)^2$, $v_i \equiv (E_{pi}/E)^2$, where $E_{pe} = \hbar(4\pi n_e e^2/m_e)^{1/2} = 0.02871(Y_e\,\rho_1)^{1/2}$ keV is the electron plasma energy, and $E_{pi} = (Zm_e/Am_p)E_{pe} = 6.70\times10^{-4}\,Y_e\,\rho_1^{1/2}$ keV is the ion plasma energy. The dimensionless damping rates $\gamma_{ei}^{\perp,\parallel} = \nu_{ei}^{\perp,\parallel}/\omega$ (for electron-ion collisional damping), $\gamma_{re} = \nu_{re}/\omega$ (for electron radiative damping), and $\gamma_{ri} = \nu_{ri}/\omega$ (for ion radiative damping) are given by

$$\gamma_{ei}^{\perp,\parallel} = 9.2\times10^{-5}\frac{Z^2\,\rho_1}{A\,T_6^{1/2}\,E_1^2}\left(1-e^{-E/k_BT}\right)\,g_{\perp,\parallel}^{\rm ff}, \tag{3.13}$$

$$\gamma_{re} = 9.5\times10^{-6}E_1, \tag{3.14}$$

$$\gamma_{ri} = 5.2\times10^{-9}\frac{Z^2}{A}E_1. \tag{3.15}$$

The quantities $g_\perp^{\rm ff}$ and $g_\parallel^{\rm ff}$ are the velocity-averaged magnetic Gaunt factors perpendicular and parallel to the magnetic field, respectively; they are calculated using eqs. (4.4.9)-(4.4.12) from Meszaros (1992).[3] This calculation includes contributions

[2]Note that eq. (13) of Lai & Ho (2003a) should be $\gamma_{ei}^{\pm} = \gamma_{ei}^{\perp}(1+\frac{m_e}{Am_p}) \approx \gamma_{ei}^{\perp}$. This substitution should be applied to all the appropriate equations in Lai & Ho (2003a).

[3]Note that eq. (4.4.12) of Meszaros (1992) should be $a_\pm = (p \pm [p^2 + 2m\hbar\omega]^{1/2})^2/(2mk_BT)$.

from electrons in the ground Landau level only. Gaunt factors including contributions from excited states have been derived by Potekhin & Chabrier (2004). Nevertheless, for energies well below E_{Be}, the differences between the two calculations are negligible (Potekhin, 2006). Fig. 3.2 shows the magnetic Gaunt factors as a function of photon energy for $T = 10^6$ K at several magnetic field strengths (note that the Gaunt factors depend weakly on temperature). The solid curves show the value of $g^{\rm ff}$ perpendicular to the magnetic field while the dashed curves show the result parallel to the field. From bottom to top, the curves correspond to $B = 10^{13}, 4\times10^{13}, 7\times10^{13}, 10^{14}$, and 5×10^{14} G. In the energy range $E \sim 0.1-1$ keV, the Gaunt factors have magnitudes of order unity, however, outside of this range they can vary in magnitude greatly (from ~ 60 in the optical band to ~ 0.1 in the X-ray band). The strong energy dependence of $g^{\rm ff}$ has a significant effect on the opacities and hence radiative transfer; it is thus critical to properly evaluate these factors.

Vacuum contributions to the dielectric tensor can be taken into account by making the following substitutions into the tensor of eq. (3.10):

$$\epsilon \rightarrow \epsilon' = \epsilon + a - 1, \quad \eta \rightarrow \eta' = \eta + a + q - 1, \tag{3.16}$$

where a and q are vacuum parameters given by the expressions in, for example, Heyl & Hernquist (1997) and Potekhin et al. (2004) (the latter contains general fitting formulas). Solving Maxwell's equations for the anisotropic medium yields two modes of propagation. In a coordinate system where the wave vector $\mathbf{k}$ is along the z-axis and the magnetic field lies in the xz plane (such that $\hat{\mathbf{k}}\times\hat{\mathbf{B}} = -\sin\theta_{kB}\hat{\mathbf{y}}$), the mode eigenvectors can be written as

$$\mathbf{e}_\pm = \frac{1}{(1 + |K_\pm|^2 + |K_{z\pm}|^2)^{1/2}}(iK_\pm, 1, iK_{z\pm}), \tag{3.17}$$

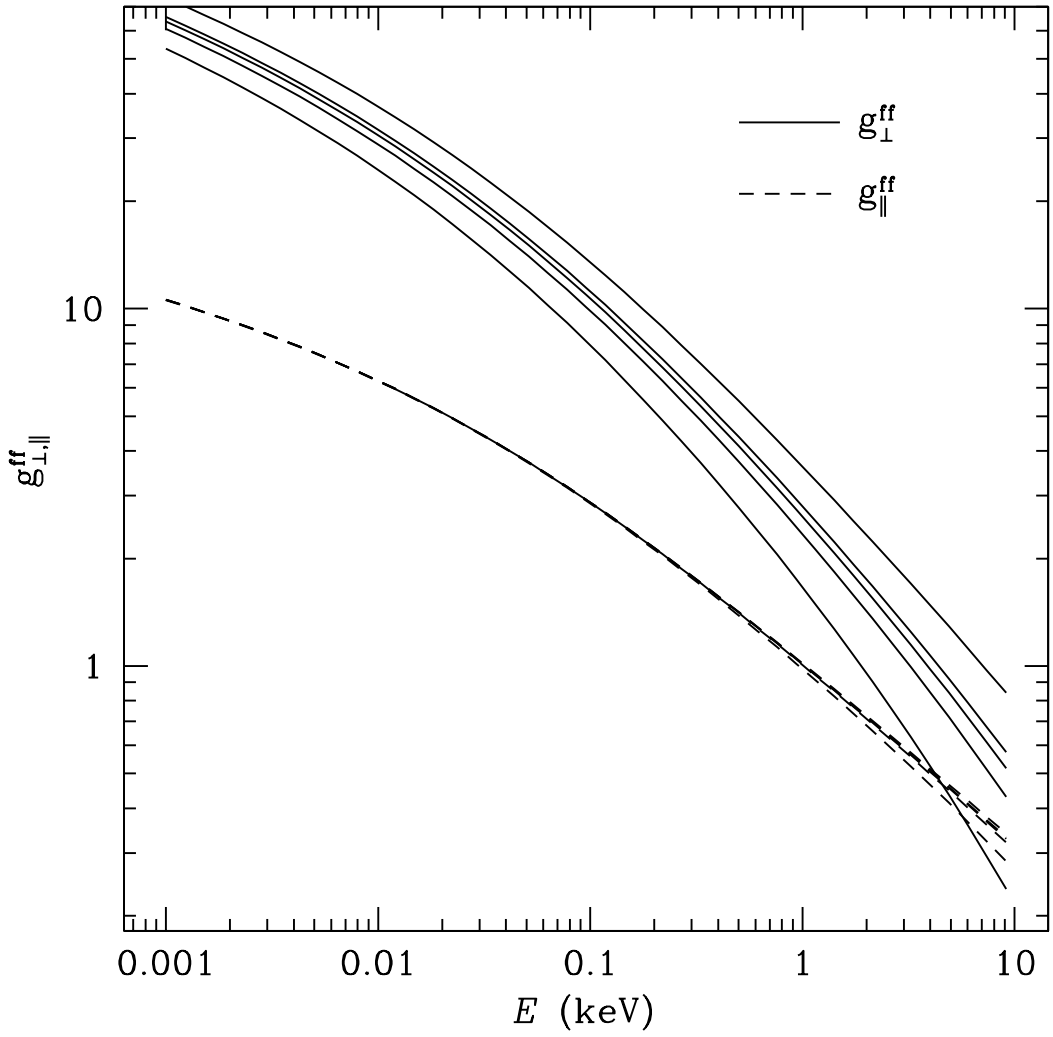

Figure 3.2: Magnetic Gaunt factors as a function of photon energy for $T = 10^6$ K at several magnetic field strengths. The solid curves show the Gaunt factors perpendicular to the magnetic field, while the dashed curves show the Gaunt factors parallel to the field. From bottom to top, the curves correspond to $B = 10^{13}, 4 \times 10^{13}, 7 \times 10^{13}, 10^{14}$, and 5×10^{14} G. Note the strong energy dependence and deviations of the Gaunt factors from unity.

where the ellipticity $K_\pm = -ie_x/e_y$ of mode $\pm$ is given by

$$K_\pm = \beta \pm \sqrt{\beta^2 + r}, \tag{3.18}$$

with $r = 1+(m/a)\sin^2\theta_{kB}$ (m is another vacuum polarization parameter; see Heyl & Hernquist 1997; Potekhin et al. 2004), and the polarization parameter β is

$$\beta = -\frac{\epsilon'^2 - g^2 - \epsilon'\eta'(1+m/a)}{2g\eta'}\frac{\sin^2\theta_{kB}}{\cos\theta_{kB}}. \tag{3.19}$$

The z-components of the mode eigenvectors are given by

$$K_{z\pm} = -\frac{(\epsilon-\eta-g)\sin\theta_{kB}\cos\theta_{kB}K_\pm + g\sin\theta_{kB}}{\epsilon\sin^2\theta_{kB} + (\eta+q)\cos^2\theta_{kB} + a - 1}. \tag{3.20}$$

Note that when the modes are labelled according to eq. (3.18), the $K_\pm$ vary continuously across the vacuum resonance ($\beta = 0$), and do not cross each other in the absence of dissipation (Lai & Ho, 2003a). Another way of labeling the modes, commonly adopted in the literature (e.g., Meszaros, 1992), is

$$K_j = \beta\left[1 + (-1)^j\left(1 + \frac{r}{\beta^2}\right)^{1/2}\right]. \tag{3.21}$$

According to this labeling scheme, $j = 1$ corresponds to the X-mode ($|K_1| < 1$) and $j = 2$ corresponds to the O-mode ($|K_2| > 1$). Obviously, K_1 and K_2 are not continuous functions across the vacuum resonance. It is also clear that a given + mode (or - mode) which manifests as the X-mode (O-mode) before the resonance switches character after the resonance.

Using the mode eigenvectors and the componenets of the dielectric tensor, expressions for the free-free absorption and scattering opacities can be obtained. The cyclic components of the mode eigenvectors in a rotating frame with the magnetic field along the z-axis are:

$$\left|e^j_\pm\right|^2 = \left|\frac{1}{\sqrt{2}}(e^j_X + ie^j_Y)\right|^2 = \frac{1 \pm |K_j\cos\theta_{kB} + K_{zj}\sin\theta_{kB}|^2}{2(1+|K_j|^2+|K_{zj}|^2)}, \tag{3.22}$$

$$\left|e^j_o\right|^2 = \frac{\left|K_j\sin\theta_{kB} - K_{zj}\cos\theta_{kB}\right|^2}{1+|K_j|^2+|K_{zj}|^2}. \tag{3.23}$$

Note that in the above expression, j indicates the mode, and the $\pm$ subscript should not be confused with the $K_\pm$ labeling of photon modes. The free-free absorption opacity for mode j can be written (Lai & Ho, 2003a):

$$\kappa_j^{\rm ff} = \kappa_+^j |e_+^j|^2 + \kappa_- |e_-^j|^2 + \kappa_o |e_o^j|^2, \tag{3.24}$$

with

$$\kappa_\pm = \frac{\omega}{c\rho} v_e \Lambda_\pm \gamma_{ei}^\perp, \tag{3.25}$$

$$\kappa_o = \frac{\omega}{c\rho} v_e \gamma_{ei}^\parallel, \tag{3.26}$$

$$\Lambda_\pm = \left[(1 \pm u_e^{1/2})^2 (1 \mp u_i^{1/2})^2 + \gamma_\pm^2 \right]^{-1}, \tag{3.27}$$

$$\gamma_\pm = \gamma_{ei}^\perp + (1 \pm u_e^{1/2}) \gamma_{ri} + (1 \mp u_i^{1/2}) \gamma_{re}. \tag{3.28}$$

Note that these expressions include the contribution of electron-ion Coulomb collisions to the free-free absorption opacity in a consistent way. They correct the free-free opacity adopted in earlier papers (e.g. Pavlov et al., 1995; Ho & Lai, 2001), and they agree with the correct expressions given in Potekhin & Chabrier (2003), and those used by Ho et al. (2003).

The scattering opacity from mode j into mode i is given by Ventura (1979) (see also Ho & Lai, 2001):

$$\begin{aligned} \kappa_{ji}^{sc} = {} & Y_e \kappa_T \sum_{\alpha=-1}^{1} \left[(1 + \alpha u_e^{1/2})^2 + \gamma_e^2 \right]^{-1} |e_\alpha^j|^2 A_\alpha^i + \\ & \left(\frac{Z^2 m_e}{A m_p} \right)^2 \frac{\kappa_T}{A} \sum_{\alpha=-1}^{1} \left[(1 - \alpha u_i^{1/2})^2 + \gamma_i^2 \right]^{-1} |e_\alpha^j|^2 A_\alpha^i \end{aligned} \tag{3.29}$$

where $\gamma_e = \gamma_{ei}^\alpha + \gamma_{re}$, $\gamma_i = \gamma_{ei}^\alpha + \gamma_{ri}$, and $A_\alpha^i = (3/4) \int_{-1}^{1} d\mu' |e_\alpha^i|^2$. The total scattering opacity from mode j is then $\kappa_j^{sc} = \sum_i \kappa_{ji}^{sc}$.

Source Function

The source function in eq. (3.6) can be written as

$$S_\nu^j(\mu) = \frac{\kappa_j^{\rm ff}(\mu)}{\kappa^{\rm tot}(\mu)}\frac{B_\nu}{2} + \frac{2\pi}{\kappa_j^{tot}(\mu)}\sum_{i=1}^{2}\int_0^1 d\mu' \frac{d\kappa^{sc}(\mu' i \rightarrow \mu j)}{d\Omega}\left[I_\nu^j(\mu) + I_\nu^i(-\mu)\right] \quad (3.30)$$

where (Ventura, 1979)

$$\frac{d\kappa^{sc}(j\mu \rightarrow i\mu')}{d\Omega'} = \frac{3}{8\pi}Y_e\kappa_T\left|\sum_{\alpha=-1}^{1}\frac{1}{1+\alpha u_e^{1/2}}\, e_\alpha^{j\,*} e_\alpha^i\right|^2 + \frac{3}{8\pi}\left(\frac{Z^2 m_e}{A m_p}\right)^2\frac{\kappa_T}{A}\left|\sum_{\alpha=-1}^{1}\frac{1}{1-\alpha u_i^{1/2}}\, e_\alpha^{j\,*} e_\alpha^i\right|^2 . \quad (3.31)$$

Following Ho & Lai (2001), it is a good approximation to assume that the differential scattering cross-section is independent of the initial photon direction. The resulting approximate source function is:

$$S_\nu^j(\mu) \approx \frac{\kappa_j^{\rm ff}(\mu)}{\kappa_j^{tot}(\mu)}\frac{B_\nu}{2} + \sum_i \frac{\kappa_{ji}^{sc}(\mu)}{\kappa_j^{tot}(\mu)}\frac{cu_\nu^i}{4\pi} \quad (3.32)$$

where $u_\nu^j = (2\pi/c)\int_{-1}^{1} d\mu' I_\nu^j(\mu')$ is the specific energy density of mode j. Note that the source function depends on the specific intensity in all directions, and thus depends on the solution to the radiative transfer equation. Therefore, we calculate S_ν^j iteratively, according to the scheme described below.

Solution to Transfer Equation for Photon Modes Including Partial Mode Conversion

We describe above how vacuum polarization effects can be incorporated into the free-free absorption and scattering opacities for the photon modes. However, these opacity effects do not capture the essence of the vacuum resonance phenomena. As discussed in Lai & Ho (2003a), solving the transfer eq. (3.6) using $K_\pm$ [eq. (3.18)]

as the basis for the photon modes amounts to assuming complete mode conversion ($P_{\rm jump} = 0$), while using $K_{1,2}$ [eq. (3.21)] corresponds to assuming no mode conversion ($P_{\rm jump} = 1$). This was the strategy adopted by previous works. To correctly account for the vacuum resonance effect, it is necessary to use the jump probability $P_{\rm jump}$ [eq. (3.4)] to convert the mode intensities across the resonance according to the formulas:

$$I_X \rightarrow P_{\rm jump}\, I_X + (1 - P_{\rm jump}) I_O, \tag{3.33}$$

$$I_O \rightarrow P_{\rm jump}\, I_O + (1 - P_{\rm jump}) I_X. \tag{3.34}$$

Note that since the resonance density depends on photon energy, the standard Feautrier procedure for integrating the radiative transfer equation cannot be used here, as there is no simple way to incorporate eqs. (3.33)-(3.34) into the method of forward and backward substitution employed by Feautrier (see §6-3 of Mihalas, 1978). Instead, we use the standard Runga-Kutta method to integrate the transfer eq. (3.6) in the upward and downward directions starting from the boundary conditions:

$$I^j_\nu(\tau \rightarrow \tau_{\rm max}, +\mu) \rightarrow B_\nu/2, \tag{3.35}$$

$$I^j_\nu(\tau \rightarrow \tau_{\rm min}, -\mu) \rightarrow 0. \tag{3.36}$$

The Runga-Kutta integration is stopped at the resonance, where eqs. (3.33) and (3.34) are used to convert the mode intensities. Then the integration is continued to completion. The limits $\tau_{\rm max}$ and $\tau_{\rm min}$ are chosen to span 5-8 orders of magnitude. This insures that (1) photons begin their evolution at densities greater than the X-mode decoupling depth, and (2) both X-mode and O-mode photons are fully decoupled from the matter at the outermost edge of the atmosphere ($\tau = \tau_{min}$).

We finite-difference eq. (3.6) as:

$$\pm\mu\frac{I'-I}{\Delta\tau} \approx \frac{1}{2\kappa_T}\left[\kappa(I-S)+\kappa'(I'-S')\right] \tag{3.37}$$

where $I = I_\nu^j(\tau,\pm\mu)$, $I' = I_\nu^j(\tau',\pm\mu)$, $\kappa = \kappa_j^{\rm tot}$, $\kappa' = \kappa_j^{\rm tot}(\tau')$, $S = S_\nu^j(\tau,\pm\mu)$, $S' = S_\nu^j(\tau',\pm\mu)$, with $\tau' = \tau + \Delta\tau$. This gives

$$I' = \frac{1}{1\mp\frac{\Delta\tau\kappa'}{2\mu\kappa_T}}\left[\left(1\pm\frac{\Delta\tau\kappa}{2\mu\kappa_T}\right)I \mp \frac{\Delta\tau}{2\mu\kappa_T}(\kappa S+\kappa' S')\right]. \tag{3.38}$$

This formula yields stable integrations whose results are not strongly dependent on grid spacing (see §3.2.4).

To summarize, our method for integrating the radiative transfer with partial mode conversion is as follows: (1) For given E and θ_{kB}, we integrate eq. (3.6) using (3.38) from $\tau_{\rm max}$ to the vacuum resonance at optical depth τ_V (defined by $\rho(\tau_V) = \rho_V$); (2) At the resonance, the X-mode and O-mode intensities are converted using eqs. (3.33) and (3.34); (3) Integration of eq. (3.6) is continued to $\tau_{\rm min}$. We use an analagous procedure for downward integration from $\tau_{\rm min}$ to $\tau_{\rm max}$.

Temperature Correction Procedure

To integrate the radiative transfer equation, an initial temperature profile is assumed (the initial source function is set to $B_\nu/2$). This initial profile is taken from a previously constructed model with the same magnetic field and effective temperature, but without partial mode conversion (see Ho & Lai, 2003). In general, the solution to eq. (3.6) using this profile will not satisfy eqs. (3.8)-(3.9). To establish equilibrium, the initial temperature profile is corrected using the standard Unsöld-Lucy procedure (Mihalas, 1978). The entire process is iterated until the deviations from radiative equilibrium, constant flux, and the relative size of the temperature correction are all less than a few percent. During a given iteration,

the specific intensity calculated from the previous iteration is used to determine the source function. Thus, the source function must also converge to yield a self-consistent solution. Numerically, we find that the source function converges more rapidly than the other quantities considered above. For a more detailed discussion of the construction of self-consistent atmosphere models, see Ho & Lai (2001) and Mihalas (1978).

3.2.2 Partial Mode Conversion Using Photon Stokes Parameters

While the treatment described above captures the essential physics of the transfer problem, it is important to compare it with the exact solution obtained from integration of the transfer equations for the radiation Stokes parameters. As discussed in §3.1, near the vacuum resonance, the modal transfer equation (3.6) breaks down because of the violation of the Faraday depolarization condition and collapse of the photon modes (see Figs. 4-5 of Lai & Ho 2003a for the precise condition).

The radiative transfer equations for the Stokes parameters are given by (Lai & Ho, 2003a):

$$\pm\mu\frac{\partial \boldsymbol{I}}{\partial\tau} = \boldsymbol{M}\cdot\boldsymbol{I} - \boldsymbol{S_{em}}, \tag{3.39}$$

with

$$\boldsymbol{M} = \frac{\omega}{c\rho\kappa_T}\begin{pmatrix} \sigma_{11i} & 0 & \sigma_{12i}/2 & -\sigma_{12r}/2 \\ 0 & \sigma_{22i} & -\sigma_{12i}/2 & -\sigma_{12r}/2 \\ -\sigma_{12i} & \sigma_{12i} & (\sigma_{11i}+\sigma_{22i})/2 & (\sigma_{11r}-\sigma_{22r)/2} \\ -\sigma_{12r} & -\sigma_{12r} & (\sigma_{22r}-\sigma_{11r})/2 & (\sigma_{11i}+\sigma_{22i})/2 \end{pmatrix}, \quad (3.40)$$

$$\boldsymbol{S_{em}} = \frac{\omega B_\nu}{2\rho\kappa_T c}\begin{pmatrix} \sigma_{11i} \\ \sigma_{22i} \\ 0 \\ -2\sigma_{12r} \end{pmatrix}_{em}, \quad (3.41)$$

where $\sigma_{11} = \epsilon' \cos^2\theta_{kB} + \eta' \sin^2\theta_{kB} - a$, $\sigma_{12} = ig\cos\theta_{kB}$, $\sigma_{22} = \epsilon' - a - m\sin^2\theta_{kB}$, $\sigma_{\alpha\beta r} = \Re e(\sigma_{\alpha\beta})$, $\sigma_{\alpha\beta i} = \Im m(\sigma_{\alpha\beta})$, and $\boldsymbol{I} \equiv (I_{11}, I_{22}, U_\nu, V_\nu)^+$, with $I_{11} = (I_\nu + Q_\nu)/2$, $I_{22} = (I_\nu - Q_\nu)/2$. Note that eq. (3.39) ignores scattering; the "em" suffix on the source functions implies that terms proportional to γ_{re} or γ_{ri} should be set to zero as they are related to scattering contributions. The scattering contributions to eq. (3.39) are derived in Lai & Ho (2003a).

Away from the resonance, the modes discussed in §3.2.1 are well defined and are readily calculated from the Stokes parameters. Neglecting dissipative terms in the dielectric tensor, the transverse part of the mode polarization vectors can be written [see eq. (3.17)]

$$\boldsymbol{e}_+ = (i\cos\theta_m, \sin\theta_m), \quad \boldsymbol{e}_- = (-i\sin\theta_m, \cos\theta_m), \quad (3.42)$$

where θ_m is the "mixing angle" defined by $\cos\theta_m = K_+/\sqrt{1+K_+^2}$, $\sin\theta_m = 1/\sqrt{1+K_+^2}$. The intensities of the $\pm$ modes can be calculated from the Stokes parameters via

$$I_\nu^\pm = \frac{1}{2}\left[I_\nu \pm (\cos 2\theta_m Q_\nu + \sin 2\theta_m V_\nu)\right]. \quad (3.43)$$

Conversely, given the mode intensities, the Stokes parameters can be calculated using

$$I_\nu = I_\nu^+ + I_\nu^-, \tag{3.44}$$

$$Q_\nu = \cos 2\theta_m (I_\nu^+ - I_\nu^-) - 2 \sin 2\theta_m (I_\nu^+ I_\nu^-)^{1/2} \cos \Delta\phi, \tag{3.45}$$

$$U_\nu = -2 (I_\nu^+ I_\nu^-)^{1/2} \sin \Delta\phi, \tag{3.46}$$

$$V_\nu = \sin 2\theta_m (I_\nu^+ - I_\nu^-) + 2 \cos 2\theta_m (I_\nu^+ I_\nu^-)^{1/2} \cos \Delta\phi, \tag{3.47}$$

where $\Delta\phi = \Delta\phi_i + (\omega/c) \int^z (n_+ - n_-) dz$ is the phase difference between the $+$ and $-$ modes. Note that $\Delta\phi$ is unknown, since the initial phase difference $\Delta\phi_i$ between photons in the X and O-modes is random. To correctly evaluate the Stokes parameters from the specific mode intensities, one should sample $\Delta\phi$ from a random distribution, and average over the results. Practically, we note that while the choice of $\Delta\phi$ affects the values of the Stokes parameters, it does not change the specific mode intensities calculated from eq. (3.43). Therefore, the phase difference is unimportant for the comparison of the mode and Stokes parameter transfer equations (see §3.2.3).

In principle, eq. (3.39) can be integrated from $\tau_{\max}$ to $\tau_{\min}$ using the initial condition $\boldsymbol{I}(\tau_{\max}) \to (B_\nu/2, B_\nu/2, 0, 0)^+$ as in §3.2.1. However, this approach runs into a numerical difficulty: away from the vacuum resonance, differences in the indices of refraction for the two modes manifest as rapid oscillations in Q_ν, U_ν, V_ν, which are difficult to handle numerically. Thus, the direct solution of eq. (3.39) over the entire range of integration is impractical. It is possible, however, to integrate eq. (3.39) for a small range of τ around the resonance. Using eqs. (3.43) and (3.44)–(3.47), we can quantitatively compare the result of such an integration with that obtained using the method of §3.2.1, and thereby confirm the accuracy of the

latter method.

3.2.3 Numerical Comparison Between Mode and Stokes Equations

We consider a typical case, the propagation of a photon, initially polarized in the − mode, with energy $E = 1.0$ keV, propagation angle $\theta_{kB} = \pi/4$, and magnetic field $B = 10^{14}$ G. The temperature profile is held constant at $T = 5 \times 10^6$ K [eqs. (3.44)-(3.47) are used to set the initial conditions for (3.39)]. Figure 3.3 shows the Stokes parameters as a function of optical depth near the resonance. These are obtained by integrating eq. (3.39). The corresponding mode intensities are then calculated using eq. (3.43) and depicted in the top panel (solid and dashed lines). The dashed-dot and dotted lines show the results obtained from the integration of the mode equations with partial mode conversion [eqs. (3.33)-(3.34)]. Note that the curves agree exactly except near the resonance where the modes are not well-defined.

We have carried out many similar comparisons between the mode equations and the Stokes transfer equation. The close agreement between the two methods establishes the validity of our method described in §3.2.1, i.e., integrating the mode eq. (3.6) and taking partial mode conversion into account using eqs. (3.33)-(3.34).

3.2.4 Numerical Test of Grid Accuracy

In solving eq. (3.6), we set up grids in Thomson optical depth, temperature, density, energy, and angle. The grid in optical depth $\{\tau_d : d = 1, \ldots, D\}$ is equally spaced logarithmically with $15 - 20$ points per decade (ppd). As discussed above, this grid spans $5 - 8$ orders of magnitude to insure that photons are generated at densities higher than the X-mode decoupling depth, and that they are fully decoupled from

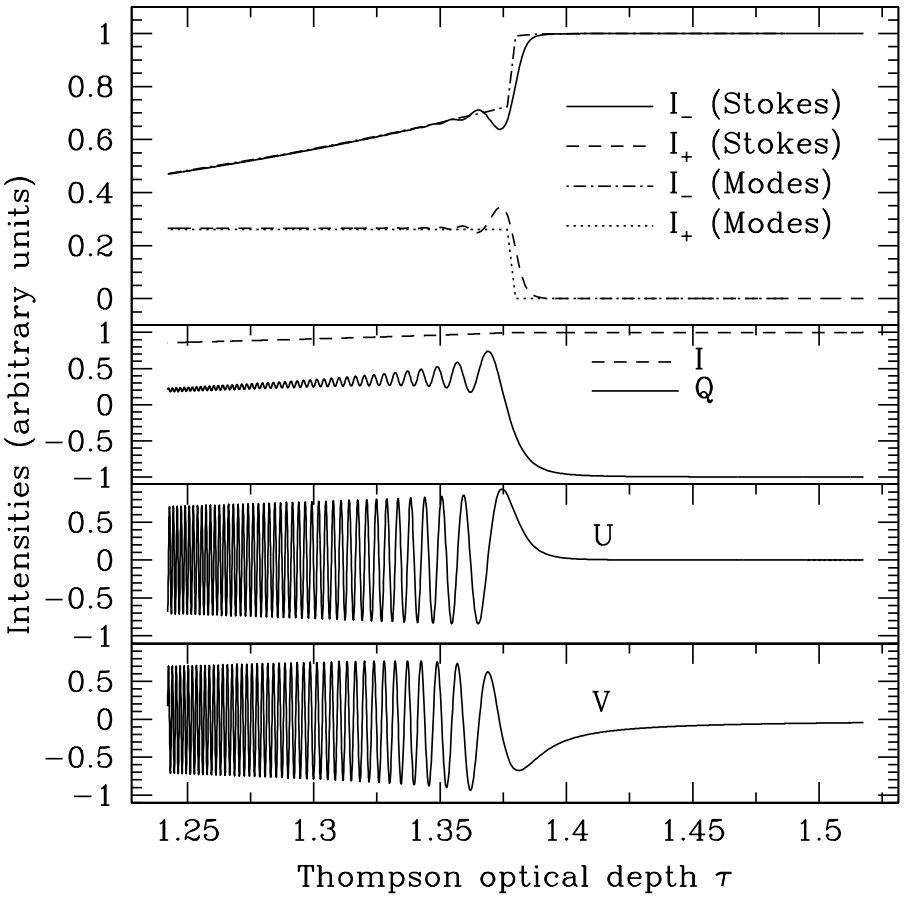

Figure 3.3: Evolution of the Stokes parameters across the vacuum resonance obtained by integrating the transfer equation (3.39). The parameters are $B = 10^{14}$ G, $\theta_{kB} = \pi/4$, $T = 5 \times 10^6$ K, and $E = 1$ keV. At high optical depth, the photon is in the $-$ mode. In the top panel, the dotted line and the dot-dashed line show the mode intensities obtained using the method described in §3.2.1 [i.e., solving the transfer equation (3.6) based on photon modes, but taking account of partial mode conversion through eqs. (3.33)-(3.34)], while the solid and dashed lines give the mode intensities based on the evolution of the Stokes parameters (panels 2-4). Note the close agreement everywhere except near the resonance where the modes are not well-defined.

the matter at the outermost layer.

Care must be used in defining the energy grid. As mentioned before, vacuum polarization introduces a narrow spike in the X mode opacity. A prohibitively high energy grid resolution is required to properly resolve this feature. An alternative is to use the equal-grid method described by Ho & Lai (2003). In this case, each point of the energy grid is chosen to be the vacuum resonance energy [given by eq. (3.1)] corresponding to a point on the optical depth grid: $\{E_n = E_V(\tau_n) : n = 1, \ldots, D\}$. This insures that the vacuum resonance is resolved. Ho & Lai (2003) point out that in the "no conversion" limit, this leads to an over-estimate of the integrated optical depth across the vacuum resonance. It is therefore important to investigate what effect this has on the emergent spectra.

Figure 3.4 illustrates the effect of grid resolution on the spectra for two of the models presented in §3.3. The top panel shows the model with $B = 10^{14}$ G, $T_{\rm eff} = 10^6$ K, which includes vacuum polarization in the opacities, but neglects the mode conversion effect (i.e., $P_{\rm jump} = 1$). Over-estimation of the vacuum resonance in the X-mode opacity is expected to be strongest for this model, since modification of the emission spectrum is due solely to the enhaced opacity. The difference between models at 15 ppd and 20 ppd is negligible. Even at 10 ppd the difference is small, occuring mainly around the proton cyclotron line, as expected.

The bottom panel of Fig. 3.4 shows the model with $B = 10^{14}$ G, and $T_{\rm eff} = 5\times10^6$ K, which includes partial mode conversion. At higher effective temperatures, the optical depth across the vacuum resonance becomes much greater than unity, thus, the error due to finite grid size becomes even less important. The lower grid resolution (10 ppd) model shows negligible deviation from the higher grid resolution (20 ppd) model, even around the proton cyclotron feature. This behavior is typical

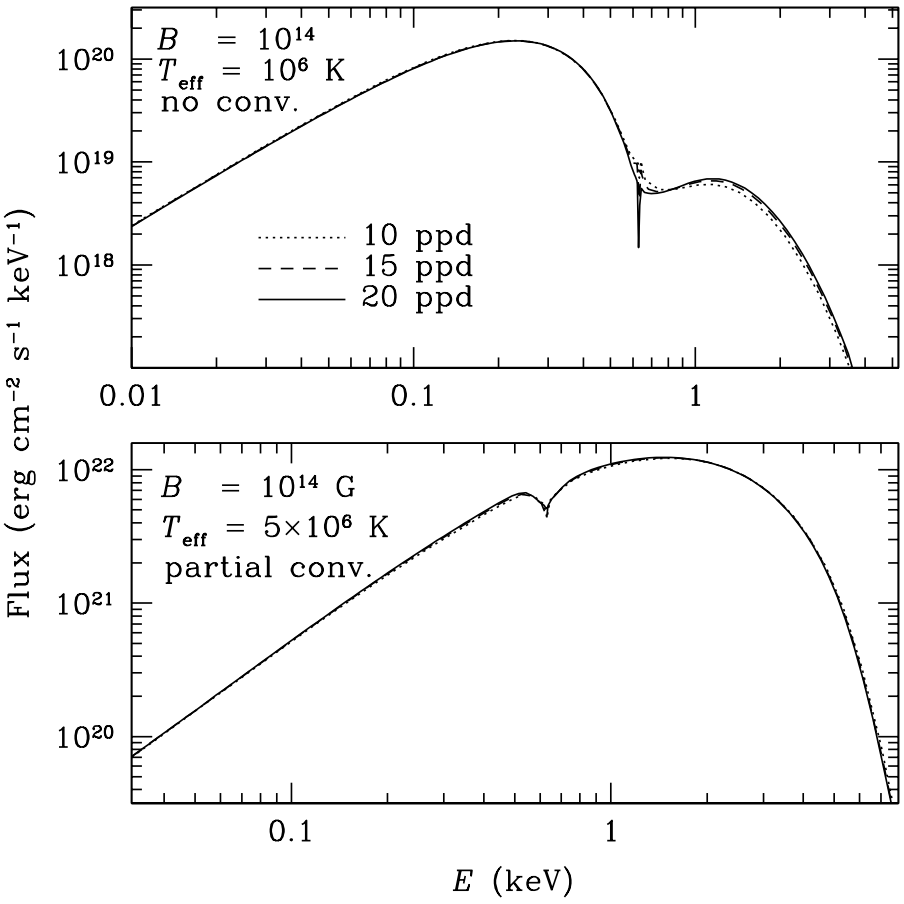

Figure 3.4: Spectra showing the effect of grid resolution on thermal emission. The top panel shows H atmosphere models with $B = 10^{14}$ G, $T_{\rm eff} = 10^6$ K, which include vacuum polarization but neglect mode conversion. As the number of grid points per decade (ppd) are increased, the curves quickly converge to the 20 ppd case. At low resolution the error mainly occurs around the proton cyclotron feature, and is negligible elsewhere. The bottom panel shows H models with $B = 10^{14}$ G, $T_{\rm eff} = 5 \times 10^6$ K, which include vacuum polarization and mode conversion. At the higher effective temperature, the difference between models with varying grid resolution is negligible.

of all models with $B = 5 \times 10^{14}$ G.

3.3 Results

We now present the results of our atmosphere models. We consider $B = 4 \times 10^{13}, 7 \times 10^{13}, 10^{14}, 5 \times 10^{14}$ G, and $T_{\rm eff} = 10^6, 5 \times 10^6$ K, for both H and He compositions.

3.3.1 Atmosphere Structure

Figure 3.5 shows the temperature profile as a function of Thompson optical depth τ for the H atmosphere model with $B = 10^{14}$ G, and $T_{\rm eff} = 10^6$ K. To understand the effect of vacuum polarization, we show the results based on four different treatments: (1) vacuum polarization is completely turned off ("no vaccum"); (2) vacuum polarization is included, but the mode conversion is neglected ($P_{\rm jump} = 1$, "no conversion"); (3) vacuum polarization is included, and complete mode conversion is assumed ($P_{\rm jump} = 0$, "complete conversion"); (4) vacuum polarization is included with the correct treatment of the resonance ("partial conversion"), using $P_{\rm jump}$ calculated from eq. (3.4). We see that models which include vacuum polarization show higher temperatures over a wide range of τ for the same $T_{\rm eff}$ than models which ignore vacuum effects. This temperature increase is due to the X-mode opacity feature at the vacuum resonance (see Fig. 3.1). In general, atmosphere structure is determined by the radiative equilibrium condition; inspection of the individual terms of eq. (3.8) reveals how the resonance affects the temperature profile. The mode absorption opacities obey the relation $\kappa_O \gg \kappa_X$ except at the energies $E = E_{Bi}, E_V$. Thus, $\kappa_X(B_\nu/2)$ can be neglected relative to $\kappa_O(B_\nu/2)$ in eq. (3.8). In the absence of vacuum polarization, the O-mode largely determines

the atmosphere structure due to the weak interaction of X mode photons with the medium. However, when the resonance spike in the X mode opacity is present, $\kappa_X J_\nu^X$ cannot be neglected relative to $\kappa_O J_\nu^O$; in fact, this occurs over a large bandwidth for which $J_\nu^X \gg J_\nu^O$. The result of this enhanced interaction is to increase the overall temperature. Adding the effect of mode conversion further increases the temperature over a large range of optical depth. This is due to heat deposited by converted X mode photons, which interact with the large O mode opacity after passing through the vacuum resonance. The temperature profile for the partial mode conversion model (shown by the solid curve of Fig. 3.5) closely follows the result for the no conversion model (shown by the dotted curve) for the small optical depths at which low energy photons decouple. This is because for these photons, $E \lesssim E_{ad}$, is satisfied and mode conversion is ineffective. For larger optical depths, at which higher energy photons decouple, $E \gtrsim E_{ad}$, and mode conversion is more effective, thus the "partial conversion" result lies between the "no conversion" and "complete conversion" limits.

Figure 3.6 shows the temperature profile for the $B = 10^{14}$ G, $T_{\rm eff} = 5 \times 10^6$ K model. This higher temperature model shows the same basic features as the low-$T_{\rm eff}$ model in Fig. 3.5. In this case, the energy flux is carried by photons with higher energies, and the adiabatic condition ($E \gtrsim E_{ad}$) is more readily satisfied, leading to effective mixing of photon modes. Thus we see that at large optical depths ($\tau \gtrsim 0.1$), the partial conversion profile closely follows the complete conversion curve. At lower optical depth, the partial conversion profile lies between the complete conversion and no conversion curves.

Finding self-consistent temperature profiles is the most time consuming step in atmosphere modeling. Once the profile is known, the emergent radiation can

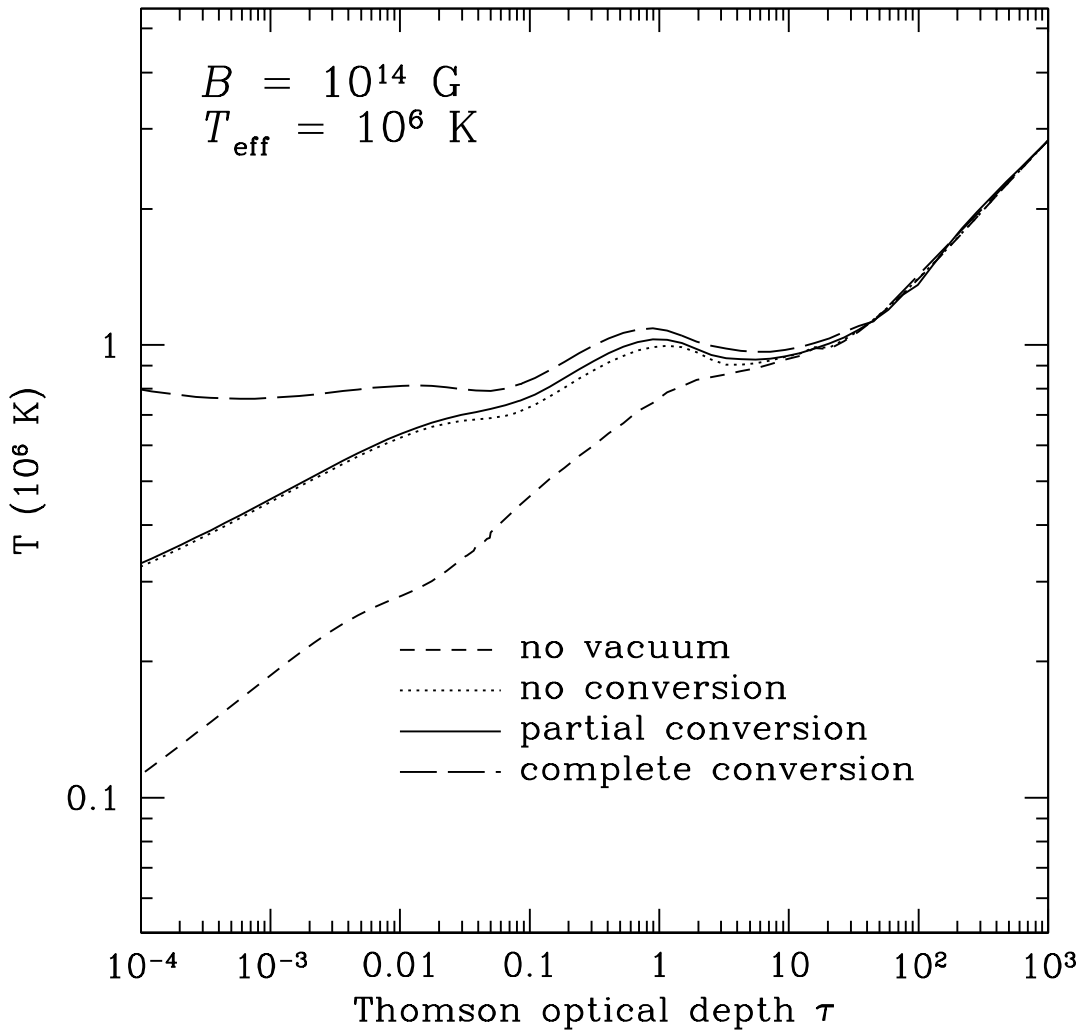

Figure 3.5: Temperature profile for the H atmosphere model with $B = 10^{14}$ G, $T_{\rm eff} = 10^6$ K. The four curves correspond to different ways of treating the vacuum polarization effect: (1) no vacuum (short-dashed curve); (2) no conversion (dotted curve); (3) partial conversion (solid curve); and (4) complete conversion (long-dashed curve).

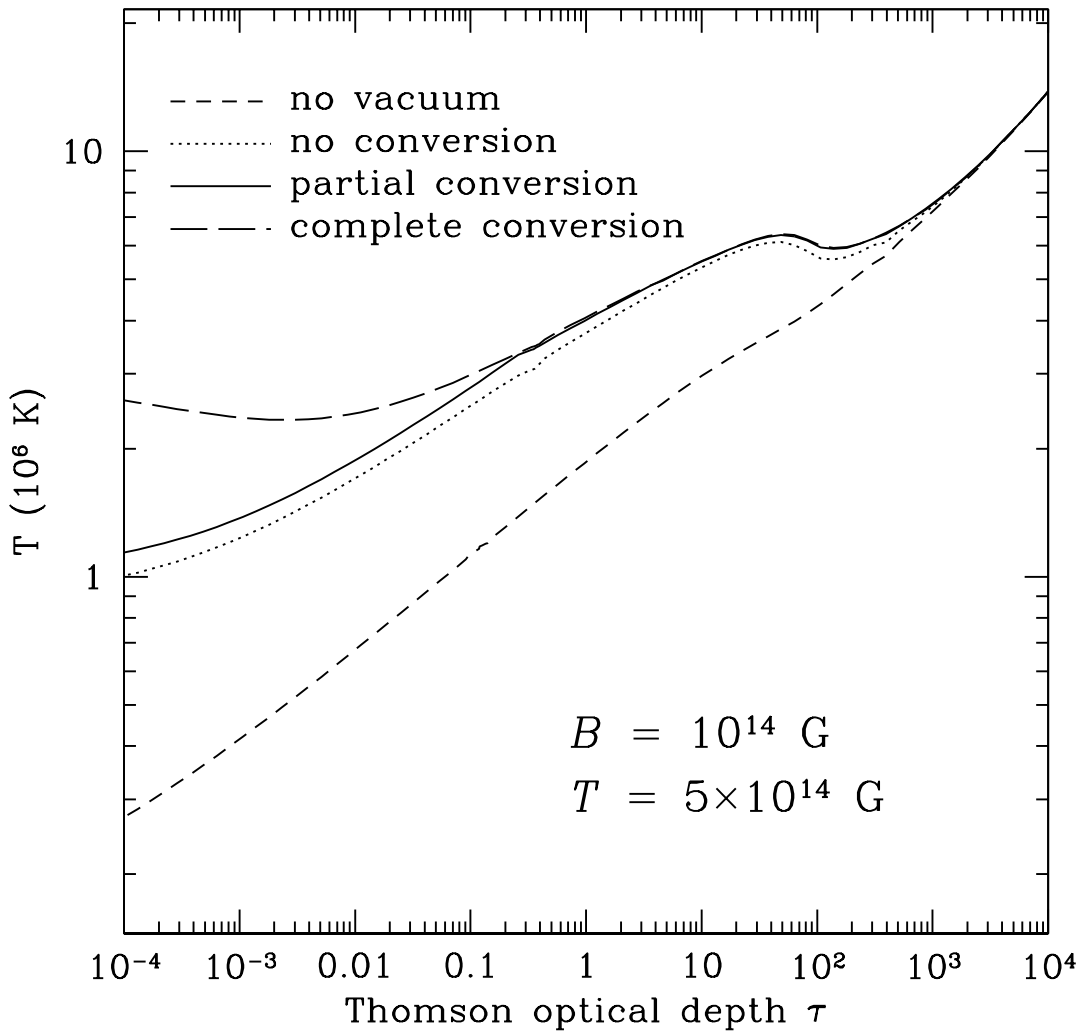

Figure 3.6: Same as Fig. 3.5, except for $T_{\rm eff} = 5 \times 10^6$ K.

be obtained by a single integration of the transfer equation. To facilitate future work on NS atmospheres and related applications, we provide fitting formulas for the models presented in this paper. Formulas are provided only for models incorporating vacuum polarization with partial mode conversion. The fits are valid over the optical depth range $\tau = 10^{-3} - 2 \times 10^4$. Each model is fit by the function

$$\log_{10}\left[T_6(\tau)\right] = \begin{cases} a_1 + a_2\,\Delta x + a_3\,\Delta x^2 + a_4\,\Delta x^3 + a_5\,\Delta x^4 + a_6\,\Delta x^5 \\ \qquad\qquad\qquad\qquad \tau_{\rm mid} < \tau < 2 \times 10^4, \\ b_1 + b_2\,\Delta x + b_3\,\Delta x^2 + b_4\,\Delta x^3 + b_5\,\Delta x^4 + b_6\,\Delta x^5 \\ \qquad\qquad\qquad\qquad 10^{-3} < \tau < \tau_{\rm mid}, \end{cases} \tag{3.48}$$

where $x \equiv \log_{10}(\tau)$, $\Delta x \equiv x - x_{\rm mid}$, and $\tau_{\rm mid}$ denotes the break between the two parts of the fit used to describe the temperature profile. The parameters are fit with a standard linear least-squares method. To insure that the function and its derivative are continuous through $\tau_{\rm mid}$, we set $b_1 = a_1$, $a_2 = b_2$, and re-fit, holding b_1 and a_2 constant. This process is iterated until a self-consistent set of parameters is obtained. The parameters for each model are summarized in Table 3.1.

Table 3.1: Parameters in the temperature profile fitting formulas [eq. (3.48)] for NS atmosphere models with different magnetic field strengths, effective temperatures and compositions (ionized H or He)

Model	$\tau_{\rm mid}$	a_1	a_2	a_3	a_4	a_5	a_6
10^{13} G, 5×10^6 K, H	27.1	0.793	0.122	-0.502	0.548	-0.205	0.0266
4×10^{13} G, 10^6 K, H	4.27	-0.0599	0.192	0.0225	0.0115	-0.0072	0.00116
4×10^{13} G, 5×10^6 K, H	11.9	0.623	-0.0425	0.0991	0.0412	-0.026	0.0036
7×10^{13} G, 10^6 K, H	0.888	-0.0455	-0.158	0.221	-0.0469	0.00231	0.000307
7×10^{13} G, 5×10^6 K, H	21.6	0.789	0.123	-0.650	0.726	-0.274	0.0354
10^{14} G, 10^6 K, H	0.683	0.00828	0.0614	-0.304	0.266	-0.0719	0.00652
10^{14} G, 10^6 K, He	0.749	-0.0935	-0.154	0.262	-0.0904	0.0167	-0.00124
10^{14} G, 5×10^6 K, H	30.6	0.799	0.115	-0.537	0.617	-0.241	0.0326
5×10^{14} G, 10^6 K, H	32.9	0.0939	0.0181	-0.0153	-0.0413	0.0376	-0.00578
5×10^{14} G, 5×10^6 K, H	63.2	0.761	0.00198	0.267	-0.356	0.179	-0.0282
5×10^{14} G, 5×10^6 K, He	23.5	0.707	0.0467	0.342	-0.417	0.174	-0.0234

Table 3.1 (Continued)

Model	$\tau_{\rm mid}$	b_1	b_2	b_3	b_4	b_5	b_6
10^{13} G, 5×10^6 K, H	27.1	0.793	0.122	0.00445	0.0108	0.00211	0.0000574
4×10^{13} G, 10^6 K, H	4.27	-0.0599	0.192	0.109	0.0828	0.0256	0.00286
4×10^{13} G, 5×10^6 K, H	11.9	0.623	-0.0425	-0.0851	-0.00392	0.0034	0.000418
7×10^{13} G, 10^6 K, H	0.888	-0.0455	-0.158	-0.329	-0.118	-0.00387	0.00304
7×10^{13} G, 5×10^6 K, H	21.6	0.789	0.123	-0.0105	-0.00406	-0.00242	-0.000411
10^{14} G, 10^6 K, H	0.683	0.00828	0.0614	-0.313	-0.374	-0.162	-0.0234
10^{14} G, 10^6 K, He	0.749	-0.0935	-0.154	-0.197	0.0197	0.0428	0.0083
10^{14} G, 5×10^6 K, H	30.6	0.799	0.115	-0.00603	0.00409	0.000351	-0.0000978
5×10^{14} G, 10^6 K, H	32.9	0.0939	0.0181	0.0504	0.0462	0.00991	0.000676
5×10^{14} G, 5×10^6 K, H	63.2	0.761	0.00198	-0.118	-0.0336	-0.00428	-0.00022
5×10^{14} G, 5×10^6 K, He	23.5	0.707	0.0467	-0.109	-0.040	-0.0069	-0.000481

3.3.2 Spectra

Figure 3.7 presents the spectrum for the H atmosphere model with $B = 10^{14}$ G and $T_{\rm eff} = 10^6$ K. The results for the four different ways of treating the vacuum resonance (see §3.3.1) are shown. These spectra correspond to the temperature profiles depicted in Fig. 3.5.

When the vacuum polarization effect is neglected, the spectrum of a magnetic, ionized H atmosphere model generally exhibits two characteristics: (1) a hard spectral tail (compared to blackbody) due to the non-grey free-free opacity ($\kappa^{\rm ff}$ decreases with increasing photon energy; Shibanov et al. 1992; Pavlov et al. 1995); (2) a significant proton cyclotron absorption line when E_{Bi} is not too far away from the blackbody peak ($\sim 3k_BT$) (Zane et al., 2001; Ho & Lai, 2001). Vacuum polarization tends to soften the hard spectral tail and suppress (reduce) the proton cyclotron line. These effects are discussed extensively in §4 of Ho & Lai (2003), and Lai & Ho (2003a). In Fig. 3.7, all of the models that include vacuum polarization effects display a large reduction in the equivalent width (EW) of the proton cyclotron feature due to the modification of the temperature profile by the vacuum resonance (see §3.3.1) and the mode conversion effect. The spectra also show softening of the hard spectral tail relative to the no vacuum case, though they are all still harder than blackbody. The "partial conversion" curve appears as an intermediate case between the "complete conversion" and "no conversion" extremes. The adiabatic regime where mode conversion is efficient is clearly visible: for $E \gtrsim E_{ad} \sim 2$ keV, the "partial conversion" curve begins to follow the "complete conversion" curve.

This transition from "no conversion" to "complete conversion" is further illustrated by Fig. 3.8, which shows, for several photon energies E (and a given direction

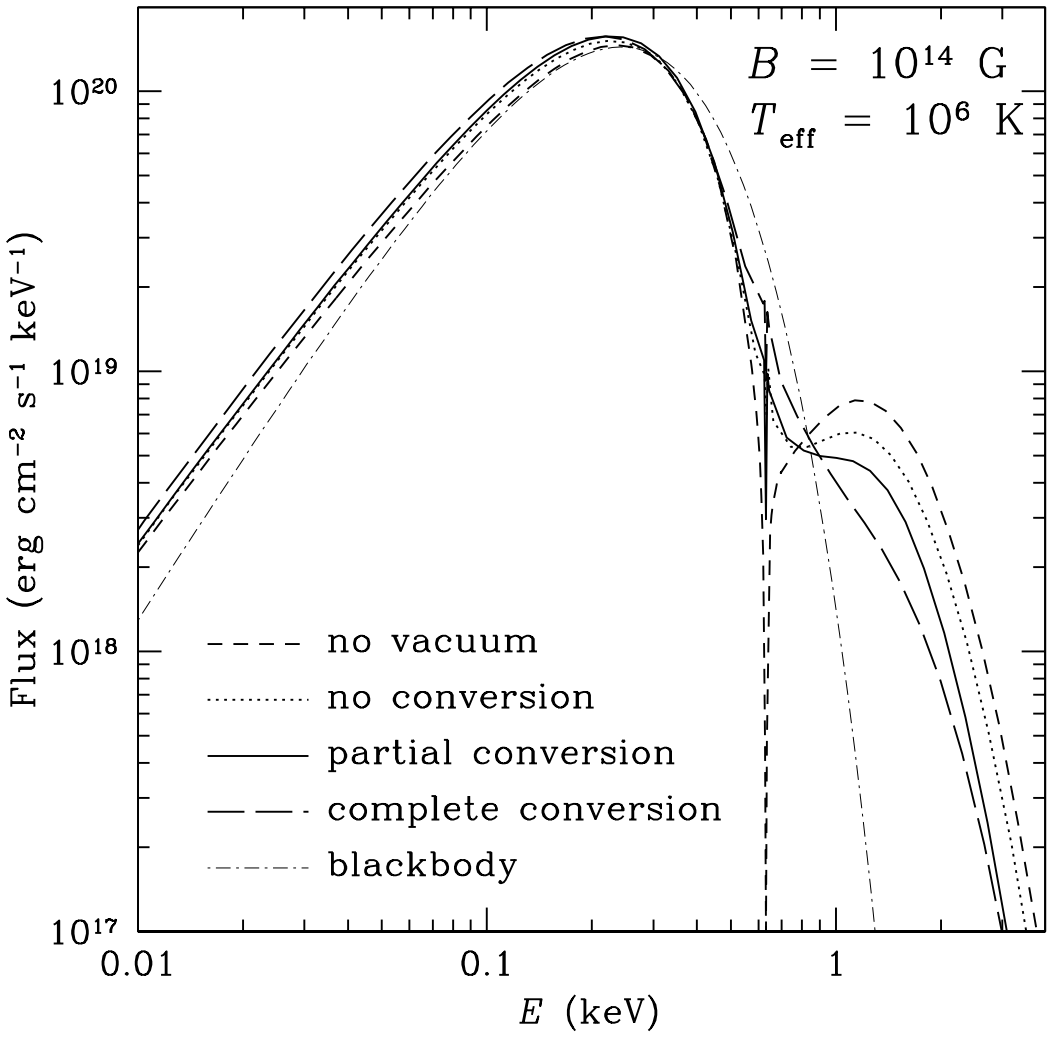

Figure 3.7: Spectra for H atmosphere models with $B = 10^{14}$ G, $T_{\rm eff} = 10^6$ K. The four cases described in the text are shown: (1) no vacuum (short-dashed cuve); (2) no conversion (dotted curve); (3) partial conversion (solid curve); and (4) complete conversion (long-dashed curve). The light dashed-dot curve shows the blackbody spectrum with $T = 10^6$ K. For all three cases that include vacuum effects, the proton cyclotron feature is strongly suppressed and the high energy tail is softened relative to the no vacuum case. The "partial conversion" curve is seen to be intermediate between the "no conversion" and "complete conversion" limits.

of propagation, θ_{kB}) the evolution of the specific mode intensities as a function of optical depth. At the resonance depth (denoted by the vertical lines), the X mode photons encounter the vacuum induced spike in opacity, and mode conversion occurs [governed by the non-adiabatic jump probability $P_{\rm jump}$; see eq. (3.4)]. As the energy is increased (from the second to bottom panels), mode conversion becomes increasingly more effective.

Figure 3.9 shows the spectrum for the H model with $B = 10^{14}$ G and $T_{\rm eff} = 5\times10^6$ K. All the calculations that include vacuum polarization effects show strong suppression of the ion cyclotron feature and significant softening of the hard spectral tail. At higher effective temperatures, there is a smaller difference between the no conversion, partial conversion, and complete conversion cases. In this regime, the optical depth across the vacuum resonance is much greater than unity, and the decoupling of X-mode photons occurs at the resonance density whether or not mode conversion is taken into account (see Lai & Ho, 2002). At high energies ($E \gtrsim 5$ keV), the models which include mode conversion are softer than those which do not.

Figures 3.10-3.13 depict atmosphere models at $T_{\rm eff} = 10^6$ K with varying magnetic field strengths, comparing the "no vacuum" and correct "partial conversion" results. For $B = 4\times10^{13}$ G $< B_l$ (Fig. 3.10), the vacuum resonance lies at a lower density than the X-mode and O-mode photospheres, and vacuum polarization has a negligible effect on the spectrum, reflected by the close agreement between the "no vacuum" and "partial conversion" curves. For the H atmosphere model with $B = 7\times10^{13}$ G (Fig. 3.11), and the He atmosphere model with $B = 10^{14}$ G (Fig. 3.12), vacuum polarization affects the spectrum. For these models, $B \gtrsim B_l$, and the ion cyclotron line lies near the blackbody peak. Thus, it is particularly

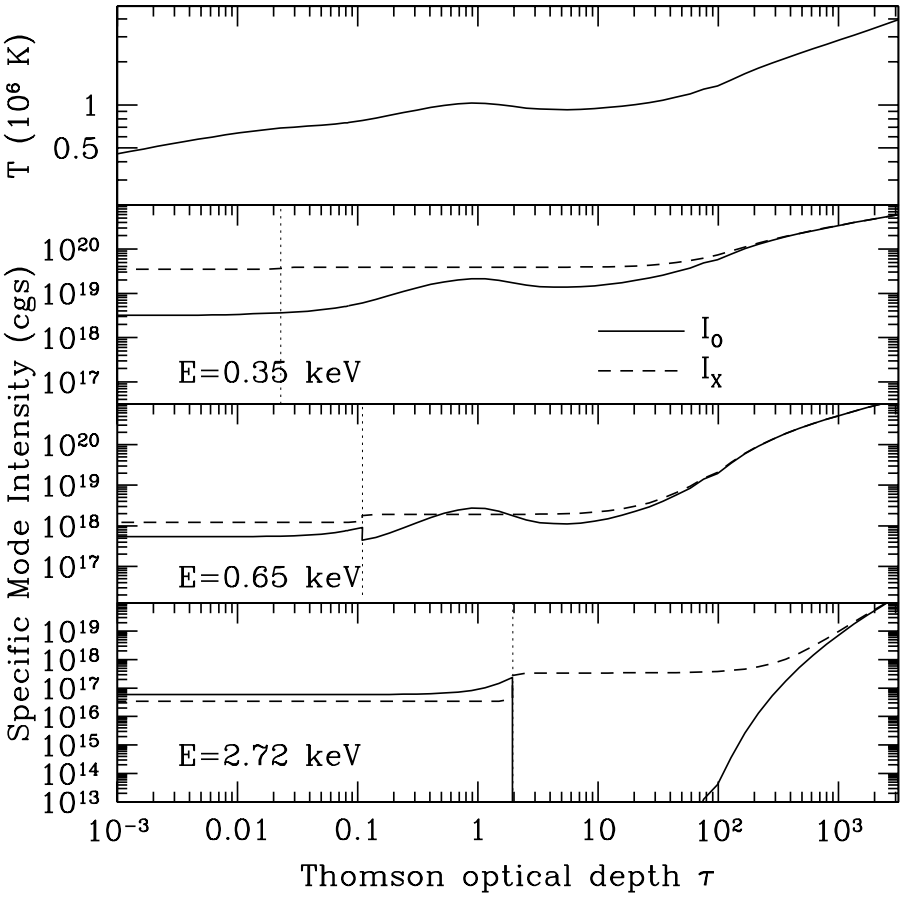

Figure 3.8: The transition from "no conversion" to "complete conversion" for a photon propagating in a H atmosphere with $B = 10^{14}$ G, $T_{\rm eff} = 10^6$ K. The top panel shows the temperature profile for this model. The bottom three panels show the evolution of the specific mode intensities for energies $E = 0.35, 0.65, 2.72$ keV and $\theta_{kB} = \pi/4$. The solid line shows the O-mode intensity, the dashed line the X-mode intensity, and the dotted vertical lines specify the location of the vacuum resonance. For $E = 0.35$ keV: $H_\rho = 0.69$ cm, $E < E_{ad}$, and $P_{\rm jump} = 1.0$, leading to minimal mode conversion. For $E = 0.65$ keV: $H_\rho = 0.78$ cm, $E \sim E_{ad}$, and $P_{\rm jump} = 0.65$, leading to partial mixing of the modes. For $E = 2.72$ keV: $H_\rho = 0.98$ cm, $E > E_{ad}$, and $P_{\rm jump} = 0.15$, leading to nearly complete conversion of the modes.

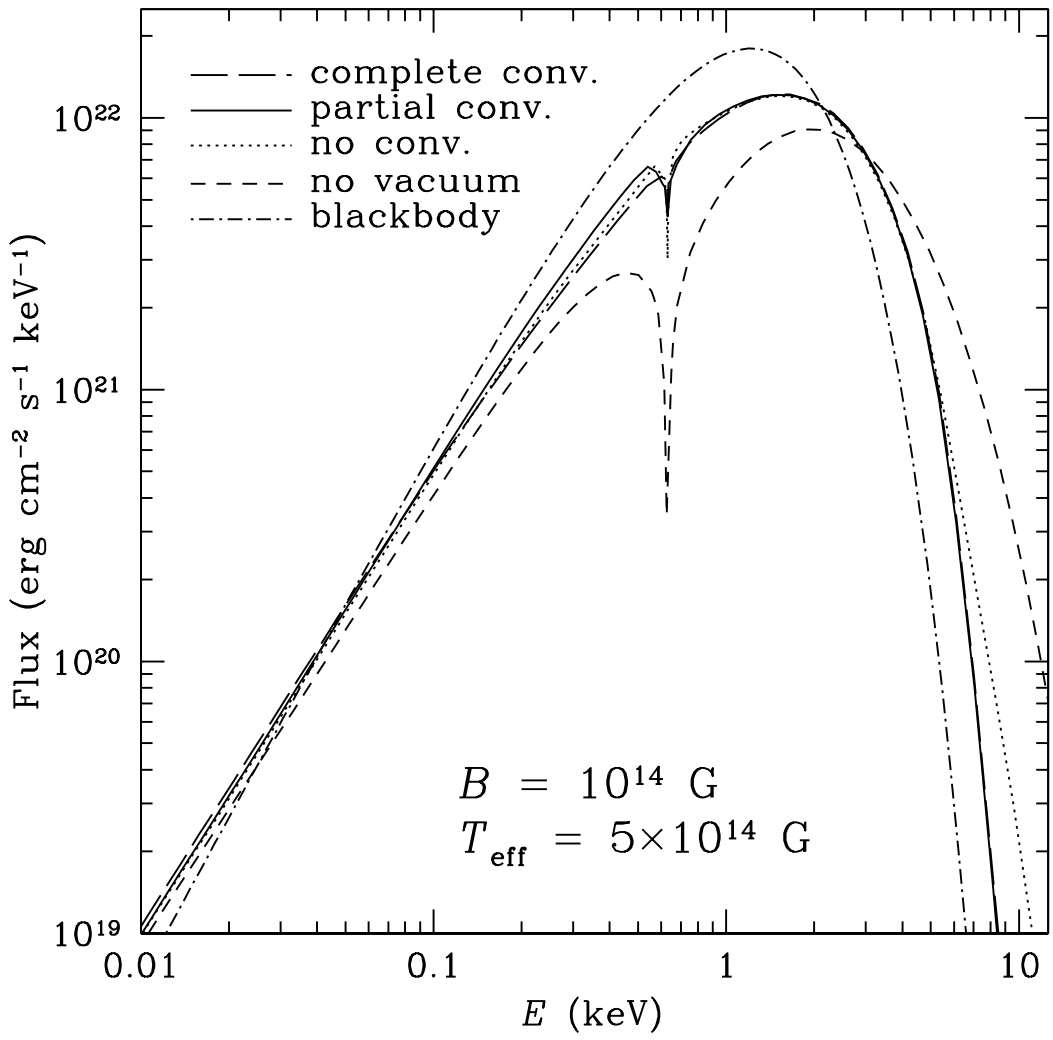

Figure 3.9: Same as Fig. 3.7, except for $T_{\rm eff} = 5\times10^6$ K. The strength of the proton cyclotron feature is strongly suppressed for models which include vacuum polarization. At $E \gtrsim 5$ keV, the models which include mode conversion are softer than those without, though all the atmosphere models are still harder than blackbody.

important to treat the vacuum resonance correctly, taking partial mode conversion into account to calculate the line width. For the $B = 5 \times 10^{14}$ G model (Fig. 3.13), the spectral feature at E_{Bi} is outside the energy band of observational interest. We note that at such a high field and low effective temperature, the atmosphere should contain a significant fraction of bound atoms and molecules (Ho et al., 2003; Potekhin et al., 2004), so the fully ionized model shown in Fig. 3.13 is not realistic.

Figures 3.14-3.15 show atmosphere models at magnetic field strength $B = 5 \times 10^{14}$ G and $T_{\rm eff} = 5 \times 10^6$ K, for H and He compositions. At this effective temperature, the ion cyclotron feature lies close to the blackbody peak, and the effects of vacuum polarization on the line width and spectral tail are pronounced.

3.3.3 Beaming Patterns and Observed Spectra

Calculations of observed NS lightcurves and polarization signals (see Chapter 4) are critical for interpreting observations. An important ingredient of such calculations is the angular beam pattern of surface emission. Figures 3.16-3.23 show the radiation intensities from local patches of NS atmosphere (for the $T_{\rm eff} = 10^6$ K models presented in §3.3.2) as a function of emission angle relative to the surface normal for several photon energies. The heavy curves show models that include vacuum polarization effects, while the light curves show models that neglect vacuum polarization. Magnetized atmosphere models which neglect vacuum polarization have a distinctive beaming pattern, consisting of a thin "pencil" feature at low emission angles and a broad "fan" beam at large emission angles, with a prominent gap between them (c.f., Özel, 2001). This gap tends to increase with increasing photon energy. The detailed shape of the emission beam pattern is determined by the temperature profile and the anisotropy of the mode opacities. As shown

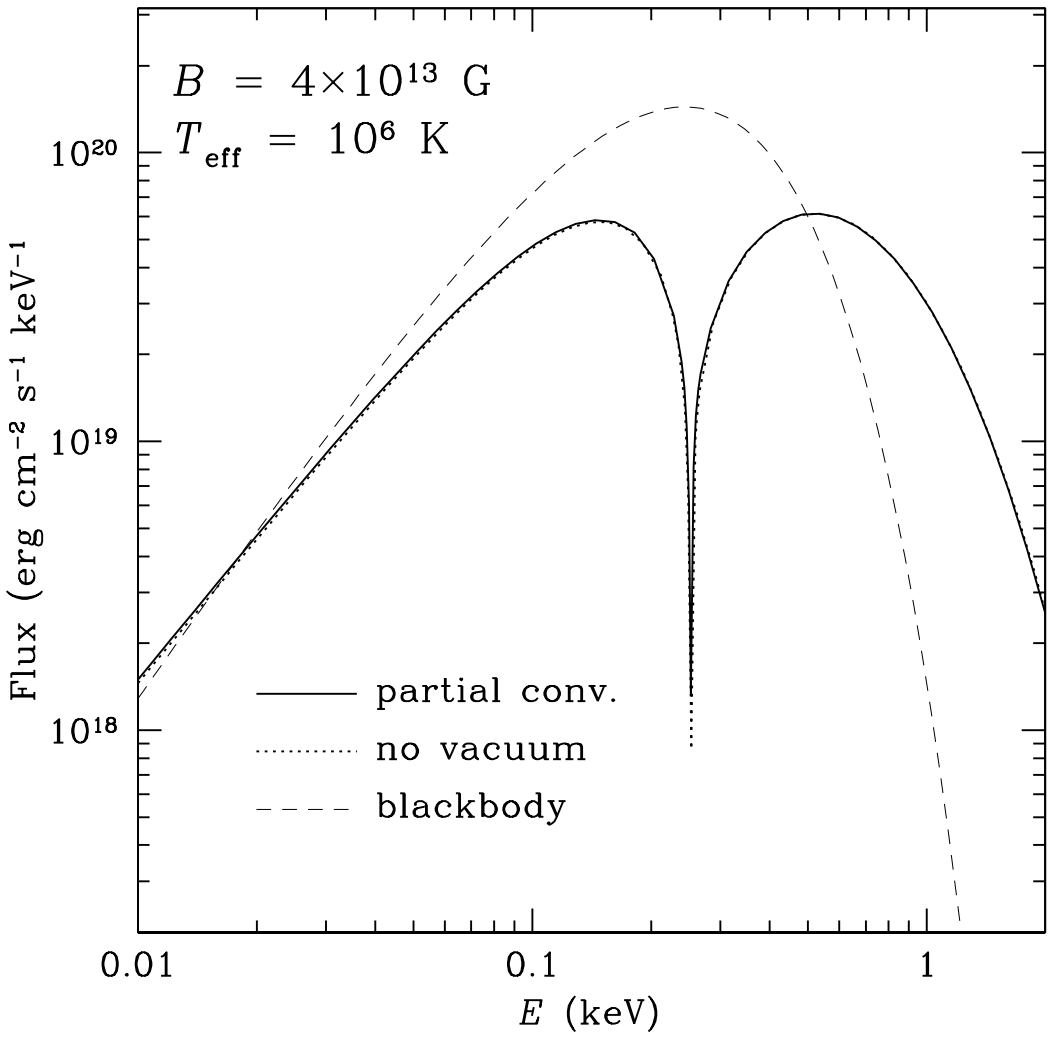

Figure 3.10: Spectrum of the H atmosphere model with $B = 4 \times 10^{13}$ G, $T_{\rm eff} = 10^6$ K, calculated for two cases: partial mode conversion (solid curve), and no vacuum (dotted curve). The light dashed line shows the blackbody spectrum with $T = 10^6$ K.

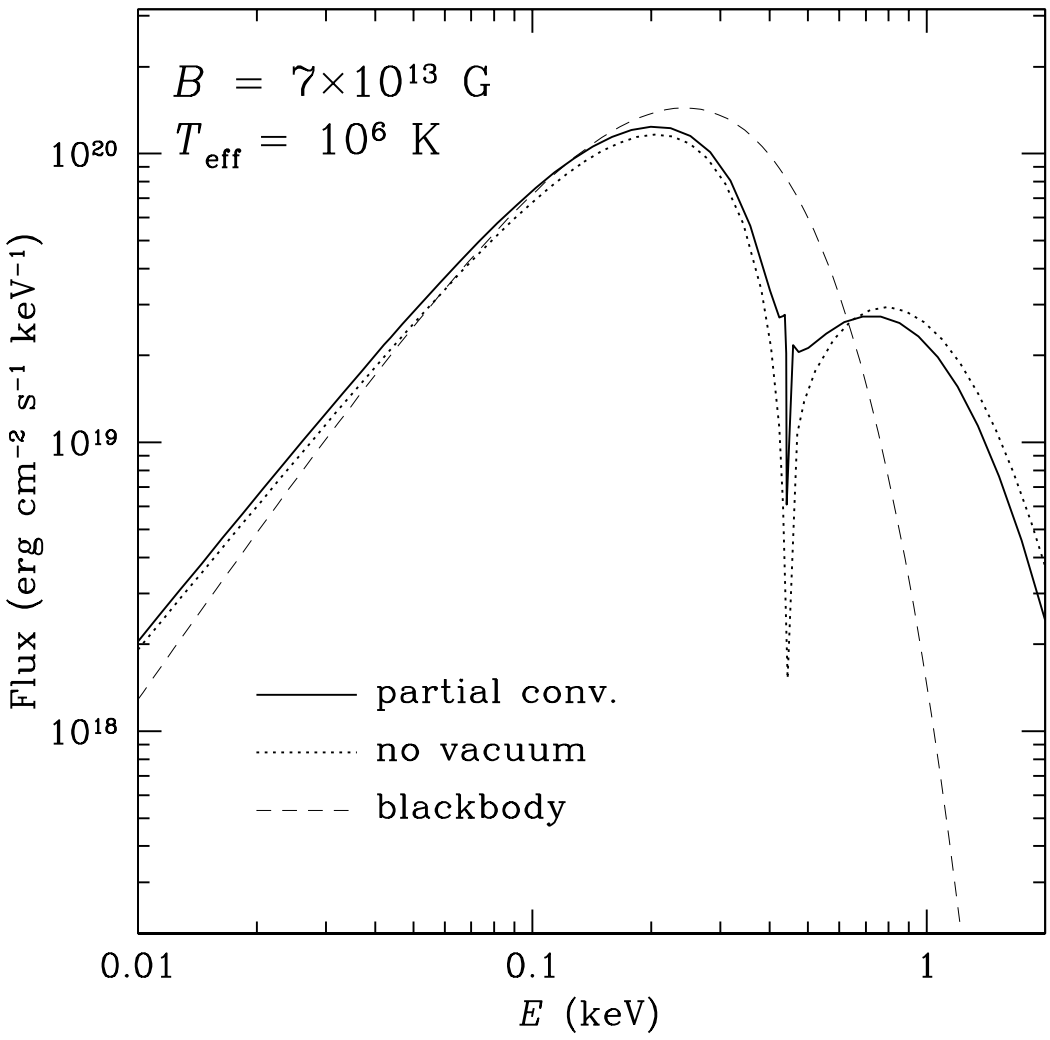

Figure 3.11: Same as Fig. 3.7, except for $B = 7 \times 10^{13}$ G.

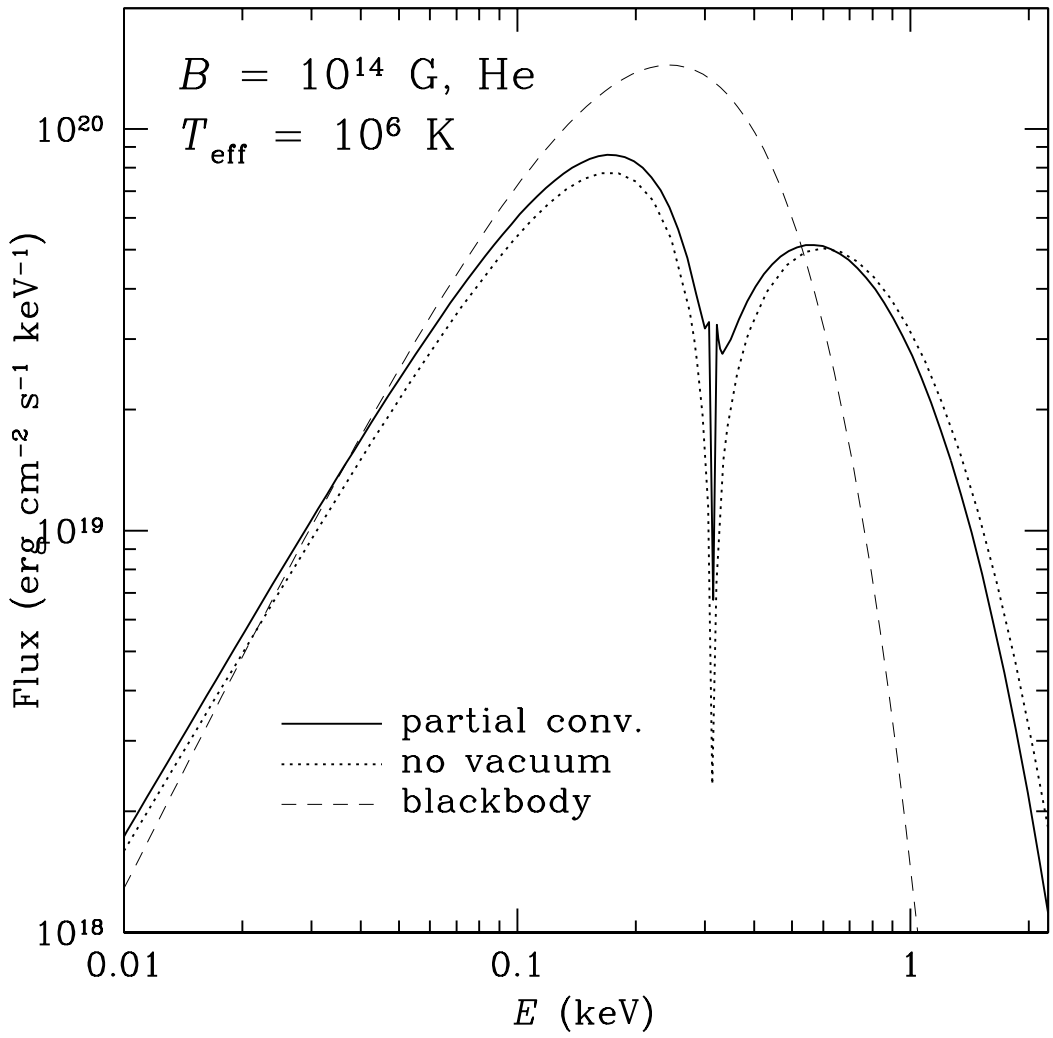

Figure 3.12: Same as Fig. 3.10, except for He composition with $B = 10^{14}$ G. The ion cyclotron line width is reduced by vacuum polarization, though it has a larger equivalent width than the model for H, due to the location of the line near the maximum of the continuum emission.

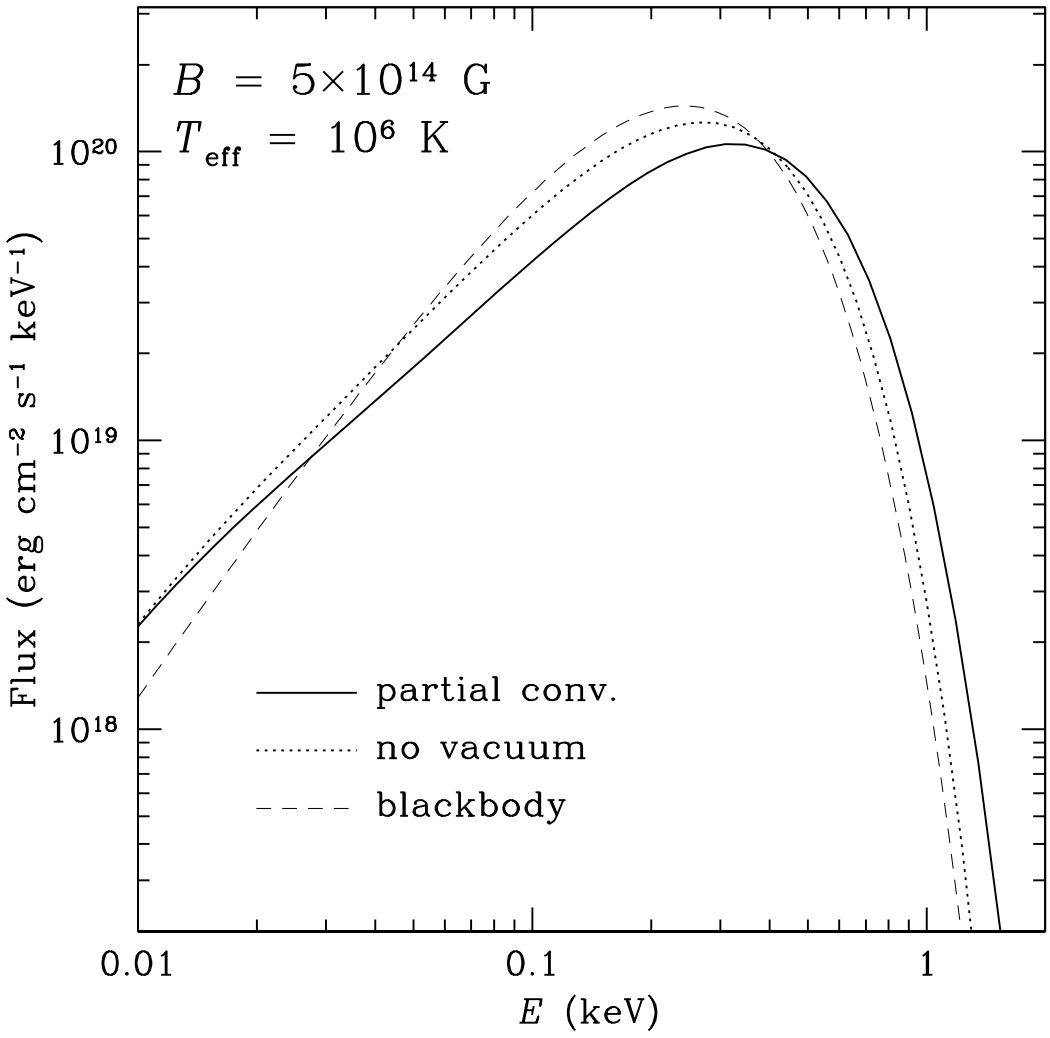

Figure 3.13: Same as Fig. 3.11, except for $B = 5 \times 10^{14}$ G.

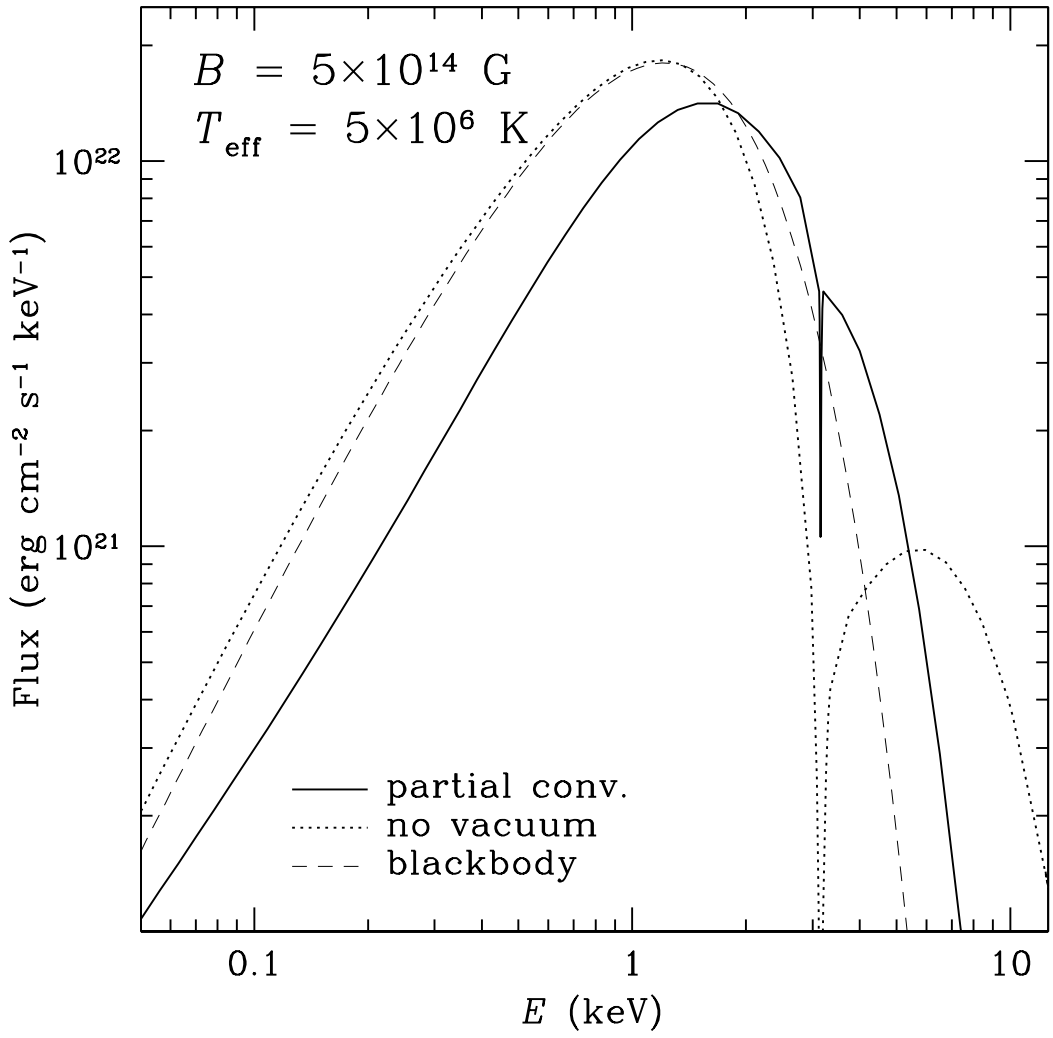

Figure 3.14: Same as Fig. 3.13, except for $T_{\rm eff} = 5 \times 10^6$ K. The proton cyclotron feature is strongly suppressed by vacuum polarization. The hard spectral tail is softened considerably relative to the no vacuum case, though it is still harder than blackbody.

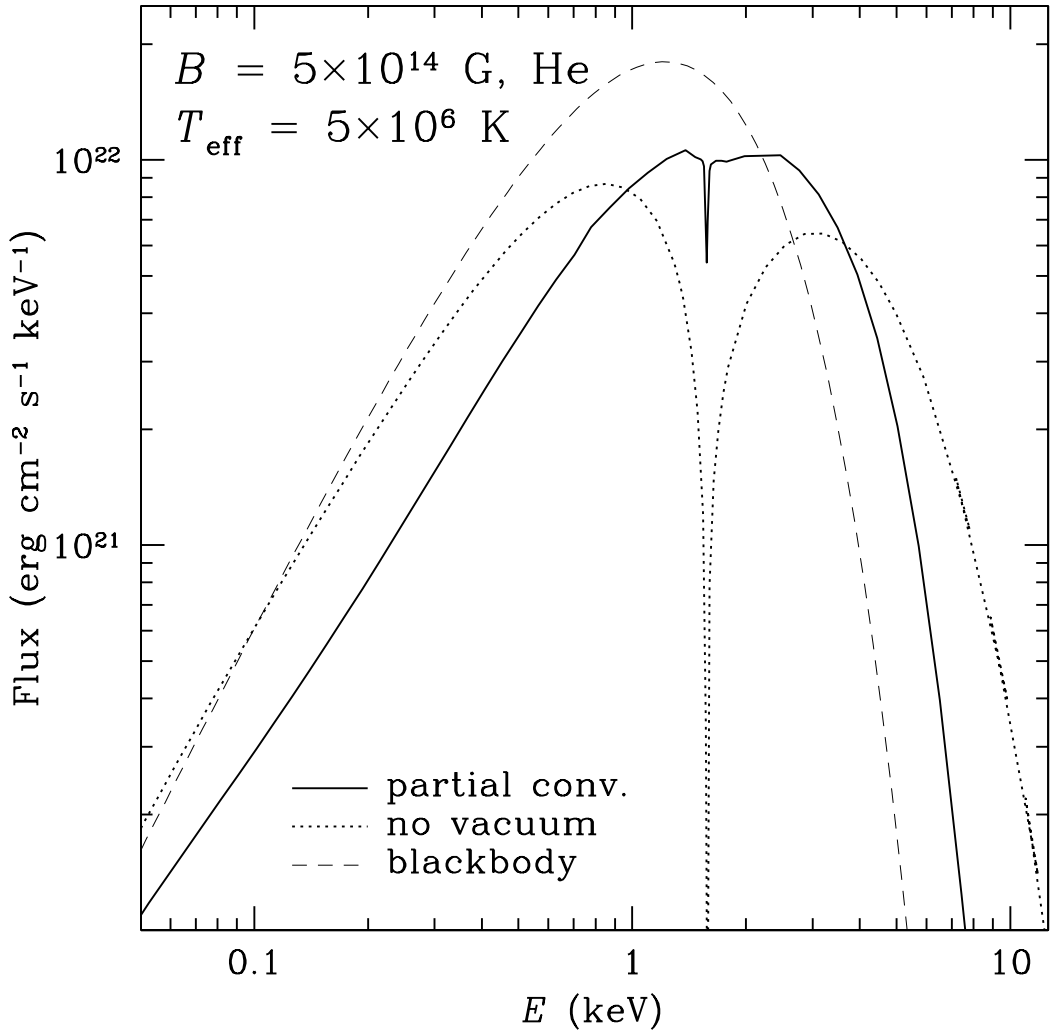

Figure 3.15: Same as Fig. 3.14, except for He composition. Vacuum polarization strongly suppresses the ion cyclotron feature, and softens the hard spectral tail relative to the no vacuum case.

by Figs. 3.16-3.23, vacuum polarization tends to smooth out the gap, leading to a broad, featureless beam pattern at large magnetic fields. The broadening of the beaming pattern is due to the alteration of the temperature profile by the spike in opacity at the vacuum resonance and the mode conversion effect.

Figures 3.24-3.29 show the specific radiation intensity from patches of NS atmosphere (for the $T_{\rm eff} = 10^6$ K models presented in §3.3.2) at several emission angles. We find that the shapes of the specta and EWs of the absorption features can change significantly depending on the emission angle and whether or not vacuum polarization effects are included in the calculation.

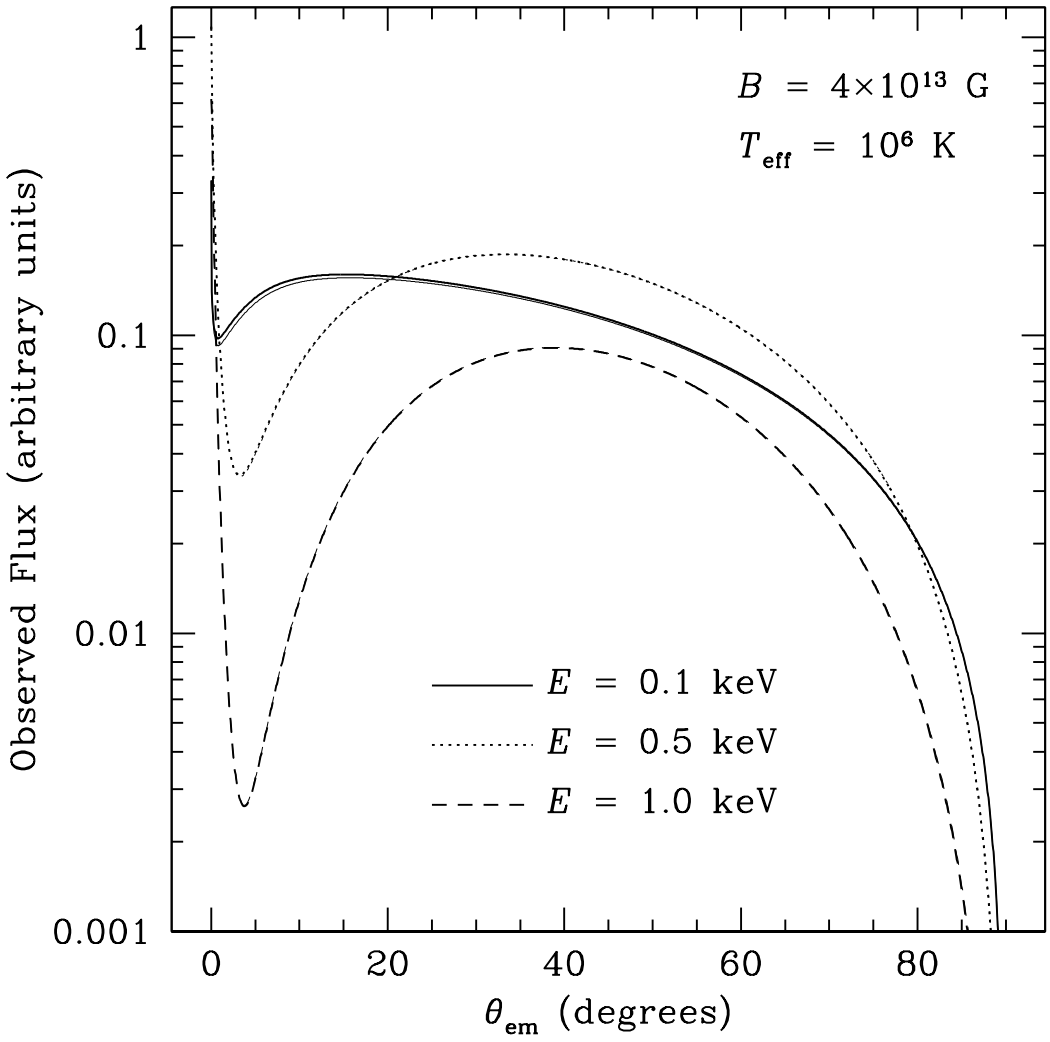

Figure 3.16: Observed flux as a function of emission angle at photon energies $E = 0.1, 0.5, 1$ keV for the NS atmosphere model with $B = 4 \times 10^{13}$ G and $T_{\rm eff} = 10^6$ K. For $B < B_l$, the beam pattern assumes the characteristic shape for magnetized NS atmospheres which neglect vacuum polarization effects, with a thin "pencil" shape at low emission angles, a broad "fan" at large emission angles, and a prominent gap in between. The gap becomes more pronounced with increasing photon energy. The heavy curves show models which include vacuum polarization effects, while the light curves denote models which neglect vacuum polarization.

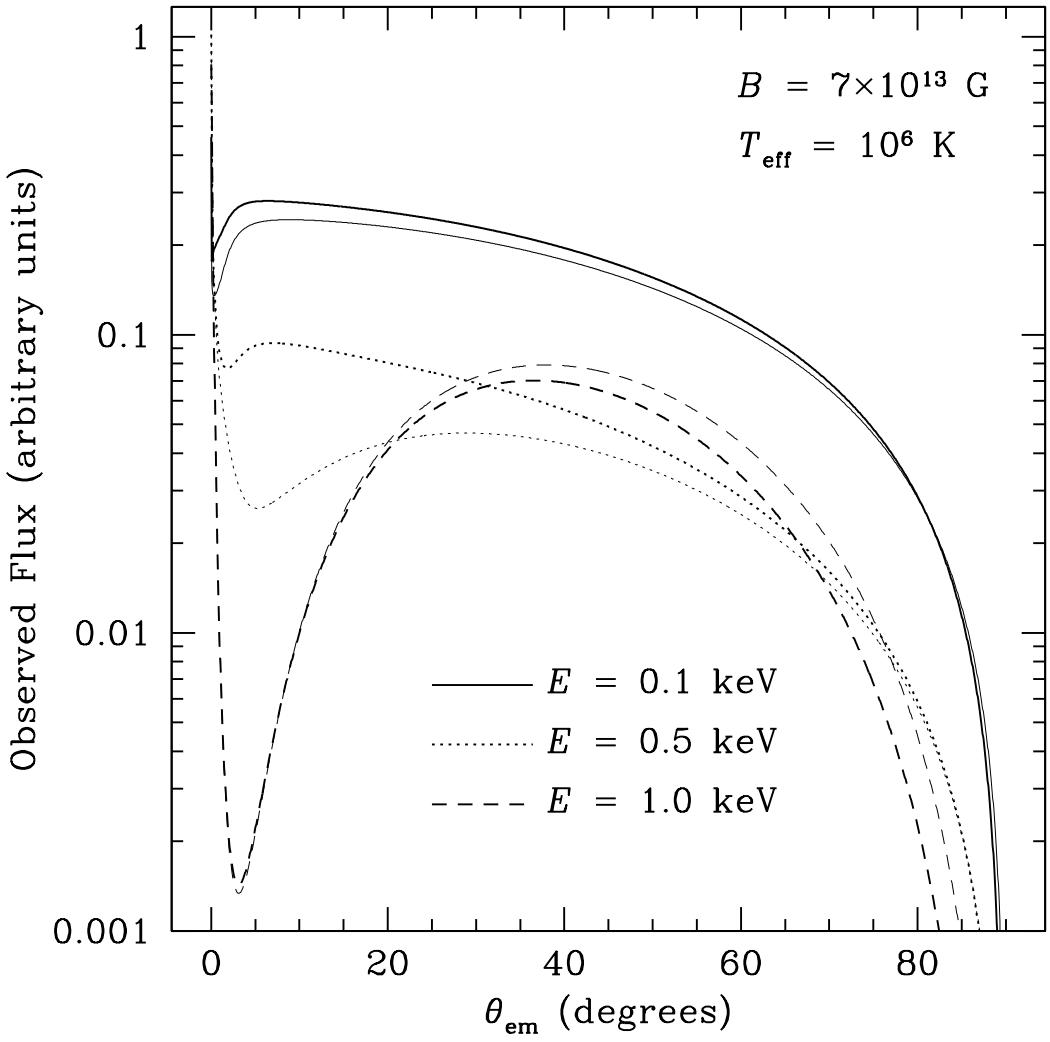

Figure 3.17: Same as Fig. 3.16 except for $B = 7 \times 10^{13}$ G. For $B > B_l$, vacuum polarization effects tend to smooth out the gap in emission, leading to a broader beam pattern.

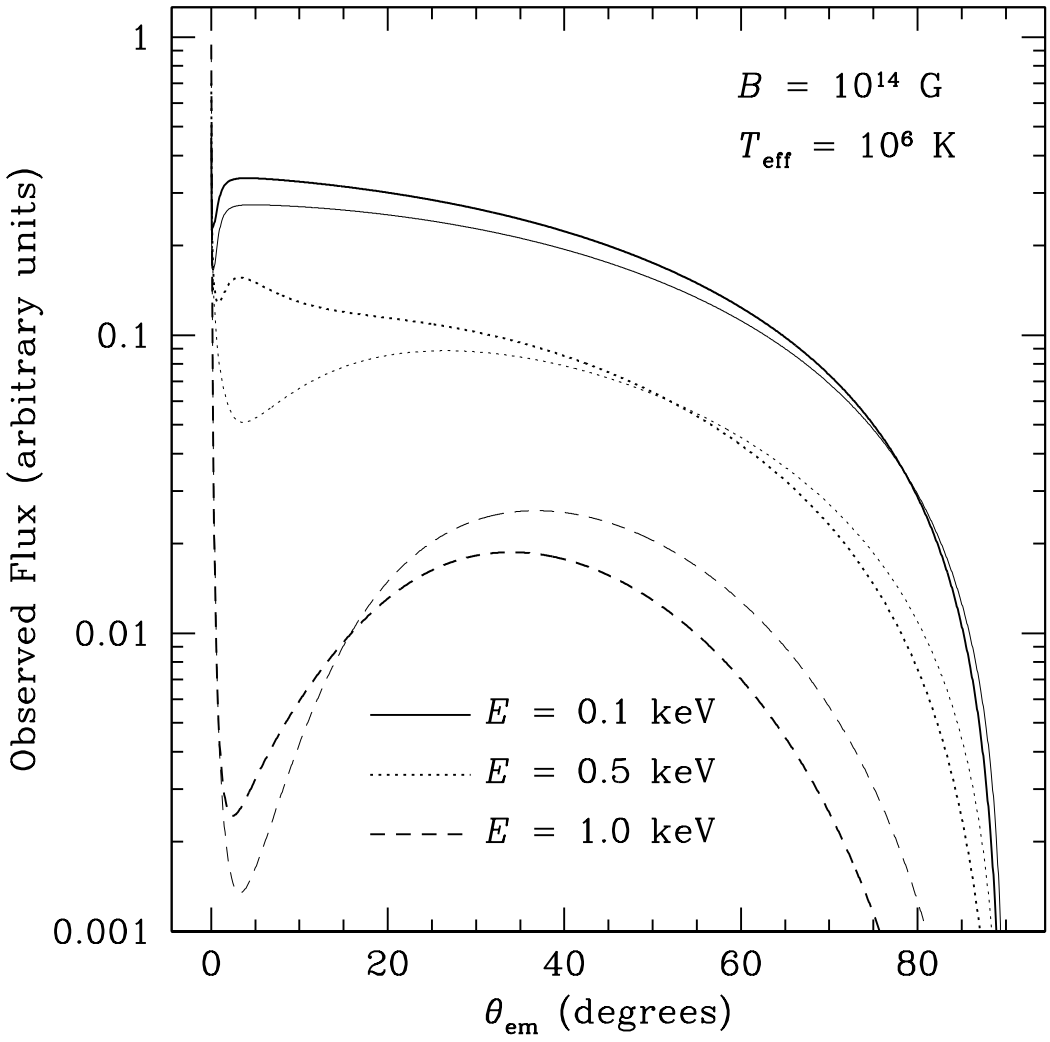

Figure 3.18: Same as Fig. 3.16 except for $B = 10^{14}$ G.

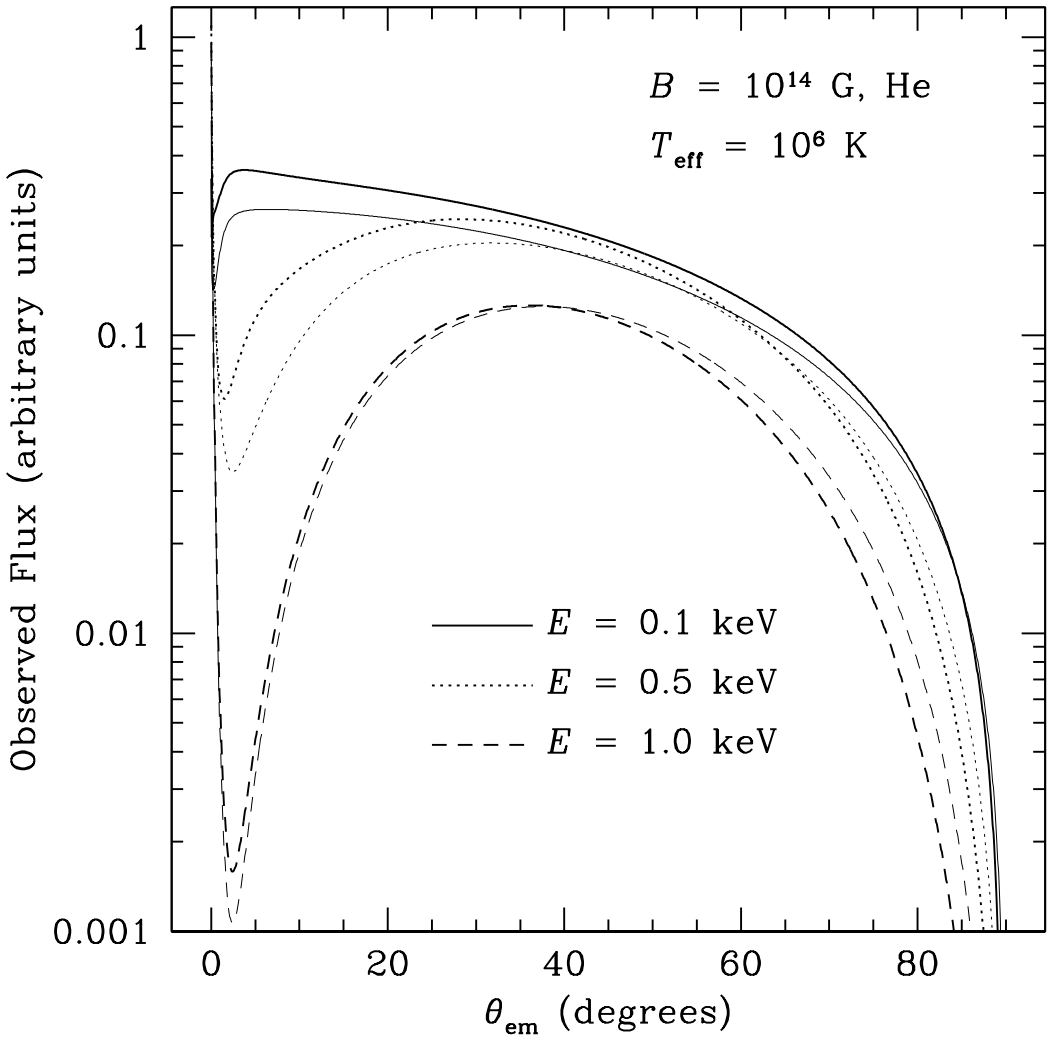

Figure 3.19: Same as Fig. 3.18 except for He composition.

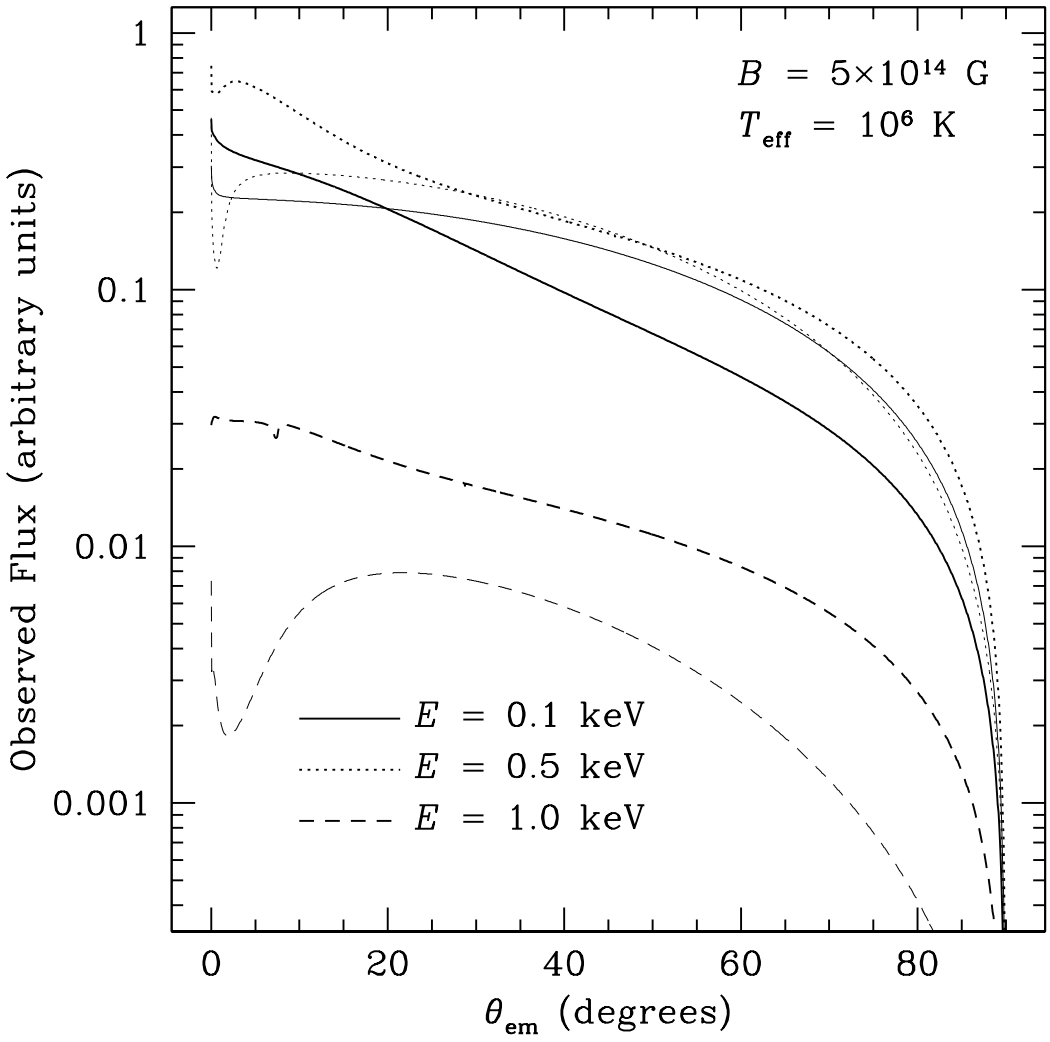

Figure 3.20: Same as Fig. 3.16 except for $B = 5 \times 10^{14}$ G.

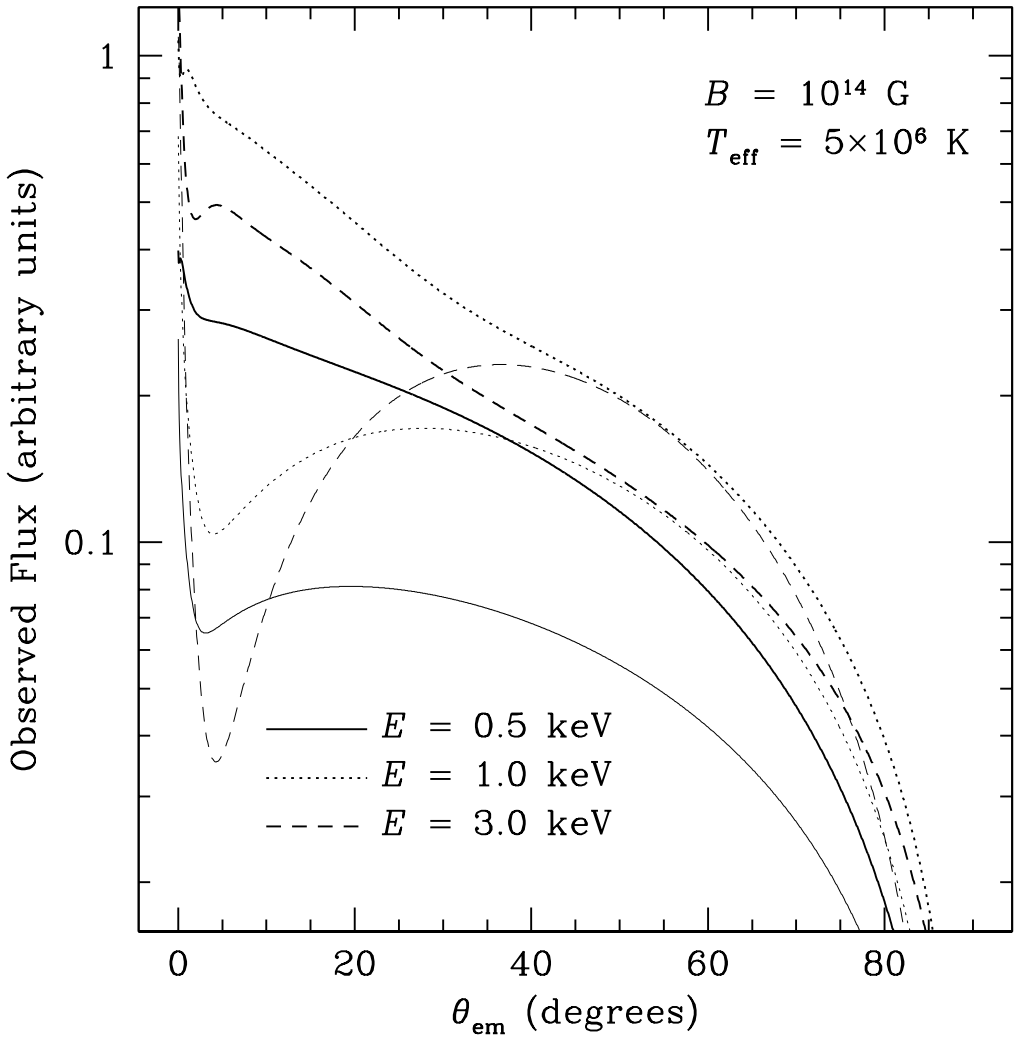

Figure 3.21: Same as Fig. 3.16 except for $B = 10^{14}$ G, $T_{\rm eff} = 5 \times 10^6$ K.

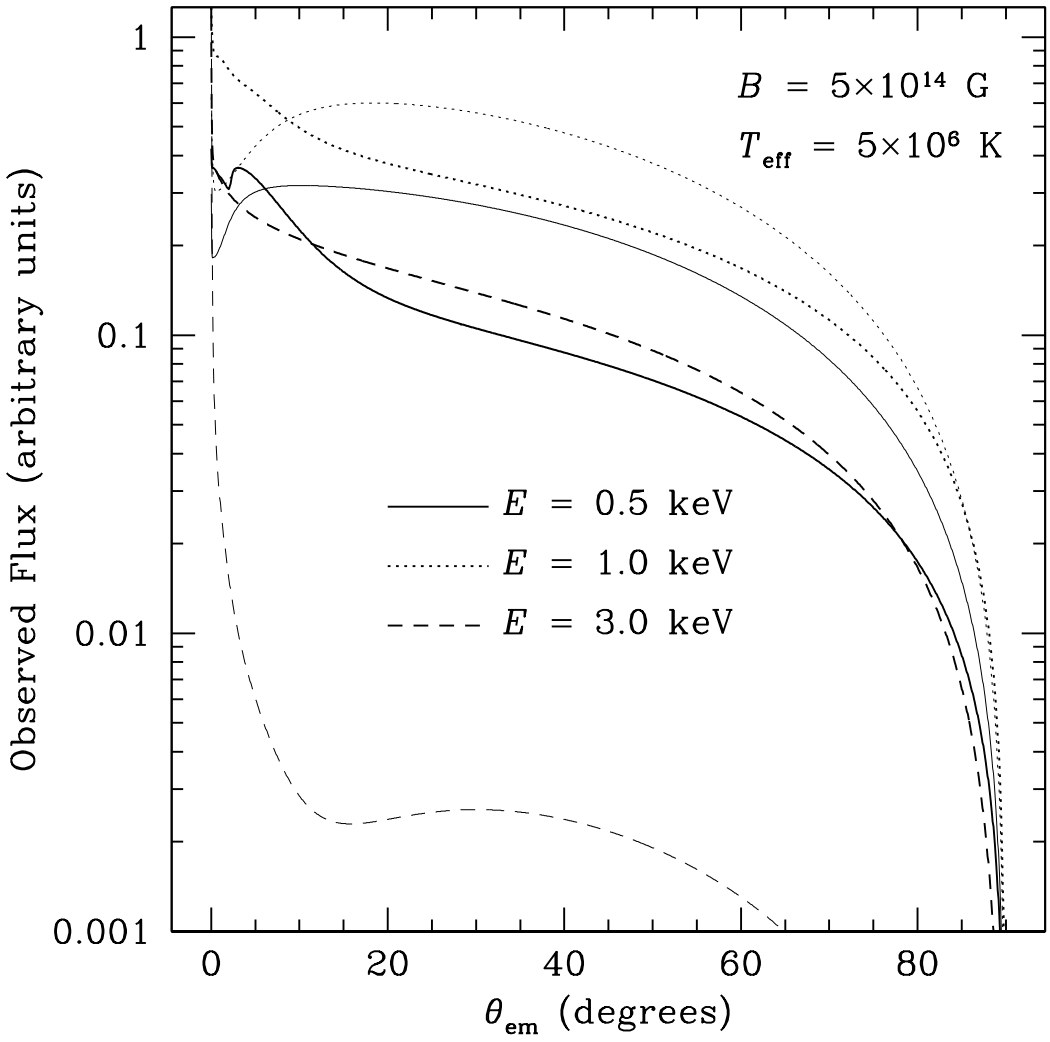

Figure 3.22: Same as Fig. 3.16 except for $B = 5 \times 10^{14}$ G, $T_{\rm eff} = 5 \times 10^6$ K.

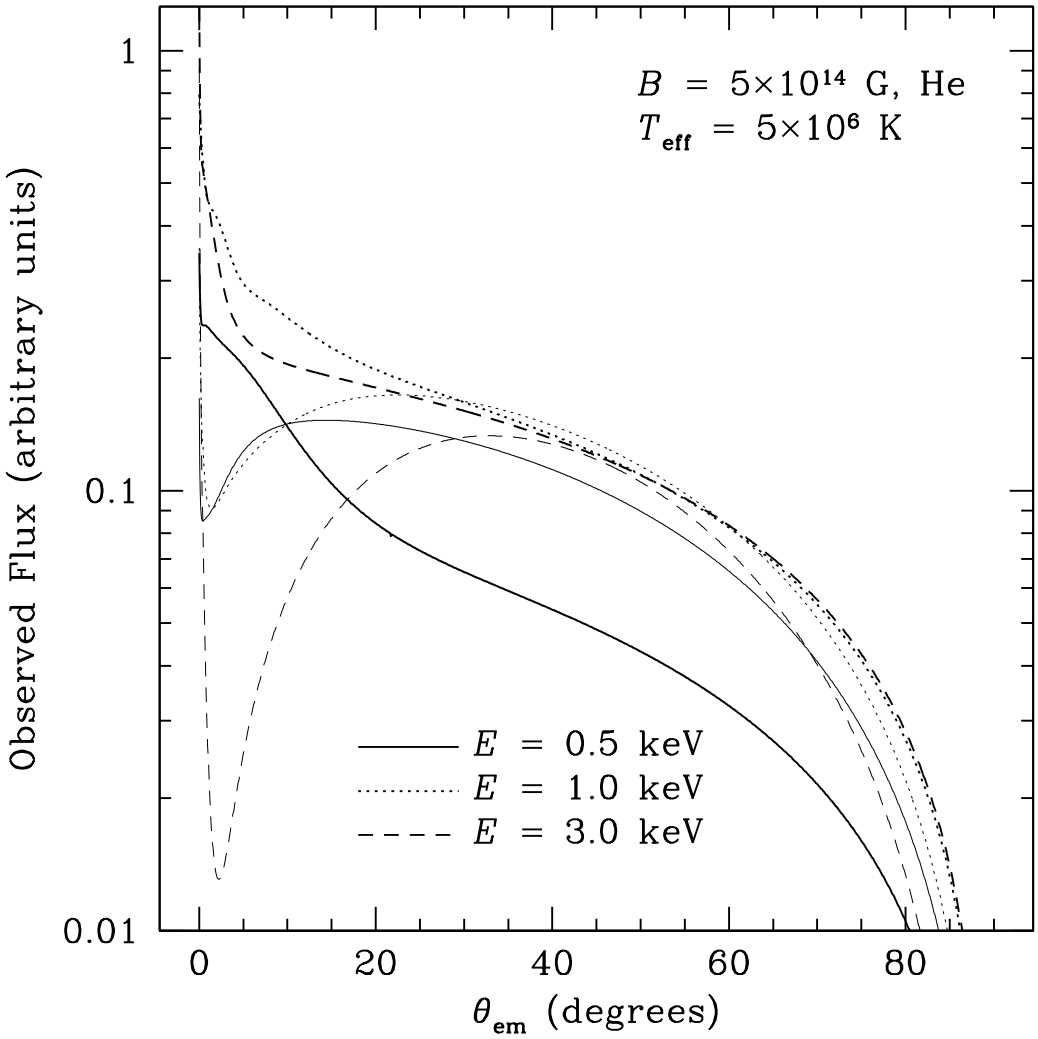

Figure 3.23: Same as Fig. 3.16 except for $B = 5 \times 10^{14}$ G, $T_{\rm eff} = 5 \times 10^6$ K, He composition.

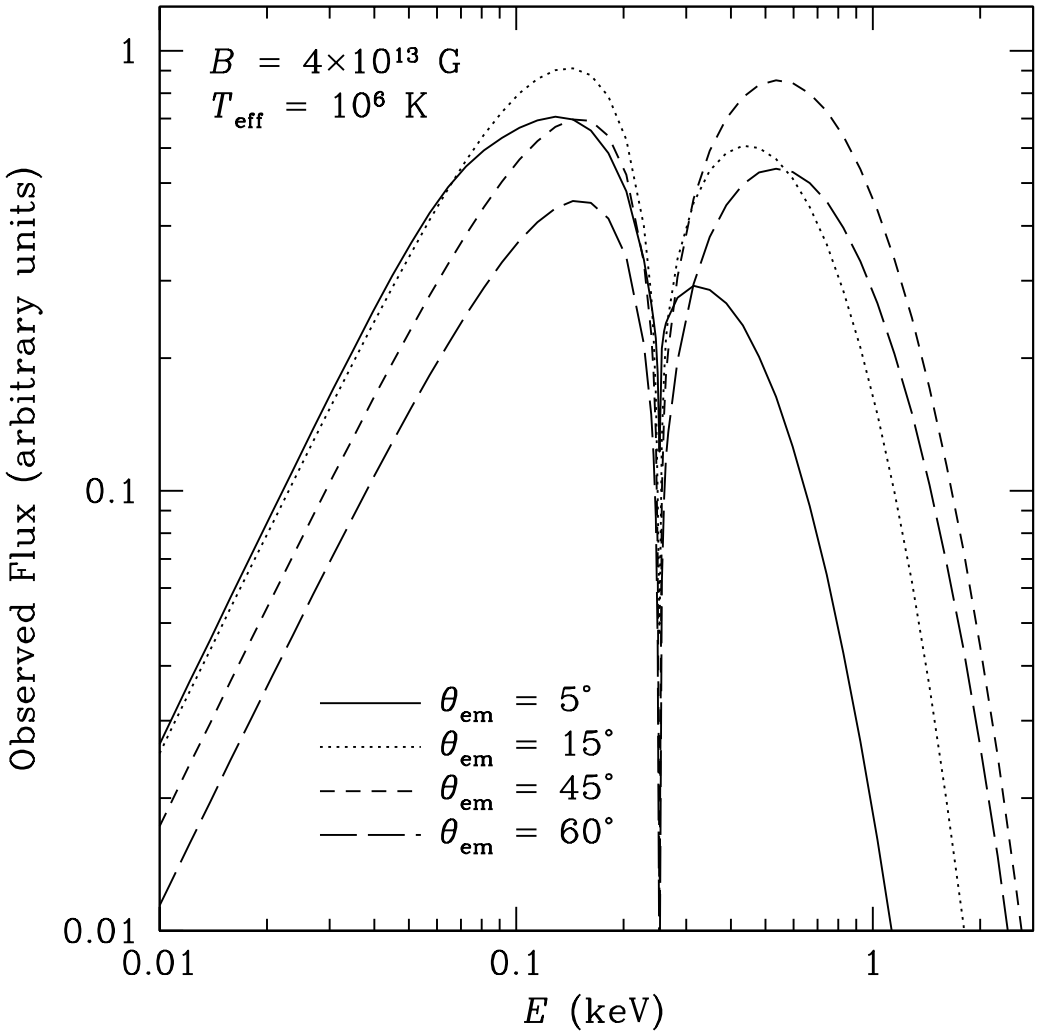

Figure 3.24: Observed spectral flux at emission angles $\theta_{\rm em} = 5^\circ, 15^\circ, 45^\circ, 60^\circ$, for the NS atmosphere model with $B = 4 \times 10^{13}$ G and $T_{\rm eff} = 10^6$ K.

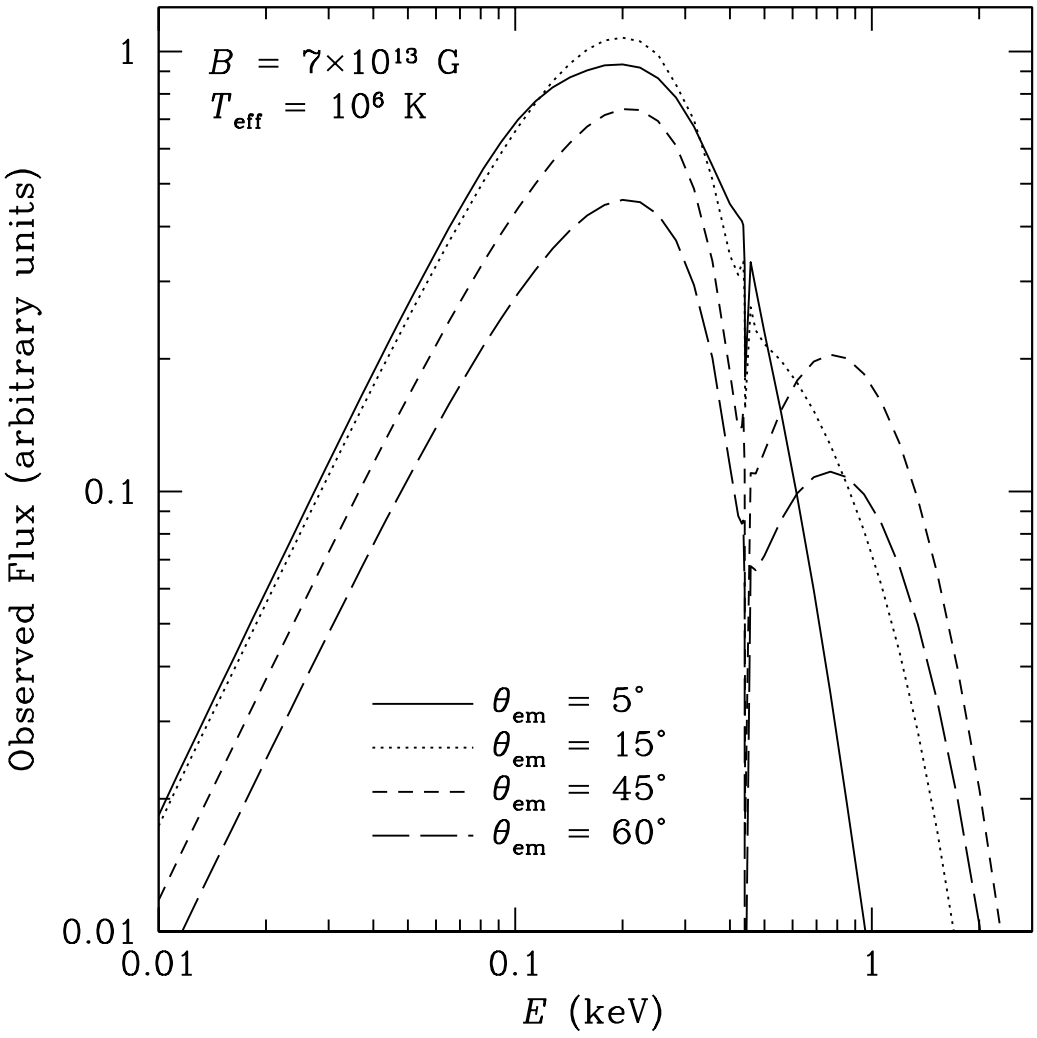

Figure 3.25: Same as Fig. 3.24, except for $B = 7 \times 10^{13}$ G.

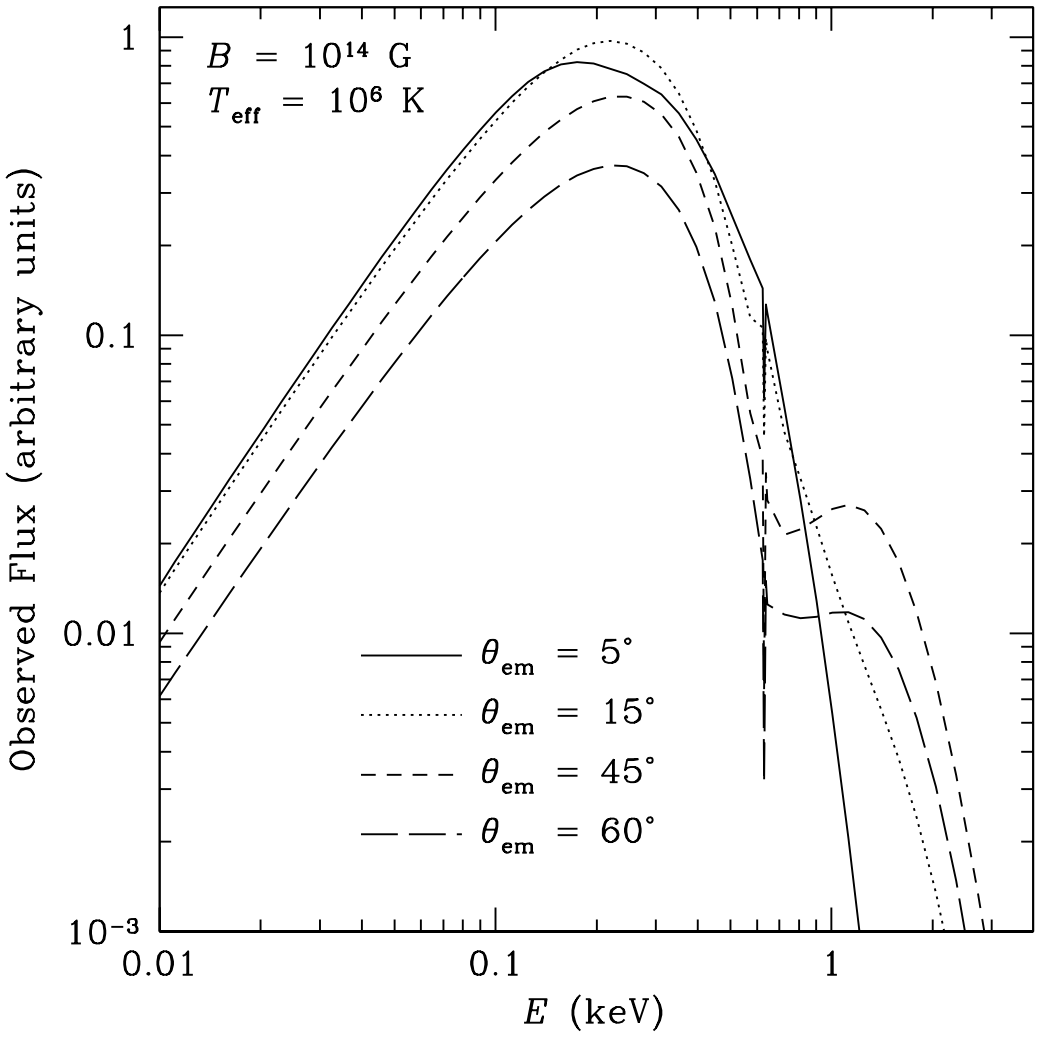

Figure 3.26: Same as Fig. 3.24, except for $B = 10^{14}$ G.

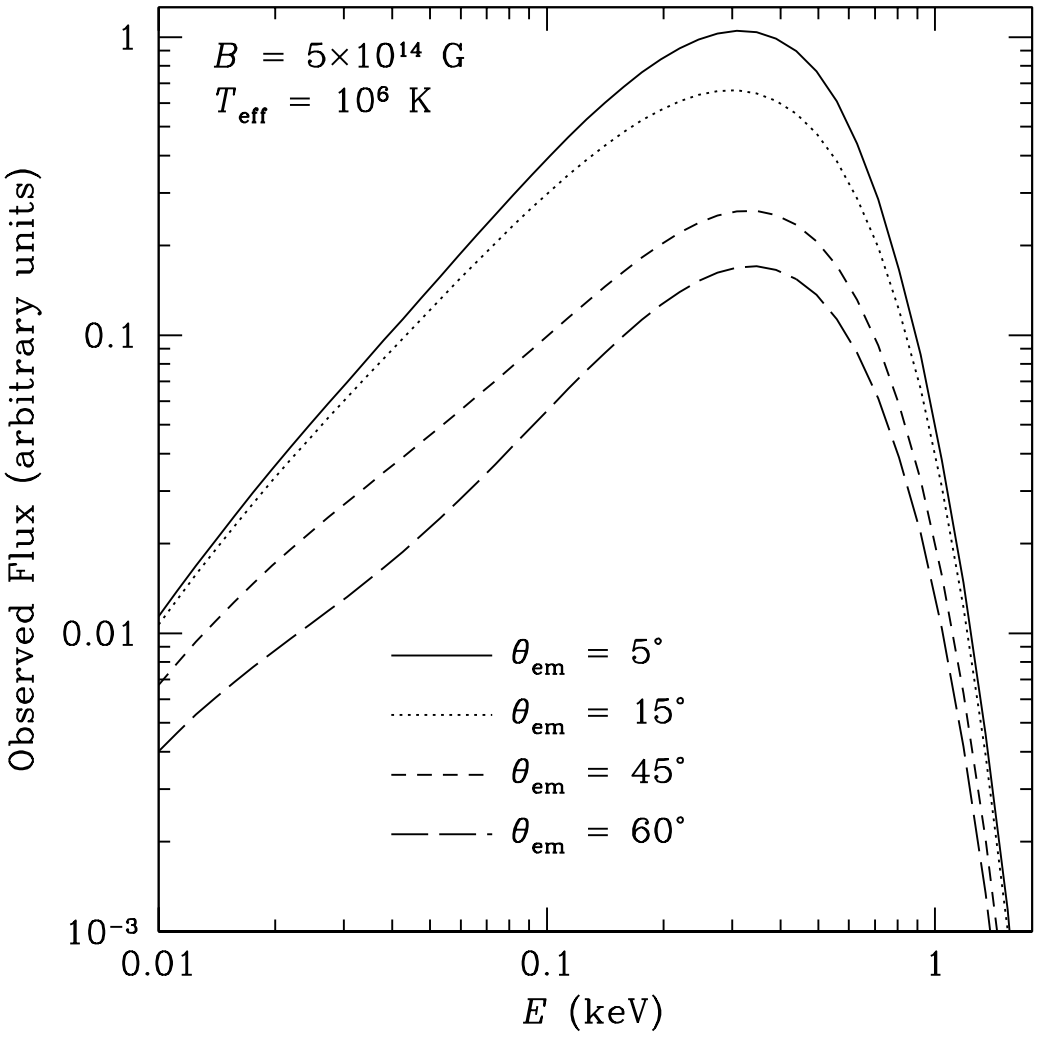

Figure 3.27: Same as Fig. 3.24, except for $B = 5 \times 10^{14}$ G.

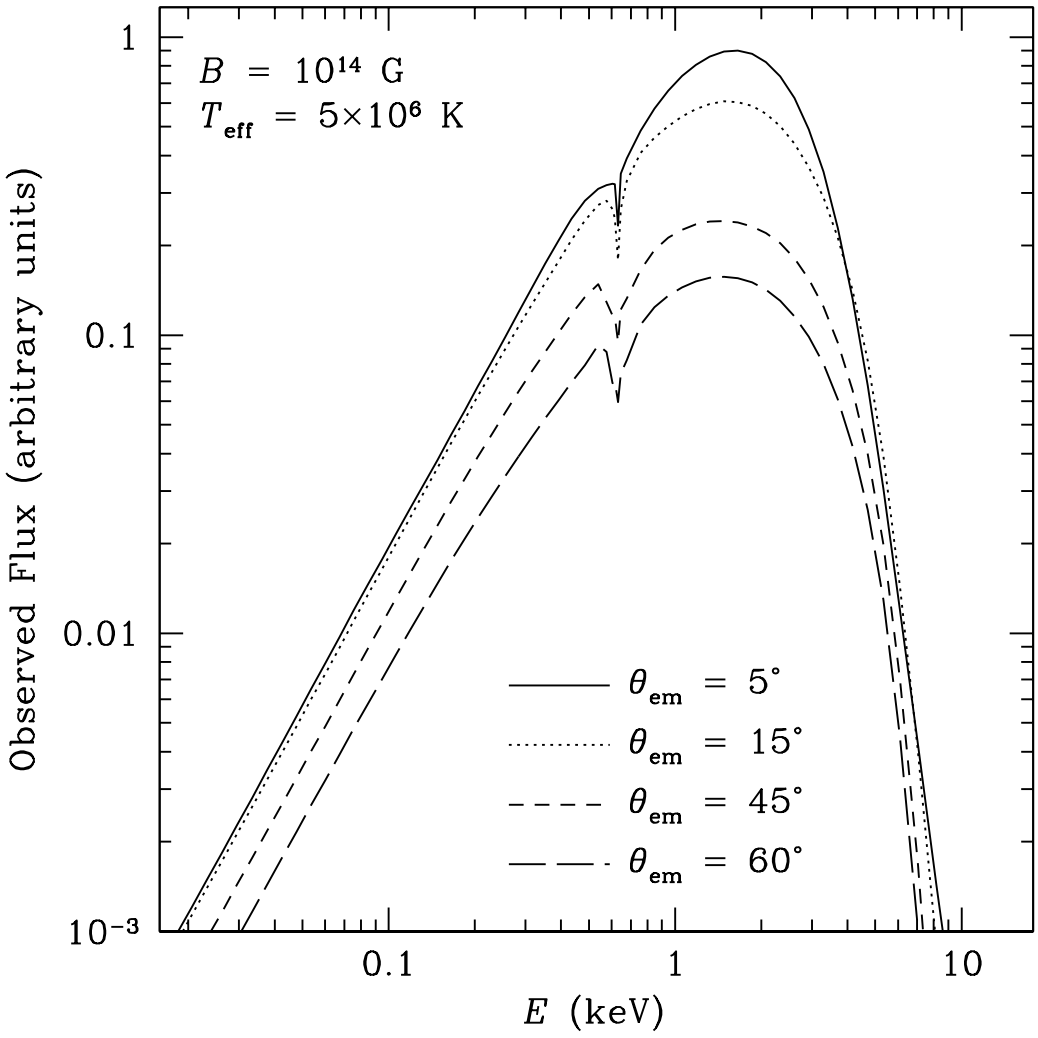

Figure 3.28: Same as Fig. 3.24, except for $B = 10^{14}$ G, $T_{\rm eff} = 5 \times 10^6$ K.

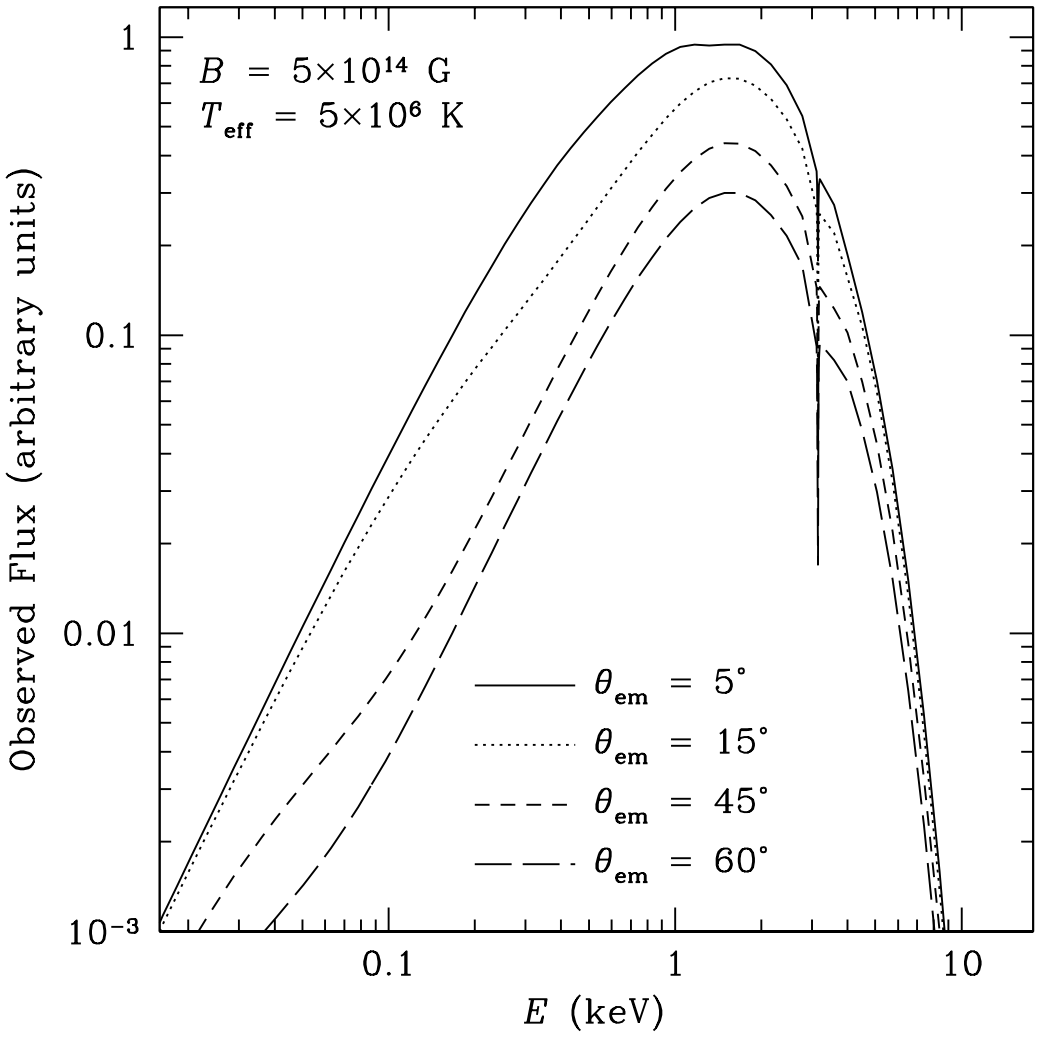

Figure 3.29: Same as Fig. 3.24, except for $B = 5 \times 10^{14}$ G, $T_{\rm eff} = 5 \times 10^6$ K.

Chapter 4

Polarization of the Atmosphere Emission

Thermal emission from a magnetized NS atmosphere is highly polarized. This arises from that fact that the typical X-mode photon opacity is much smaller than the O-mode opacity,[1] $\kappa_{\rm X} \sim (E/E_{Be})^2 \kappa_{\rm O} \ll \kappa_{\rm O}$. Thus, X-mode photons escape from deeper, hotter layers of the NS atmosphere than O-mode photons, and the emergent radiation is linearly polarized to a high degree (as high as 100%; see Gnedin & Sunyaev, 1974; Meszaros et al., 1988; Pavlov & Zavlin, 2000).

There has been some recent interest in X-ray polarimetry for NSs (Costa et al., 2001, 2006). Observations of X-ray polarization, particularly when phase-resolved and measured in different energy bands, can provide useful constraints on the magnetic field strength and geometry, the NS rotation rate, and compactness. This information is highly complimentary to that obtained from spectra and lightcurves. Moreover, as we show below (see also Lai & Ho, 2003b), vacuum resonance gives rise to a unique polarization signature in the surface emission, even for NSs with moderate ($B \sim 10^{12} - 10^{13}$ G) magnetic fields.

Below, we calculate the observed X-ray polarization signals in the case when the emission comes from a rotating magnetic hotspot on the NS surface. Although this represents the simplest situation, it captures the essential properties of the polarization signals, and the result can be carried over to more general situations. See the end of §4.3 for a discussion of the case when emission comes from an extended area (or the whole) of the stellar surface.

[1] This applies under typical conditions, when the photon energy E is much less than the electron cyclotron energy E_{Be}, is not too close to the ion cyclotron energy E_{Bi}, the plasma density is not too close to the vacuum resonance (see the text), and θ_{kB} (the angle between $\mathbf{k}$ and $\mathbf{B}$) is not too close to 0° or 180°.

4.1 Geometry and Lightcurves

To calculate the observed lightcurves and polarization signals, we set up a fixed coordinate system XYZ with the Z-axis along the line-of-sight (pointing from the NS toward the observer), and the X-axis in the plane spanned by the Z-axis and $\mathbf{\Omega}$ (the spin angular velocity vector). The angle between $\mathbf{\Omega}$ and $\hat{\mathbf{e}}_Z$ is denoted by γ. The hotspot is assumed to be at the intersection of the NS surface and dipole magnetic axis, which is inclined at an angle η relative to the spin axis. As the star rotates, the angle Θ between the magnetic axis $\boldsymbol{\mu}$ and the line of sight varies according to

$$\cos\Theta = \cos\gamma\cos\eta - \sin\gamma\sin\eta\cos\psi, \tag{4.1}$$

where $\psi = (\Omega t + \text{constant})$ is the rotation phase ($\psi = 0$ when $\boldsymbol{\mu}$ lies in the XZ plane). We use the simplified formalism derived by Beloborodov (2002) to calculate the observed spectral flux from the area dS of the hotspot, which takes the form

$$F_{\rm obs} = \left(1 - \frac{r_g}{R}\right)^{3/2} I_\nu(\theta_{\rm em})\cos\theta_{\rm em}\frac{dS}{D^2}, \tag{4.2}$$

where $r_g = 2GM/c^2$ is the Schwarzschild radius, R is the NS radius, and $\theta_{\rm em}$ (the angle between the photon direction and the surface normal at the emission point) is related to Θ through:

$$\cos\theta_{\rm em} = \frac{r_g}{R} + \left(1 - \frac{r_g}{R}\right)\cos\Theta. \tag{4.3}$$

For $R > 3r_g$, the spectral flux calculated using eq. (4.2) differs from the exact treatment (see Pechenick et al., 1983) by less than 1%.

The top panels of Figs. 4.1-4.3 show lightcurves for NS models with several magnetic field strengths, at a range of energies $E = 0.5 - 3$ keV, with geometry $\gamma = 30°$, $\eta = 70°$.

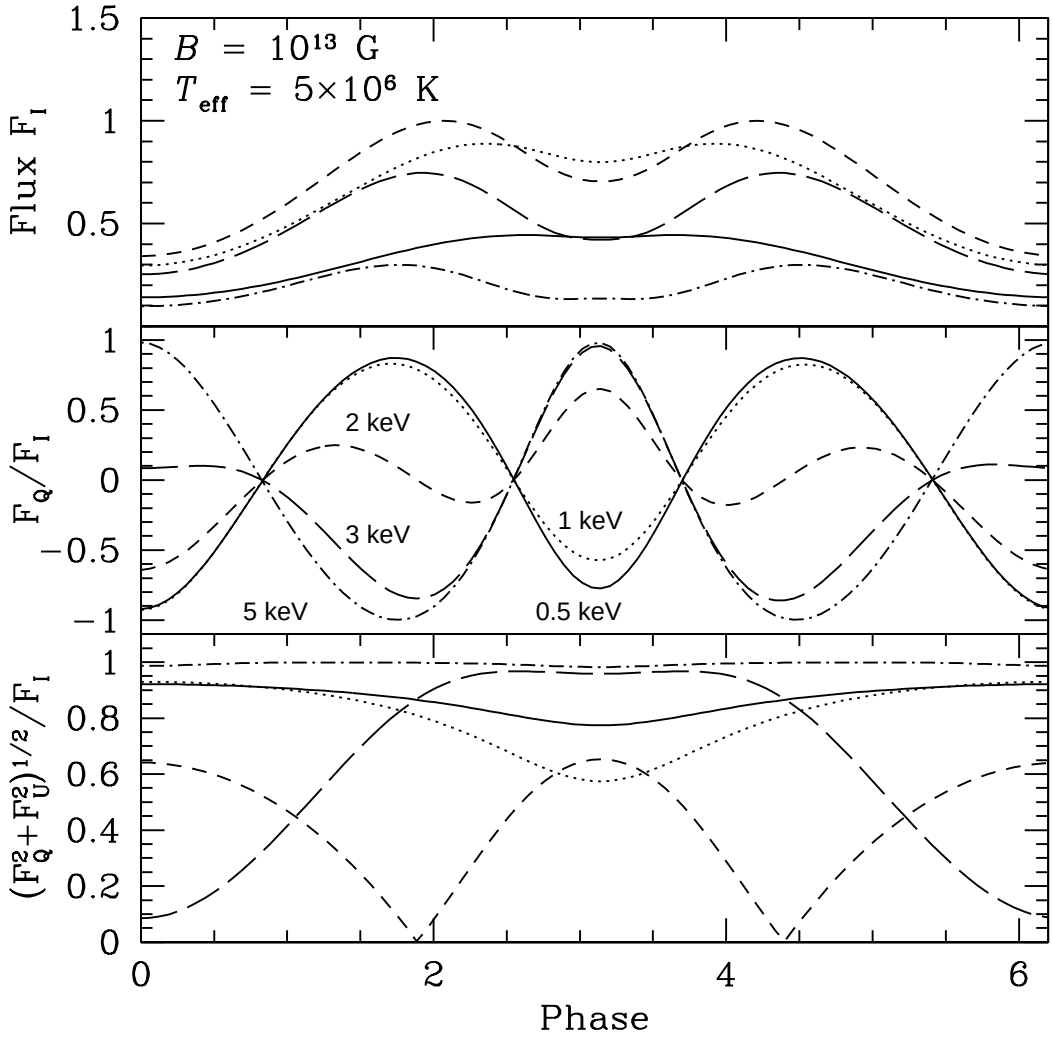

Figure 4.1: Lightcurve and polarization as a function of rotation phase for a NS hotspot with $B = 10^{13}$ G, $T_{\rm eff} = 5 \times 10^6$ K. The angle of the spin axis relative to the line of sight is $\gamma = 30°$, and the inclination of the magnetic axis relative to the spin axis is $\eta = 70°$. Note that the sign of the F_Q Stokes parameter is opposite for low and high energy photons; this implies that the planes of polarization for low and high energy photons are perpendicular. This is a unique signature of vacuum polarization for models with $B < B_l$.

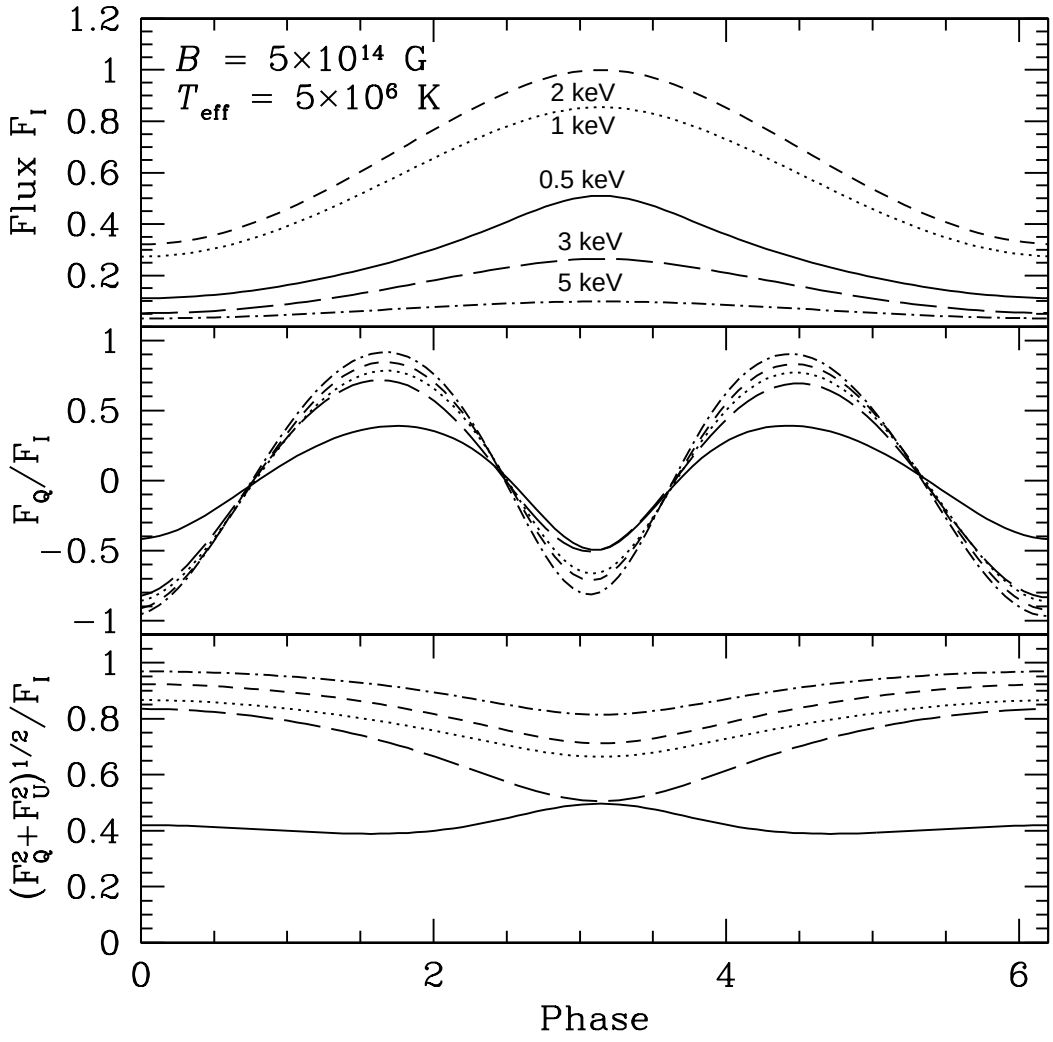

Figure 4.2: Same as Fig. 4.1 with $B = 5 \times 10^{14}$ G. At this field strength, $B > B_l$, and the vacuum resonance lies between the O and X-mode photospheres. Thus, the sign of the F_Q Stokes parameter for low and high energy photons is the same. Note that in the top panel, the flux for the 0.5 keV case is multiplied by a factor of 10 relative to the other curves.

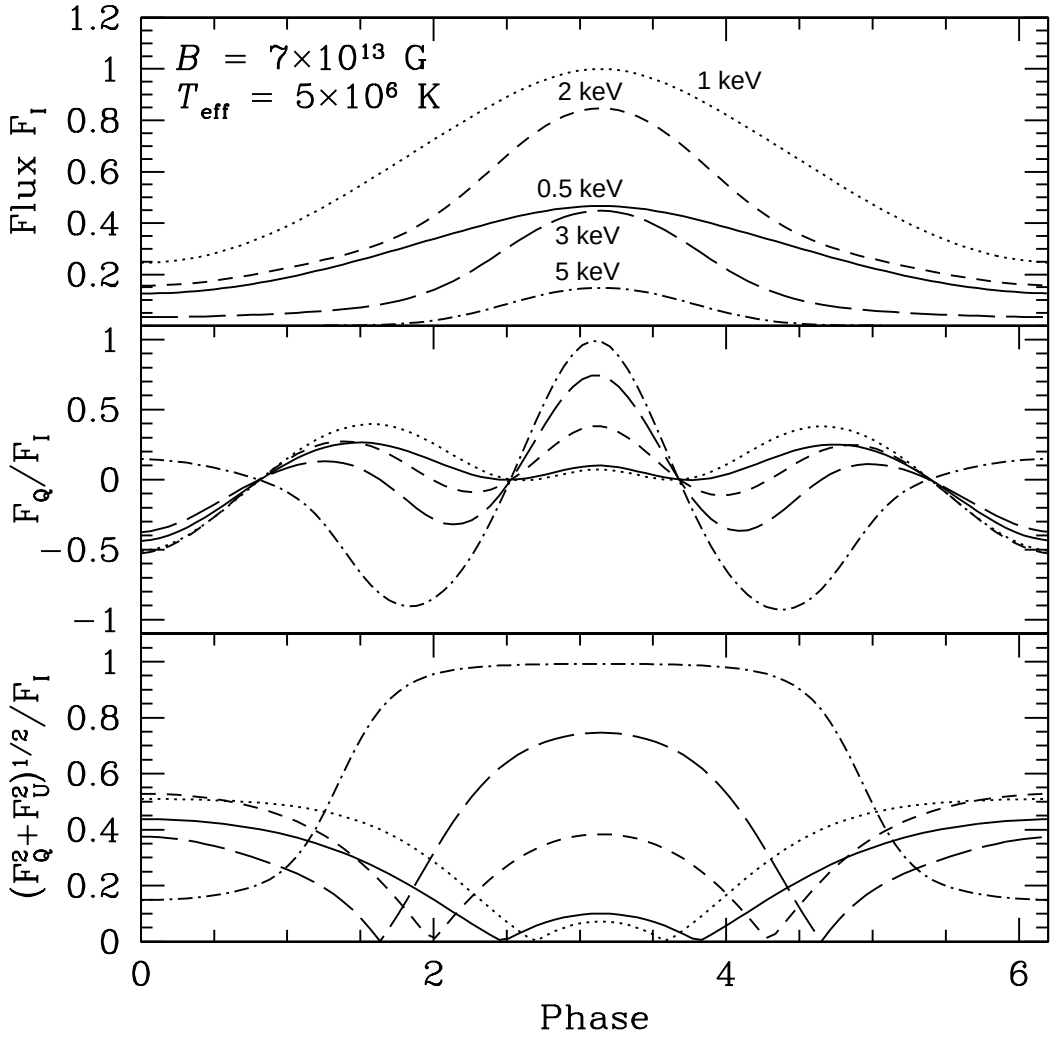

Figure 4.3: Same as Fig. 4.1 with $B = 7 \times 10^{13}$ G. For this model, $B \sim B_l$, representing the transition between the models shown in Figs. 4.1 and 4.2.

4.2 Observed Linear Polarization Signals

The atmosphere models presented in Chapter 3 yield the specific intensities $I_\nu^{\rm X}(\theta_{\rm em})$ and $I_\nu^{\rm O}(\theta_{\rm em})$ of the two photon modes, emerging from the NS atmosphere (outside the vacuum resonance layer). To determine the observed polarization signals, it is important to consider propagation of the polarized radiation in the NS magnetosphere. In the X-ray band, the magnetospheric dielectric properties are dominated by vacuum polarization (Heyl & Shaviv, 2002). Heyl et al. (2003) evolved the Stokes parameters along photon geodesics in the magnetosphere and showed that the observed polarization is determined at the so-called "polarization limiting radius," a distance far from the NS surface. Below we present a simple calculation of the propagation effect and observed linear polarization (see also Lai & Ho, 2003b).

Consider a photon emitted at time t_i from the hotspot, with rotation phase $\psi_i = \Omega t_i$. The emission point has polar angle Θ_i (relative to the fixed XYZ frame) given by eq. (4.1) with $\psi = \psi_i$, and azimuthal angle φ_i given by

$$\tan\varphi_i = \frac{\sin\eta\,\sin\psi_i}{\sin\eta\cos\gamma\cos\psi_i + \cos\eta\sin\gamma}. \tag{4.4}$$

This is also the angle $[\varphi_i = \varphi_B(R)]$ between the projection of the magnetic axis in the XY plane and the X-axis. After the photon leaves the star, it travels towards the observer, with a trajectory given by

$$\mathbf{r} = (R\sin\Theta_i\cos\phi_i + \Delta_X)\,\hat{X} + (R\sin\Theta_i\sin\phi_i + \Delta_Y)\,\hat{Y} + (R\cos\Theta_i + s + \Delta_Z)\,\hat{Z}, \tag{4.5}$$

where $s = c\Delta t = c(t - t_i)$, $\Delta_{X,Y,Z}$ are relativistic corrections (which, as we will see shortly, are unimportant for the polarization signals), and $\hat{X}$, $\hat{Y}$, $\hat{Z}$ are unit vectors. As the photon propagates in the magnetosphere, it will "see" a changing

stellar magnetic field, given by $\mathbf{B} = -\nabla(\boldsymbol{\mu} \cdot \mathbf{r}/r^3)$, where[2]

$$\boldsymbol{\mu} = \mu \Big[(\sin\eta\cos\gamma\cos\psi + \cos\eta\sin\gamma)\,\hat{X} + \sin\eta\sin\psi\,\hat{Y} + (\cos\eta\cos\gamma - \sin\eta\sin\gamma\cos\psi)\,\hat{Z} \Big], \tag{4.6}$$

with $\psi = \Omega t = \psi_i + \Omega\Delta t = \psi_i + s/r_l$ (here $r_l = c/\Omega$ is the radius of the light cyclinder). The photon's polarization state will evolve adiabatically, following the varying magnetic field that the photon experiences, up to the polarization limiting radius $r_{\rm pl}$ beyond which the polarization is frozen. Since we anticipate $r_{\rm pl} \gg R$, we consider only the region far from the NS. For $r \gg R$, the photon trajectory is simply $\mathbf{r} \simeq s\,\hat{Z}$, and the magnetic field along the photon path is $\mathbf{B} \simeq (2\mu_Z\hat{Z} - \mu_X\hat{X} - \mu_Y\hat{Y})/r^3$, with $r \simeq s$. This magnetic field has magnitude

$$B(s) = \frac{B_s}{2}\left(\frac{R}{r}\right)^3 \left[1 + 3\left(\cos\eta\cos\gamma - \sin\gamma\sin\eta\cos\psi\right)^2\right]^{1/2}, \tag{4.7}$$

where $B_s = 2\mu/R^3$ is the magnitude of the (dipole) surface field strength at the magnetic pole. The magnetic field is inclined at an angle θ_{kB} to the line of sight, and makes an azimuthal angle φ_B in the XY plane such that:

$$\sin^2\theta_{kB}(s) = \frac{1 - \left(\cos\eta\cos\gamma - \sin\gamma\sin\eta\cos\psi\right)^2}{1 + 3\left(\cos\eta\cos\gamma - \sin\gamma\sin\eta\cos\psi\right)^2}, \tag{4.8}$$

$$\tan\varphi_B(s) = \frac{\sin\eta\sin\psi}{\cos\eta\sin\gamma + \cos\gamma\sin\eta\cos\psi}. \tag{4.9}$$

Recall that in Eqs. (4.7)-(4.9), $\psi = \psi_i + s/r_l = \Omega t_i + s/r_l$ and s is the affine parameter along the ray.

The wave equation for photon propagation in a magnetized medium takes the form

$$\nabla \times (\bar{\boldsymbol{\mu}} \cdot \nabla \times \mathbf{E}) = \frac{\omega^2}{c^2}\boldsymbol{\epsilon} \cdot \mathbf{E}, \tag{4.10}$$

[2]We restrict the propagation to the "near zone" of the star, i.e., $r < r_l = c/\Omega$.

where $\mathbf{E}$ is the electric field (not to be confused with the photon energy), and $\boldsymbol{\epsilon}$, $\bar{\boldsymbol{\mu}}$ are the dielectric and inverse permeability tensors, respectively. In the magnetized vacuum of the NS magnetosphere, they are given by $\boldsymbol{\epsilon} = a\mathbf{I} + q\hat{\mathbf{B}}\hat{\mathbf{B}}$ and $\bar{\boldsymbol{\mu}} = a\mathbf{I} + m\hat{\mathbf{B}}\hat{\mathbf{B}}$. Solving eq. (4.10) for EM waves with $E \propto e^{iks-i\omega t}$ yields the two modes (in the XY basis)

$$\mathbf{e}_{\rm O} = (\cos\varphi_B, \sin\varphi_B), \quad \mathbf{e}_{\rm X} = (-\sin\varphi_B, \cos\varphi_B), \tag{4.11}$$

with indices of refraction $n_{\rm O} \simeq 1 + (q/2)\sin^2\theta_{kB}$ and $n_{\rm X} \simeq 1 - (m/2)\sin^2\theta_{kB}$. A general (transverse) EM wave can be written as a superposition of the two modes:

$$\mathbf{E} = \mathcal{A}_{\rm O}\mathbf{e}_{\rm O} + \mathcal{A}_{\rm X}\mathbf{e}_{\rm X}. \tag{4.12}$$

Following the steps of Lai & Ho (2002) [see their eq. (15)], we derive the following equations for the evolution of the mode amplitudes:

$$i\begin{pmatrix} \mathcal{A}'_{\rm O} \\ \mathcal{A}'_{\rm X} \end{pmatrix} \simeq \begin{pmatrix} -(\omega/c)\Delta n/2 & i\varphi'_B \\ -i\varphi'_B & (\omega/c)\Delta n/2 \end{pmatrix}\begin{pmatrix} \mathcal{A}_{\rm O} \\ \mathcal{A}_{\rm X} \end{pmatrix}, \tag{4.13}$$

where the prime (') denotes a derivative with respect to s, and $\Delta n = n_{\rm O} - n_{\rm X} = \frac{1}{2}(q+m)\sin^2\theta_{kB}$. The condition for adiabatic evolution of photon modes is

$$(\omega/c)\Delta n \gg 2\varphi'_B. \tag{4.14}$$

Near the star ($r \sim R$), $\varphi_B \sim 1/r$, and the adiabatic condition is easily satisfied. Far from the star, $r \gg R$; using eq. (4.7), we write:

$$\Delta n = \frac{\alpha}{30\pi}\left(\frac{B}{B_Q}\right)^2 \sin^2\theta_{kB} = 9.94\times10^{-9}B_{12}^2\left(\frac{R}{r}\right)^6 F_B, \tag{4.15}$$

where

$$F_B = 1 - (\cos\eta\cos\gamma - \sin\gamma\sin\eta\cos\psi)^2, \tag{4.16}$$

and $B_{12} = B_s/(10^{12}\mathrm{G})$. From eq. (4.9), we have

$$\frac{d\varphi_B}{ds} = \frac{1}{r_l} F_\varphi, \tag{4.17}$$

with

$$F_\varphi = \left(\sin^2\eta\cos\gamma + \sin\eta\cos\eta\sin\gamma\cos\psi\right)/F_B. \tag{4.18}$$

The polarization-limiting radius $r_{\rm pl}$ is set by the condition $\omega\Delta n/c = 2\varphi'_B$. Substituting in eqs. (4.15) and (4.17), we find[3]

$$\frac{r_{\rm pl}}{R} = 32.6\left(\frac{E_1 B_{12}^2 F_B}{f_1\, F_\varphi}\right)^{1/6}, \tag{4.19}$$

where f_1 is the spin frequency $\Omega/(2\pi)$ in Hz, and F_B, F_φ are slowly varying functions of phase and are of order unity. Note that the above analysis is valid only if $r_{\rm pl} \lesssim r_l/2$, since beyond the light-cylinder radius the magnetic field is no longer described by a static dipole. Thus we require that

$$\frac{r_{\rm pl}}{r_l} \simeq 6.84\times10^{-3}\left(\frac{E_1 B_{12}^2 F_B}{F_\varphi}\right)^{1/6} R_{10}\, f_1^{5/6} \lesssim 0.5, \tag{4.20}$$

where $R_{10} = R/(10\ \mathrm{km})$.

Beyond $r_{\rm pl}$, the polarization state of the photon is "frozen." Using eq. (4.11), the observed Stokes parameters in the observer coordinate system (XYZ) are given by

$$I = I_{\rm O} + I_{\rm X}, \tag{4.21}$$

$$Q \simeq (I_{\rm O} - I_{\rm X})\cos 2\varphi_B(r_{\rm pl}), \tag{4.22}$$

$$U \simeq (I_{\rm O} - I_{\rm X})\sin 2\varphi_B(r_{\rm pl}), \tag{4.23}$$

where $I_{\rm O} \propto I_\nu^{\rm O}(\theta_{\rm em})$ and $I_{\rm X} \propto I_\nu^{\rm X}(\theta_{\rm em})$ are the specific mode intensities emitted at the NS surface [calculated with our models described in Chapter 3, and corrected

[3]Our expression for $r_{\rm pl}$ differs from that given in Heyl & Shaviv (2002) and Heyl et al. (2003).

for the general relativistic effect; see eqs. (4.2)-(4.3)], and $\varphi_B(r_{\rm pl})$ is evaluated at $s \simeq r = r_{\rm pl}$. From eqs. (4.4) and (4.9), with $\psi(r_{\rm pl}) = \psi_i + r_{\rm pl}/r_l$, we see that the effect of NS rotation is to shift the polarization lightcurve by a phase $r_{\rm pl}/r_l$. For slow rotation $r_{\rm pl}/r_l \ll 1$ [see eq. (4.20)] and this shift is small, yielding $\varphi_B(r_{\rm pl}) \simeq \varphi_i + \pi$. We calculate the observed spectral fluxes $F_I = F$, F_Q, F_U associated with the intensities I, Q, U using the standard procedure described in §4.1.

The middle and bottom panels of Figs. 4.1-4.3 show the phase evolution of the Stokes parameter F_Q and the degree of linear polarization, both normalized to the observed spectral flux. Note that Q is defined such that $Q = 1$ corresponds to linear polarization in the plane spanned by the line of sight Z and the NS spin axis. In Fig. 4.1, we consider emission from a NS hotspot with $B = 10^{13}$ G and $T_{\rm eff} = 5 \times 10^6$ K. Note that the value of F_Q for low energy photons ($E \lesssim 1$ keV) is of opposite sign to that of high energy photons ($E \gtrsim 3$ keV). This implies that the planes of polarization for low and high energy photons are perpendicular. This is a unique signature of vacuum polarization first identified by Lai & Ho (2003b), which occurs for $B < B_l$ [see eq. 3.5] because the vacuum resonance appears outside the O-mode photosphere. Below the vacuum resonace layer ($\rho > \rho_V$), the X-mode flux dominates over the O-mode. For low energy photons, $E \lesssim E_{ad}$, mode conversion is inefficient, and the emergent flux is dominated by the X-mode; for high energy photons $E \gtrsim E_{ad}$, mode conversion is efficient, rotating the plane of polarization, and the emergent flux is dominated by the O-mode [see Fig. 2 of Lai & Ho (2003b)].

Fig. 4.2 shows the same result for the model with $B = 5 \times 10^{14}$ G, $T_{\rm eff} = 5 \times 10^6$ K. In this case, $B > B_l$, the vacuum resonance appears inside the O and X-mode photospheres, and the emergent radiation is always dominated by the X-

mode. As expected, the planes of polarization for low and high energy photons are aligned. Fig. 4.3 shows an intermediate case, where $B \sim B_l$ — to calculate the spectra and polarization signals for such a model, it is particularly important to incorporate partial mode conversion properly. The distinct behavior between the low field and high field cases is illustrated by Fig. 4.4, which shows the phase-averaged F_Q Stokes parameter as a function of photon energy for several values of the magnetic field strength. The low-field cases show the characteristic rotation of the plane of polarization between low-E and high-E, whereas the high-field cases do not.

Note that in the above analysis, the observed linear polarization fraction Π_L (the bottom panel of Figs. 4.1-4.2) is the same as the value just outside the emission region, $|\Pi_{em}|$, i.e.,

$$\Pi_L = \frac{(Q^2+U^2)^{1/2}}{I} = |\Pi_{em}|, \qquad \text{with} \quad \Pi_{em} = \frac{I_\nu^O(\theta_{em}) - I_\nu^X(\theta_{em})}{I_\nu^O(\theta_{em}) + I_\nu^X(\theta_{em})}. \tag{4.24}$$

The polarized fluxes are simply

$$F_Q \simeq F_I \Pi_{em} \cos 2\varphi_B(r_{\rm pl}), \qquad F_U \simeq F_I \Pi_{em} \sin 2\varphi_B(r_{\rm pl}). \tag{4.25}$$

In §4.3 we shall see that for rapidly rotating NSs, the observed Π_L will be somewhat smaller than $|\Pi_{em}|$ because of the generation of circular polarization around $r_{\rm pl}$.

4.3 Circular Polarization

Circular polarization of surface emission may be generated for NSs with sufficiently rapid rotation, due to the gradual photon mode coupling and decoupling around $r_{\rm pl}$. While the linear polarization signals can be adequately described and calculated using the simple analysis given in §4.2, to calculate the circular polarization,

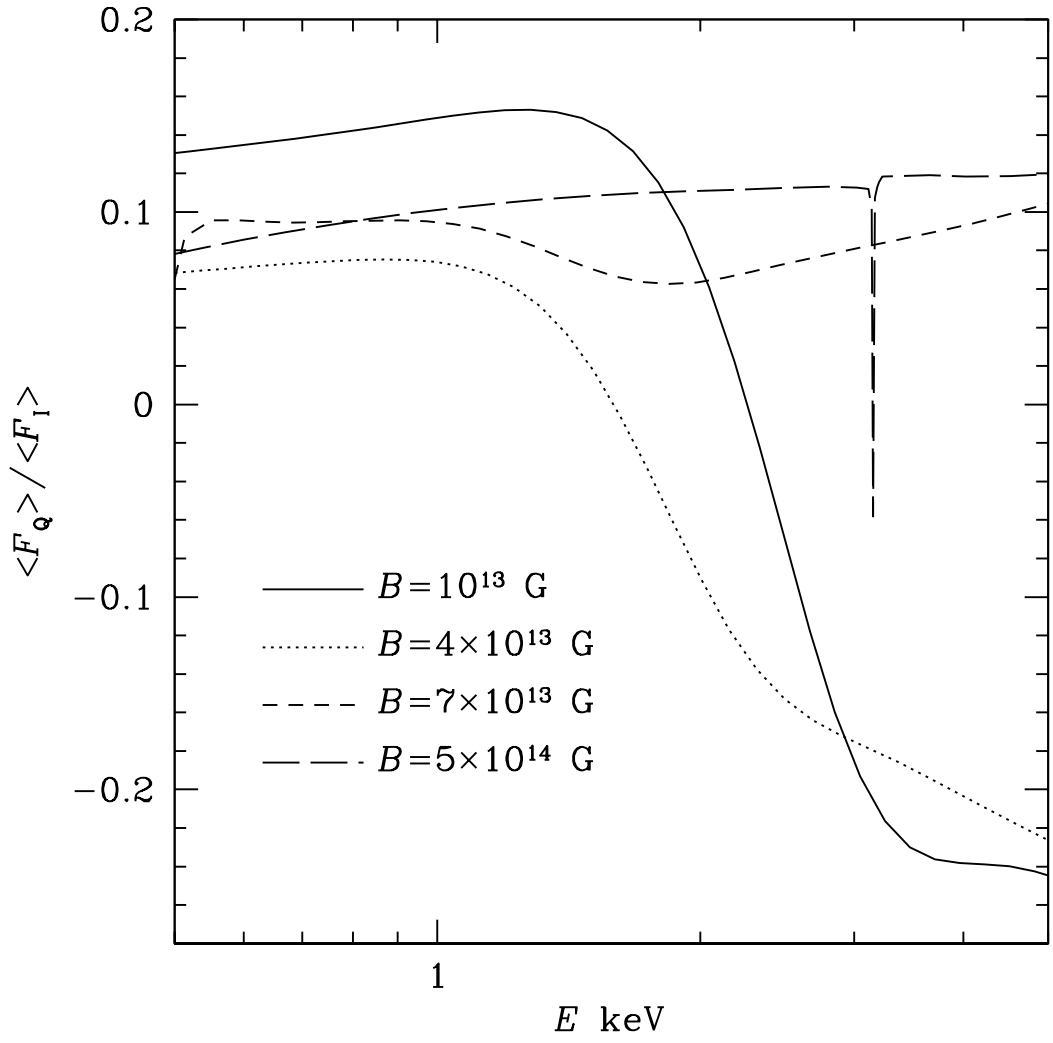

Figure 4.4: Phase-average of Stokes parameter F_Q as a function of photon energy for a rotating NS hotspot at magnetic field strengths $B = 10^{13}, 4 \times 10^{13}, 7 \times 10^{13}$ and 5×10^{14} G, with $T_{\rm eff} = 5 \times 10^6$ K. Note that the sign of $\langle F_Q \rangle$ changes between low and high photon energies for the low-field cases, corresponding to rotation of the plane of polarization.

quantitative solutions of the evolution equations for the modes or Stokes parameters in the magnetosphere are necessary.

Consider the mode evolution equations (4.13). For given initial values (e.g., the mode amplitudes at $r_i \ll r_{\rm pl}$), the solution of the equations depends on two parameters: C, defined by $(\omega/c)\Delta n \approx C/r^6$ and φ_B' (since ψ varies by a small amount along the ray path, F_B and F_φ are nearly constant). Alternatively, since $r_{\rm pl}$ is determined by $C/r^6 = 2\varphi_B'$, the solution depends only on the dimensionless parameter Γ, defined by

$$\Gamma \equiv r_{\rm pl}\varphi_B' = \frac{r_{\rm pl}}{r_l}\, F_\varphi \simeq 6.84\times 10^{-3}\left(E_1 B_{12}^2 F_B F_\varphi^5\right)^{1/6} R_{10}\, f_1^{5/6}. \tag{4.26}$$

Indeed, if we define $x = r/r_{\rm pl}$, eq. (4.13) can be rewritten as

$$i\frac{d}{dx}\begin{pmatrix} \mathcal{A}_{\rm O} \\ \mathcal{A}_{\rm X} \end{pmatrix} \simeq \Gamma \begin{pmatrix} -x^{-6} & i \\ -i & x^{-6} \end{pmatrix} \begin{pmatrix} \mathcal{A}_{\rm O} \\ \mathcal{A}_{\rm X} \end{pmatrix}. \tag{4.27}$$

Note that while eq. (4.13) is valid for all radii, the magnetostatic approximation for the field of a rotating dipole breaks down beyond the light-cylinder radius. Since $\varphi_B' \sim 1/r_l$, eq. (4.27) is valid only for $\Gamma \sim r_{\rm pl}/r_l \lesssim 0.5$.

The Stokes parameters can be written in terms of the mode amplitudes as

$$I = |E_X|^2 + |E_Y|^2 = |\mathcal{A}_{\rm O}|^2 + |\mathcal{A}_{\rm X}|^2, \tag{4.28}$$

$$Q = |E_X|^2 - |E_Y|^2 = \cos 2\varphi_B\left(|\mathcal{A}_{\rm O}|^2 - |\mathcal{A}_{\rm X}|^2\right) - 2\sin 2\varphi_B\, \Re e\left(\mathcal{A}_{\rm O}\mathcal{A}_{\rm X}^*\right), \tag{4.29}$$

$$U = 2\,\Re e\left(E_X E_Y^*\right) = \sin 2\varphi_B\left(|\mathcal{A}_{\rm O}|^2 - |\mathcal{A}_{\rm X}|^2\right) + 2\cos 2\varphi_B\, \Re e\left(\mathcal{A}_{\rm O}\mathcal{A}_{\rm X}^*\right), \tag{4.30}$$

$$V = 2\,\Im m\left(E_X E_Y^*\right) = 2\,\Im m\left(\mathcal{A}_{\rm O}\mathcal{A}_{\rm X}^*\right). \tag{4.31}$$

Figure 4.5 gives some examples of the results of numerical integration of eq. (4.27). We start the integration at radius $x_i = r_i/r_{\rm pl}$ such that the adiabatic

condition is well satisfied (we typically choose $x_i \lesssim 1/3$). In these examples, the initial values are $\mathcal{A}_{\rm O} = 1$, $\mathcal{A}_{\rm X} = 0$. After obtaining $\mathcal{A}_{\rm O}(x)$ and $\mathcal{A}_{\rm X}(x)$, we calculate the Stokes parameters using eqs. (4.28)-(4.31) with $\varphi_B = \varphi_B'(r - r_i) = \Gamma(x - x_i)$ (adding a constant to φ_B will affect Q and U, but not V). We see that for $x \lesssim 1/2$, the photon modes evolve adiabatically, and thus $Q \propto \cos 2\varphi_B$, $U \propto \sin 2\varphi_B$ [see eqs. (4.22)-(4.23)] and $V \simeq 0$. Around $x = 1$ ($r = r_{\rm pl}$), the modes couple and circular polarization is generated. For $x \gtrsim 2$, the values of the Stokes parameters are "frozen" and no longer evolve. NSs with large Γ (corresponding to rapid rotations: $f = 40$ Hz, $B = 10^{13}$ G, $E = 1$ keV yields $\Gamma \sim 0.3$) can generate appreciable circular polarization, with $V(r \to \infty)/I \approx -14\%$. As the NS spin frequency decreases, the resulting $|V/I|$ decreases.

Alternatively, using the relations (4.28)-(4.31) and the mode evolution equation (4.13), we can derive evolution equations for the Stokes parameters:

$$I' = 0, \tag{4.32}$$

$$Q' = (\omega\Delta n/c)\, V \, \sin 2\varphi_B, \tag{4.33}$$

$$U' = -(\omega\Delta n/c)\, V \, \cos 2\varphi_B, \tag{4.34}$$

$$V' = -(\omega\Delta n/c)\, Q \, \sin 2\varphi_B + (\omega\Delta n/c)\, U \, \cos 2\varphi_B. \tag{4.35}$$

Since the vacuum contribution to the dielectric tensor includes no dissipation, $I' = 0$ as expected. Equations (4.32)-(4.35) can be evolved numerically to calculate the observed Stokes parameters. Again we start the integration at a radius $r_i < r_{\rm pl}$ such that the adiabatic condition is well satisfied. Since the circular polarization does not depend on the orientation of the XY axes, we set the initial conditions at r_i by rotating the coordinate system azimuthally so that $I = 1$, $U = 0$ (this also corresponds to choosing $\psi = 0$ or $\varphi_B = 0$ at $r = r_i$), and $Q_i = \Pi_{em} \leq 1$, where Π_{em}

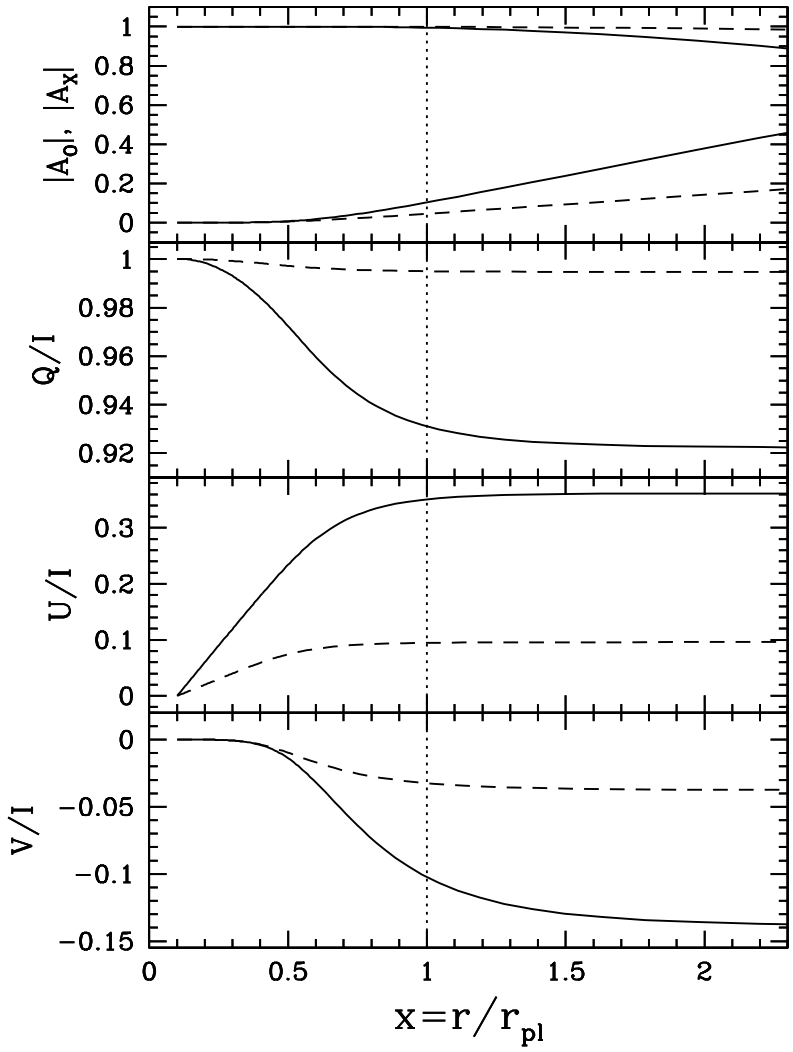

Figure 4.5: Evolution of the radiation mode amplitudes (top panel) and Stokes parameters (bottom three panels). The solid lines are for $\Gamma = 0.3$ and the dashed lines for $\Gamma = 0.1$. The polarization limiting radius is shown as the vertical dotted line. The initial values (at a small $x = x_i$) are $\mathcal{A}_{\rm O} = 1$, $\mathcal{A}_{\rm X} = 0$, $Q = I = 1$, $U = 0$ and $V = 0$. At distances $x \lesssim 0.5$, the modes evolve adiabatically. At $r \sim r_{\rm pl}$ the modes begin to couple, generating appreciable circular polarization. At $x \gtrsim 2$, the values of the Stokes parameters are "frozen."

is the linear polarization fraction just outside the atmosphere [see eq. (4.24)]. Since the radiation emerging from the NS surface is linearly polarized, we set $V(r_i) = 0$. Equations (4.32)-(4.35) are then integrated to a distance beyond $r_{\rm pl}$.

For a given initial value of the linear polarization fraction Π_{em} at a small $r_i \ll r_{\rm pl}$, the solution of eqs. (4.33)-(4.35) depends only on the dimensionless parameter $\Gamma \equiv r_{\rm pl}\varphi'_B$. Again, if we define $x = r/r_{\rm pl}$, eqs. (4.33)-(4.35) can be rewritten as

$$dQ/dx = \frac{2\Gamma}{x^6}\, V\, \sin 2\varphi_B, \tag{4.36}$$

$$dU/dx = -\frac{2\Gamma}{x^6}\, V\, \cos 2\varphi_B, \tag{4.37}$$

$$dV/dx = -\frac{2\Gamma}{x^6}\, (Q\, \sin 2\varphi_B - U\, \cos 2\varphi_B)\,, \tag{4.38}$$

with $\varphi_B = \Gamma(x - x_i)$. We are interested in the value of V at $x = x_f \gg 1$. Figure 4.5 shows some examples of the integration of Eqs. (4.36)-(4.38). Not surprisingly, the results are in exact agreement with those obtained using the mode evolution equations.

We have calculated the circular polarizations produced by rotating NSs with different values of Γ. Our numerical results [see Fig. (4.6)] show that the generated circular polarization is given by the expression

$$V/I \approx -0.60\, \Pi_{em}\, {\rm sign}(\varphi'_B)\, |r_{\rm pl}\, \varphi'_B|^{6/5} = -1.5 \times 10^{-3}\, \Pi_{em}\, \left(E_1\, B_{12}^2\, F_B\right)^{1/5}\, f_1\, F_\varphi. \tag{4.39}$$

This expression is accurate to within one percent in the regime $\Gamma \lesssim 0.4$ [see Fig. (4.6)]. Recall that $F_B \sim F_\varphi \sim 1$, so eq. (4.39) provides a quick estimate of the magnitude of circular polarization in NS surface emission.

Fig. 4.7 shows the observed, phase-resolved radiation Stokes parameters for a NS with $B = 10^{13}$ G and $T_{\rm eff} = 5 \times 10^6$ K, rotating at $f = 50$ Hz, with magnetic

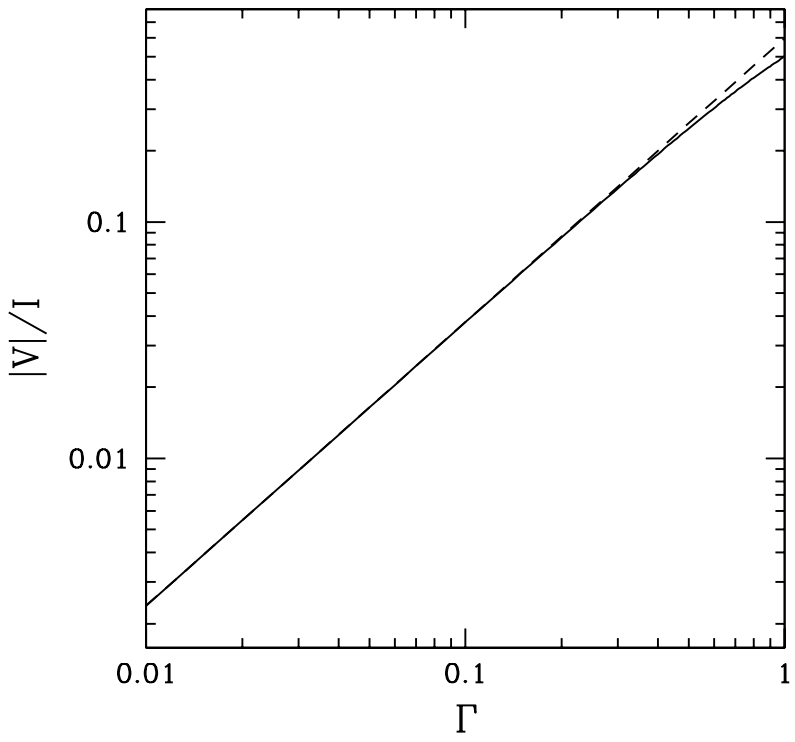

Figure 4.6: The magnitude of the observed circular polarization fraction $|V|/I$ as a function of Γ. The linear polarization fraction (Π_{em}) just outside the atmosphere is assumed to be 100%. The dashed line depicts the fitting formula, eq. (4.39), which agrees with the numerical solution to within 1% for $\Gamma < 0.4$. Note that solutions with $\Gamma \gtrsim 0.5$ are incorrect since the magnetic field around the polarization limiting radius is no longer described by the near-zone field of a rotating dipole as adopted in our calculations.

field and spin geometry $\gamma = 30°$, $\eta = 70°$ (this is the case shown in Fig. 4.1). The solid curves are numerical solutions to the Stokes parameter equations of transfer in the NS magnetosphere, while the dotted curves are calculated using the method described in §4.2. The latter method assumes $F_V = 0$, but yields results for F_Q and F_U that are quite close to those of the numerical integrations. For a rapidly rotating NS, substantial circular polarization is generated, with $|F_V/F_I|$ reaching $0.2 - 0.3$ in the hard X-ray band (see also Fig. 4.6). In contrast, Fig. 4.8 shows the same case with $f = 1$ Hz. In this case, negligible circular polarization is generated, and results from the two methods agree with each other exactly.

Finally, we note that although the specific results presented in this section refer to emission from a hot polar cap on the NS, we expect many of our key results (e.g., rotation of the planes of linear polarization between $E \lesssim 1$ keV and $E \gtrsim 4$ keV due to vacuum polarization for $B \lesssim 7 \times 10^{13}$ G) to be valid in more complicated models (when several hotspots or the whole stellar surface contribute to the X-ray emission). This is because the polarization-limiting radius (due to vacuum polarization in the magnetosphere) lies far from the star [see eq. 4.19], where rays originating from different patches of the NS experience the same dipole field (Heyl et al., 2003). Our results therefore demonstrate the unique potential of X-ray polarimetry to probe physics under extreme conditions (strong gravity and magnetic fields) and the nature of various forms of NSs.

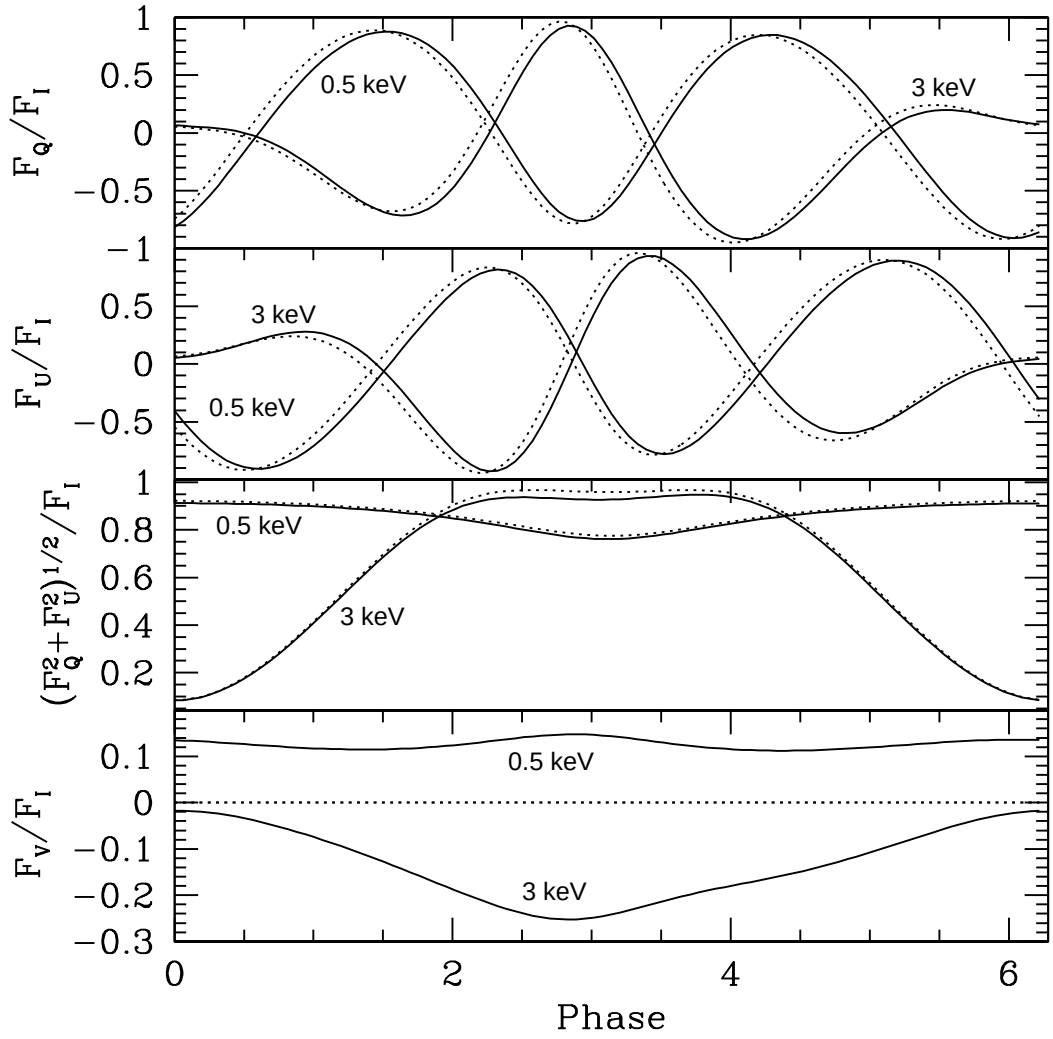

Figure 4.7: Observed radiation Stokes parameters for a NS with $B = 10^{13}$ G, $T_{\rm eff} = 5 \times 10^6$ K, $f = 50$ Hz, $\gamma = 30°$, and $\eta = 70°$, for photon energies $E = 0.5, 3$ keV. The solid curves show the results of numerical integration of the transfer equations for the Stokes parameters, while the dotted curves are calculated using the approximate method of § 4.2.

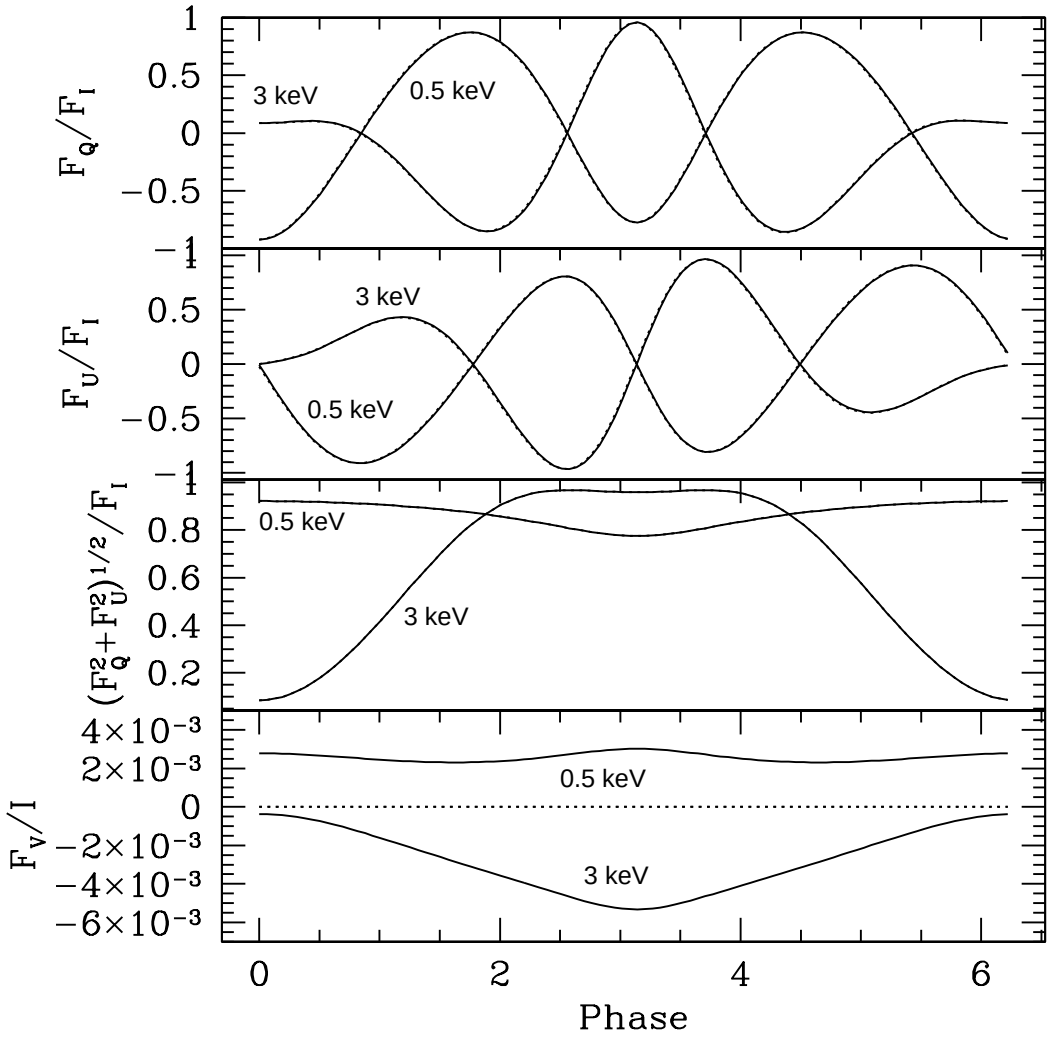

Figure 4.8: Same as Fig. 4.7, except for $f = 1$ Hz. For a slowly rotating NS, there is negligible difference between the results from the two methods.

Chapter 5

Discussion and Future Challenges for Atmosphere Modeling

We have presented a new method for incorporating partial conversion of photon modes due to vacuum polarization into fully-ionized, self-consistent atmosphere models of magnetized NSs. This method takes into account the non-trivial probability of photon mode conversion at the vacuum resonance. While recent works have clearly identified the important effects of the vacuum resonance and related mode conversion in determining atmosphere radiation spectra and polarizations (Lai & Ho, 2003a), so far the implementation of these effects in self-consistent atmosphere models, for technical reasons, has only considered two extreme limits: complete mode conversion and no mode conversion (Ho & Lai, 2003, 2004). With a direct, semi-explict Runga-Kutta integration of the radiative transfer equations for the photon modes (as opposed to the forward-backward substitution procedure of the Feautrier method) and with the use of an accurate mode conversion formula for each photon, our new atmosphere code displays excellent stability with respect to grid resolution. Moreover, integration of the full transfer equations for the radiation Stokes parameters shows that our treatment of partial conversion is accurate. As expected, the partial conversion solution is intermediate between the extreme cases of complete and no conversion considered previously. An accurate treatment of vacuum polarization is a critical step toward interpreting the spectra and predicting the polarization signals of magnetic NSs.

With our new atmosphere code, we have constructed a large number of atmosphere models for various magnetic field strengths, ranging from 10^{13} G to

5×10^{14} G, for both H and He compositions. In agreement with previous, approximate calculations (Ho & Lai, 2003, 2004), we find that for $B \gtrsim 7 \times 10^{13}$ G, the vacuum resonance affects the atmosphere spectra (the hard spectral tail is suppressed and the spectral line widths are reduced), with the effects becoming more significant as the magnetic field strength is increased. For $B \lesssim 7 \times 10^{13}$ G, the effect of the vacuum resonance on the spectra is smaller and becomes negligible for $B \lesssim 4 \times 10^{13}$ G. However, even for such "low" field strengths, vacuum resonace has a significant effect on the observed X-ray polarizations (see Lai & Ho, 2003b). Our new calculations presented in this paper are particularly important for the "intermediate" field regime ($4 \times 10^{13} \lesssim B \lesssim 2 \times 10^{14}$ G), where previous approximate treatments are inadequate. For the first time, we are able to accurately determine the B-dependence of the structure, spectra and polarization signals of ionized NS atmospheres.

Since the most time-consuming and difficult part of atmosphere modeling involves finding the atmosphere temperature profile that satisfies the condition of radiative equilibrium, for the convenience of the astrophysics community, we have presented fitting formulas for the temperature profiles of various atmosphere models (see §3.3.1). With these analytic expressions, it is relatively straightforward (using the procedure outlined in §3.2.1) to calculate various properties of the emergent radiation. These analytic profiles will also be useful for comparison with future theoretical atmosphere models.

We note that the models presented in this paper have several limitations: (1) The models assume that the magnetic field lies along the surface normal. While a more general magnetic field inclination does not change the main results of our paper (e.g. the effect of vacuum resonance and the dependence of the atmosphere

spectra on B), to confront observations, synthetic spectra must be constructed using realistic magnetic field and surface temperature distributions, adding up contributions over the entire NS surface. Such calculations are necessarily model-dependent, but they are needed for proper interpretation of observations. (2) At high density, the radiative transfer equation breaks down, due to the dense plasma effect. At large optical depth, the photon polarization develops a non-negligible longitudinal component, the index of refraction deviates significantly from unity, and the dielectric properties of the medium change. This occurs when the plasma frequency of the medium exceeds the photon frequency. To date, no detailed studies of the transfer of radiation in dense plasmas have been performed, though the problem has been treated in an ad-hoc way by Ho et al. (2003). Nevertheless, this effect is important for treating thermal radation in the optical band, and for magnetars can affect the emission spectrum in the soft X-ray ($\lesssim 1$ keV). (3) The assumption of fully ionized atmospheres may not be valid for cool NSs (such as the dim isolated NSs) or even the higher temperature AXPs and SGRs. Nevertheless, we expect features due to bound-bound and bound-free transitions of neutral species to be suppressed in the same manner as the ion cyclotron feature (see Ho et al., 2003; Potekhin et al., 2004, 2005, for recent works on partially ionized magnetic atmosphere models).

5.1 Implications for Observations of Isolated Neutron Stars

As mentioned in Chapter 1, recent observations by *Chandra* and *XMM-Newton* have shown that the quiescent thermal spectra from AXPs and SGRs have no observable absorption features (e.g., the ion cyclotron line at $E_{Bi} = 0.63(Z/A)B_{14}$ keV). As first pointed out by Ho & Lai (2003), and confirmed by our more accurate

calculations presented here, the inclusion of vacuum polarization effects provides a natural explanation for the non-detection: at $B = 5 \times 10^{14}$ G, the vacuum-suppressed width of the H or He cyclotron line is smaller than the current detector resolution. We expect that in the magnetar field regime, bound-bound and bound-free features will be similarly suppressed (see Ho et al. 2003; Potekhin et al. 2004).

Prominent absorption lines (at 0.7 keV and 1.4 keV) have been detected from the source 1E1207.4-520, a young neutron star ($T \simeq 2 \times 10^6$ K) associated with a supernova remnant (Sanwal et al., 2002; De Luca et al., 2005; Mori et al., 2005). Two viable (but tentative) identifications of these features are: (1) Ion cyclotron and atomic transitions of light-element (most likely He) atmospheres at $B \gtrsim 10^{14}$ G (Pavlov & Bezchastnov 2005); (2) Atomic transitions of C or O atmospheres with $B \lesssim 10^{12}$ G (Mori et al., 2005). Based on our general result of line suppression in the magnetar field regime, we suggest that the first interpretation is unlikely to be correct, although a quantitative calculation of the atomic line strengths is needed to draw a firm conclusion.

Absorption features have also been detected from three nearby, dim isolated NSs: RX J1308.6+2127, RX J1605.3+3249, and RX J0720.4-3125. While all three sources have similar effective temperatures ($T_{\rm eff} \sim 10^6$ K), their observed features occur at different energies and have varying equivalent widths: $E \approx 0.2 - 0.3$ keV with EW$\approx$ 150 eV for RX J1308.6+2127 (Haberl et al., 2003), $E \approx 0.27$ keV with EW$\approx$ 40 eV for RX J0720.4-3125 (Haberl et al., 2004b), and $E \approx 0.45$ keV with EW$\approx$ 80 eV for RX J1605.3+3249 (van Kerkwijk et al., 2004). With a single line, it is difficult to conclusively determine the atmosphere composition. One possibility is that these features are associated with proton cyclotron resonance (with possible blending from atomic transitions) in a H atmosphere (Ho & Lai

2004). For RX J1308.6+2127, the inferred magnetic field is $3-5\times10^{13}$ G, for which line suppression by vacuum resonance is ineffective. The broad width of the feature is consistent with that calculated by our H atmosphere models (see Fig. 3.10). RX J1605.3+3249 is also consistent with this picture: its feature corresponds to $B \sim 7 \times 10^{13}$ G, and partial suppression of the line may account for its lower (by a factor of ~ 2) EW (see Fig. 3.11). The situation for RX J0720.4-3125 is more complicated: its spectrum (including the line width) varies as a function of the rotation phase (Haberl et al., 2004b) and over a long timescale (a few years; see Haberl et al., 2006). If its absorption feature is a proton cyclotron line, then the inferred magnetic field is too low for vacuum polarization effects to alter the line strength. Its small EW (40 eV) could arise if the line-emitting region (where $B \lesssim 10^{14}$ G) is a small fraction of the NS surface; most of the surface would have $B \gtrsim 10^{14}$ G, requiring a highly non-dipolar surface field. Alternatively, if the atmosphere of RX J0720.4-3125 is composed of He, the required field strength is $B \sim 9 \times 10^{13}$ G, strong enough for the vacuum effects to reduce the line width.

Several recent papers have identified similar absorption features in other XDINSs, though these observations may require independent confirmation and better statistics. Haberl et al. (2004a) report spectral features for RX J0806.4-4123 ($E \approx 0.4 - 0.46$ keV; EW$\approx 33 - 56$) and RX J0420.0-5022 ($E \approx 0.3$ keV; EW≈ 45), while Zane et al. (2005) report a spectral feature for RX J2143.7+0654 ($E \approx 0.75$ keV; EW≈ 27). These features are similar to those described in more detail above, and suffer from the same difficulties of identification. Needless to say, since the magnetic field strengths of these NSs likely lie in the range $5 \times 10^{13} - 10^{14}$ G, for which accurate treatment of the vacuum resonance effect is crucial, the atmosphere models developed in this paper will be particularly useful, especially

when combined with detailed modeling of (phase-dependent) synthetic spectra and (energy-dependent) lightcurves.

5.2 Implications for Future Work

It is clear that further theoretical modeling of NS surface emission is needed to confront observations. Our discussion above also suggests that accurate theoretical models and high-quality data may still be inadequate to break some of the inherent degeneracies in magnetic field strength and geomery, atmosphere composition, and surface temperature distribution. In this regard, X-ray polarimetry is highly desirable. Our calculations in Chapter 4 show that polarization signals are complementary to X-ray spectra. In fact, the polarization signals from magnetars and NSs with moderate field strengths are qualitatively different. It is therefore possible for a NS with a typical spectrum and lightcurve to generate an interesting polarization signature.

Appendix A

Details of Condensed Surface Emission Calculation

A.1 Reflectivity Calculation

Here we fill in some of the details for the reflectivity calculation described in §2.2.2.

In the coordinate system xyz defined in §2.2.2, the explicit expression for eq. (2.12) is:

$$\begin{bmatrix} \epsilon\cos^2\theta_B + \eta\sin^2\theta_B + n_j^2(\sin^2\theta_j^{(t)}\cos^2\varphi - 1) & i\,g\cos\theta_B + \frac{1}{2}n_j^2\sin^2\theta_j^{(t)}\sin 2\varphi & \frac{1}{2}\left((\epsilon-\eta)\sin 2\theta_B + n_j^2\sin 2\theta_j^{(t)}\cos\varphi\right) \\ -i\,g\cos\theta_B + n_j^2\sin^2\theta_j^{(t)}\sin\varphi\cos\varphi & \epsilon + n_j^2(\sin^2\theta_j^{(t)}\sin^2\varphi - 1) & -i\,g\sin\theta_B + \frac{1}{2}n_j^2\sin 2\theta_j^{(t)}\sin\varphi \\ (\epsilon-\eta)\sin\theta_B\cos\theta_B + n_j^2\sin\theta_j^{(t)}\cos\theta_j^{(t)}\cos\varphi & i\,g\,\sin\theta_B + \frac{1}{2}n_j^2\sin 2\theta_j^{(t)}\sin\varphi & \epsilon\sin^2\theta_B + \eta\cos^2\theta_B - n_j^2\sin^2\theta_j^{(t)} \end{bmatrix} \cdot \begin{bmatrix} E_x \\ E_y \\ E_z \end{bmatrix} = \mathbf{0}, \tag{A.1}$$

where n_j (with $j = 1, 2$) is the index of refraction in the medium, and $\theta_j^{(t)}$ is the formal complex angle of propagation calculated using Snell's law (see Appendix A.2 for a discussion of the interpretation of complex $\theta_j^{(t)}$) . Taking the determinant of eq. (A.1) yields:

$$a_4 n_j^4 + a_2 n_j^2 + \cos\theta_j^{(t)}\sin\theta^{(i)}\left(a_1 n_j + a_3 n_j^3\right) + a_0 = 0, \tag{A.2}$$

where we have used Snell's law and the following definitions:

$$\begin{aligned} a_0 &= (\epsilon^2 - g^2)\eta + \frac{1}{8}\left[g^2 + \epsilon(\eta - \epsilon)\right]\left(2 + 6\cos 2\theta_B - 4\sin^2\theta_B \cos 2\varphi\right)\sin^2\theta^{(i)} \\ &\quad -2\left(\epsilon\cos^2\theta_B + \eta\sin^2\theta_B\right)\sin^2\varphi\sin^4\theta^{(i)} \qquad \text{(A.3a)} \\ a_1 &= \left[\epsilon(\eta - \epsilon) + g^2\right]\sin 2\theta_B\cos\varphi \qquad \text{(A.3b)} \\ a_2 &= \frac{1}{2}\left[g^2 - \epsilon(\epsilon + 3\eta) - (g^2 + \epsilon(\eta - \epsilon))\cos 2\theta_B\right] + \\ &\quad \left[\epsilon(\epsilon - \eta)\cos 2\theta_B + (\epsilon\cos^2\theta_B + \eta\sin^2\theta_B)\sin^2\varphi - \epsilon\cos^2\varphi\right]\sin^2\theta^{(i)} \qquad \text{(A.3c)} \\ a_3 &= (\epsilon - \eta)\sin 2\theta_B\cos\varphi \qquad \text{(A.3d)} \\ a_4 &= \left(\epsilon^2 - g^2\right)\eta. \qquad \text{(A.3e)} \end{aligned}$$

The $\cos\theta_j^{(t)}$ term is moved to the right-hand side, and the entire equation is then squared. Using the identity $\cos^2\theta_j^{(t)} = 1 - \sin^2\theta_j^{(t)}$ and Snell's law yields a polynomial equation in n_j:

$$\begin{aligned} a_4^2 n_j^8 \;+\; & (2a_2a_4 - a_3^2\sin^2\theta^{(i)})n_j^6 + (a_2^2 + 2a_0a_4 - 2a_1a_3\sin^2\theta^{(i)} + a_3^2\sin^4\theta^{(i)})n_j^4 + \\ & (2a_0a_2 - a_1^2\sin^2\theta^{(i)} + 2a_1a_3\sin^4\theta^{(i)})n_j^2 + a_0^2 + a_1^2\sin^4\theta^{(i)} = 0 \qquad \text{(A.4)} \end{aligned}$$

The polynomial equation (A.4) has eight roots for n_j which are found numerically using Laguerre's method (Press et al., 1992). Only two of the roots are physical and satisfy the original equation (A.2). In practice, it was found that for certain combinations of the parameters E, $\theta^{(i)}$, θ_B, φ, a spurious root satisfies eq. (A.2) to the specified degree of accuracy, resulting in an unphysical result for the reflectivity. It is often the case that such roots can be discounted physically using the conditions (A.11) and (A.12) (see Appendix A.2). Once the indices of refraction n_1, n_2 are known, the normal mode polarization vectors can be determined. Solving eq. (2.12)

for the ratios $f_j \equiv E_x^{(t)}/E_y^{(t)}$ and $g_j \equiv E_z^{(t)}/E_y^{(t)}$ results in the expressions

$$f_j = i\,\frac{\epsilon - i\,B_j\,g\sin\theta_B + n_j^2\sin\theta_j^{(t)}\sin\varphi\,C_j - n_j^2}{g\cos\theta_B + A_j\,g\sin\theta_B + i\,n_j^2\sin\theta_j^{(t)}D_j\sin\varphi}, \tag{A.5a}$$

$$g_j = A_j f_j + B_j, \tag{A.5b}$$

$$A_j = -\frac{\epsilon\cos^2\theta_B + \eta\sin^2\theta_B + n_j^2\sin^2\theta_j^{(t)}\cos^2\varphi}{(\epsilon-\eta)\sin\theta_B\cos\theta_B + n_j^2\sin\theta_j^{(t)}\cos\theta_j^{(t)}\cos\varphi}, \tag{A.5c}$$

$$B_j = -\frac{i\,g\cos\theta_B + n_j^2\sin\theta_j^{(t)}\sin\varphi\cos\varphi}{(\epsilon-\eta)\sin\theta_B\cos\theta_B + n_j^2\sin\theta_j^{(t)}\cos\theta_j^{(t)}\cos\varphi}, \tag{A.5d}$$

$$C_j = B_j\cos\theta_j^{(t)} + \sin\theta_j^{(t)}\sin\varphi, \tag{A.5e}$$

$$D_j = A_j\cos\theta_j^{(t)} + \sin\theta_j^{(t)}\cos\varphi. \tag{A.5f}$$

With the propagation modes in the plasma determined, the latter two equations of (2.14) give

$$\begin{pmatrix} \cos\theta^{(i)}\sin\varphi & \cos\varphi & C_1 & C_2 \\ \cos\theta^{(i)}\cos\varphi & \sin\varphi & -C_1 & -C_2 \\ -\cos\varphi & -\cos\theta^{(i)}\sin\varphi & C_5 & C_6 \\ -\sin\varphi & \cos\theta^{(i)}\cos\varphi & C_7 & C_8 \end{pmatrix} \cdot \left\{ \begin{pmatrix} r_{11} \\ r_{12} \\ t_{11} \\ t_{12} \end{pmatrix} \begin{pmatrix} r_{21} \\ r_{22} \\ t_{21} \\ t_{22} \end{pmatrix} \right\} = \left\{ \begin{pmatrix} -\cos\theta^{(i)}\sin\varphi \\ \cos\theta^{(i)}\cos\varphi \\ \cos\varphi \\ \sin\varphi \end{pmatrix} \begin{pmatrix} -\cos\varphi \\ -\sin\varphi \\ -\cos\theta^{(i)}\sin\varphi \\ \cos\theta^{(i)}\cos\varphi \end{pmatrix} \right\} \tag{A.6}$$

for the incoming polarization modes $\mathbf{e}_1^{(i)} = (-\cos\theta^{(i)}\cos\varphi, -\cos\theta^{(i)}\sin\varphi, \sin\theta^{(i)})$ and $\mathbf{e}_2^{(i)} = (\sin\varphi, -\cos\varphi, 0)$. Inverting the coefficient matrix of eq. (A.6) and performing extensive algebra yields the following expressions for the reflected field

amplitudes:

$$r_{11} = \frac{4A\cos\theta^{(i)} - 2B_-\sin^2\theta^{(i)} + (3+\cos 2\theta^{(i)})(B_+\cos 2\varphi + C_+\sin 2\varphi)}{4A\cos\theta^{(i)} + B_-(3+\cos 2\theta^{(i)}) - 2\sin^2\theta^{(i)}(B_+\cos 2\varphi + C_+\sin 2\varphi)}, \quad \text{(A.7a)}$$

$$r_{12} = \frac{4\cos\theta^{(i)}(C_- + B_+\sin 2\varphi - C_+\cos 2\varphi)}{4A\cos\theta^{(i)} + B_-(3+\cos 2\theta^{(i)}) - 2\sin^2\theta^{(i)}(B_+\cos 2\varphi + C_+\sin 2\varphi)}, \quad \text{(A.7b)}$$

$$r_{21} = \frac{4\cos\theta^{(i)}(C_+\cos 2\varphi - B_+\sin 2\varphi + C_-)}{4A\cos\theta^{(i)} + B_-(3+\cos 2\theta^{(i)}) - 2\sin^2\theta^{(i)}(B_+\cos 2\varphi + C_+\sin 2\varphi)}, \quad \text{(A.7c)}$$

$$r_{22} = \frac{(3+\cos 2\theta^{(i)})(B_+\cos 2\varphi + C_+\sin 2\varphi) - 4A\cos\theta^{(i)} - 2B_-\sin^2\theta^{(i)}}{4A\cos\theta^{(i)} + B_-(3+\cos 2\theta^{(i)}) - 2\sin^2\theta^{(i)}(B_+\cos 2\varphi + C_+\sin 2\varphi)}, \quad \text{(A.7d)}$$

using the definitions:

$$C_{1,2} = \left[1 + |f_{1,2}|^2 + |g_{1,2}|^2\right]^{-1/2}, \quad \text{(A.8a)}$$

$$C_{5,6} = C_{1,2}\left[n_{1,2}\,\sin\theta^{(t)}_{1,2}\,\cos\varphi\, g_{1,2} - n_{1,2}\,\cos\theta^{(t)}_{1,2}\, f_{1,2}\right], \quad \text{(A.8b)}$$

$$C_{7,8} = C_{1,2}\left[n_{1,2}\,\sin\theta^{(t)}_{1,2}\,\sin\varphi\, g_{1,2} - n_{1,2}\,\cos\theta^{(t)}_{1,2}\right], \quad \text{(A.8c)}$$

$$A = (C_6C_7 - C_5C_8), \quad \text{(A.8d)}$$

$$B_\pm = (C_2C_5 + C_2C_6) \pm (C_2C_7 - C_1C_8), \quad \text{(A.8e)}$$

$$C_\pm = (C_1C_6 + C_2C_5) \pm (C_2C_7 - C_1C_8). \quad \text{(A.8f)}$$

The reflectivity and the emission spectrum and polarization are then determined by eqs. (2.7), (2.8), and (2.9).

A.2 Complex Angle of Propagation

In this Appendix we outline some of the physical properties of a wave propagating in a plasma with complex index of refraction (c.f. §13.2 of Born & Wolf, 1980).

For a medium with complex index of refraction $n = n_R + in_I$ (where n_R and n_I are real), the formal refraction angle $\theta^{(t)}$, as determined by Snell's law, is complex. Let $\cos\theta^{(t)} = (1-\sin^2\theta^{(t)})^{1/2} = \cos\theta^{(t)}_R + i\cos\theta^{(t)}_I$. Defining the vector parallel to

the plane of incidence $\hat{\boldsymbol{s}} = (-\cos\varphi, -\sin\varphi, 0)$, the wavevector for the transmitted waves can be written:

$$\mathbf{k}^{(t)} = \frac{n\omega}{c}\left(\sin\theta^{(t)}\hat{\boldsymbol{s}} - \cos\theta^{(t)}\hat{\mathbf{z}}\right) = \frac{\omega}{c}\Big[\sin\theta^{(i)}\hat{\boldsymbol{s}} + (n_I\cos\theta_I^{(t)} - n_R\cos\theta_R^{(t)})\hat{\mathbf{z}} \\ -i(n_I\cos\theta_R^{(t)} + n_R\cos\theta_I^{(t)})\hat{\mathbf{z}}\Big] \quad \text{(A.9)}$$

The transmitted electric field has the form $E^{(t)} \propto e^{i\mathbf{k}^{(t)}\cdot\mathbf{r} - i\omega t}$. Substituting eq. (A.9) into this expression, the field takes the form:

$$\begin{aligned} E^{(t)} \quad \propto \quad & \exp\left[(n_R\cos\theta_I^{(t)} + n_I\cos\theta_R^{(t)})z\right] \times \\ & \exp\left[i\frac{\omega}{c}\left(\sin\theta^{(i)}s - (n_R\cos\theta_R^{(t)} - n_I\cos\theta_I^{(t)})z\right) - i\omega t\right]. \end{aligned} \quad \text{(A.10)}$$

Thus, the transmitted wave has a propagating component multiplied by a damping factor. Since the amplitude of the wave must decrease as it travels through the medium, eq. (A.10) gives the following condition on the index of refraction (recall that in the geometry of §2.2.2, $z < 0$):

$$n_R\cos\theta_I^{(t)} + n_I\cos\theta_R^{(t)} > 0. \quad \text{(A.11)}$$

The traveling component can be used to define a new wavevector $\mathbf{k}' = \sin\theta^{(i)}\hat{\boldsymbol{s}} - (n_R\cos\theta_R^{(t)} - n_I\cos\theta_I^{(t)})\hat{\mathbf{z}}$. The real angle of propagation is then given by $\cos\theta^{(t)'} = \hat{\mathbf{k}'}\cdot\mathbf{k}'/|\mathbf{k}'|$. By assumption, the angle of propagation for the refracted wave measured with respect to the z axis must be greater than $\pi/2$, yielding a second condition on the index of refraction:

$$-1 \leq \cos\theta^{(t)'} = \frac{n_I\cos\theta_I^{(t)} - n_R\cos\theta_R^{(t)}}{\sqrt{\sin^2\theta^{(i)} + (n_I\cos\theta_I^{(t)} - n_r\cos\theta_R^{(t)})^2}} \leq 0. \quad \text{(A.12)}$$

The real and imaginary parts of the indices of refraction for the birefringent transmitted waves must satisfy eqs. (A.11) and (A.12).

Appendix B

Thermal Conduction in Neutron Star Atmospheres

As discussed in Chapter 3, thermal conduction of electrons must be included in the calculation of atmospheric structure. Specifically, the condition of constant radiative flux, eq. (3.9), should be replaced by a constant total flux, $F_{\rm tot} = F_{\rm rad} + F_{\rm th}$, where $F_{\rm th}$ is the flux from thermal conduction of electrons. Due to the strongly quantizing nature of the magnetic field in the atmosphere models considered in §3.2, thermal conduction is strongly suppressed tranverse to the magnetic field. We therefore consider logitudinal conduction only.

Potekhin et al. (1999) provide calculations of electron thermal conductivity in arbitrary magnetic fields. To estimate the effects of thermal conduction on atmosphere structure, we use the classical Spitzer-Härm formula in our calculations, as a first approximation. For further discussion of calculations of thermal conductivities, see Potekhin et al. (1999) and the references therein.

The Spitzer-Härm formula for thermal conductive flux due to electrons is (Spitzer, 1962)

$$F_{\rm th} = -\lambda_{\rm C} T^{5/2} \frac{\partial T}{\partial z} \tag{B.1}$$

where $\lambda_{\rm C} = 1.8 \times 10^{-5}$ erg cm^{-1} s^{-1} K$^{-7/2}$. Using the fitting formulas from §3.3.1, $F_{\rm th}$ can be written as a function of Thomson optical depth:

$$F_{\rm th} = 5.23 \times 10^{16}\, T_6^{5/2} \left(c_2 + 2\, c_3\, \Delta x + 3\, c_4\, \Delta x^2 + 4\, c_5\, \Delta x^3 + 5\, c_6\, \Delta x^4\right) ({\rm cgs}), \tag{B.2}$$

where $c_j = a_j$ for $\tau > \tau_{\rm mid}$ and $c_j = b_j$ for $\tau < \tau_{\rm mid}$.

The radiative flux is given by

$$F_{\rm rad} = 5.67 \times 10^{19} \, (T_{\rm eff}/10^6 \text{ K})^4 \text{ erg cm}^{-2} \text{ s}^{-1} \tag{B.3}$$

Figure B.1 shows $F_{\rm th}/F_{\rm rad}$ as a function of optical depth for the H NS atmosphere models with $B = 4 \times 10^{14}$ G, $T_{\rm eff} = 10^6$ K and $B = 10^{14}$ G, $T_{\rm eff} = 5 \times 10^6$ K. For both models, the thermal conductive flux is a small fraction of the radiative flux (less than 1%) except in the deepest layers ($\tau > 10^3$).[1] We therefore conclude that thermal conduction provides a minor correction to the total flux and can be neglected in the calculations of Chapter 3.

It is possible, however, to envision scenarios in which $F_{\rm th}$ can become important. As discussed in Chapter 5, at large optical depth and magnetic field strength, the plasma frequency of the medium can exceed the photon frequency in the optical and X-ray bands. In a such case, we expect the radiative flux to be suppressed, and the conductive flux may supply the bulk of $F_{\rm tot}$. When atmosphere models take this effect into account, it may become necessary to revisit the problem of thermal conduction in NS atmospheres in more detail.

[1]Note that the negative values of $F_{\rm th}$ around $\tau \sim 10^2$ for the $T_{\rm eff} = 5 \times 10^6$ K model result from the inversion of the temperature profile due to the extra heat deposited by X-mode photons at the vacuum resonance.

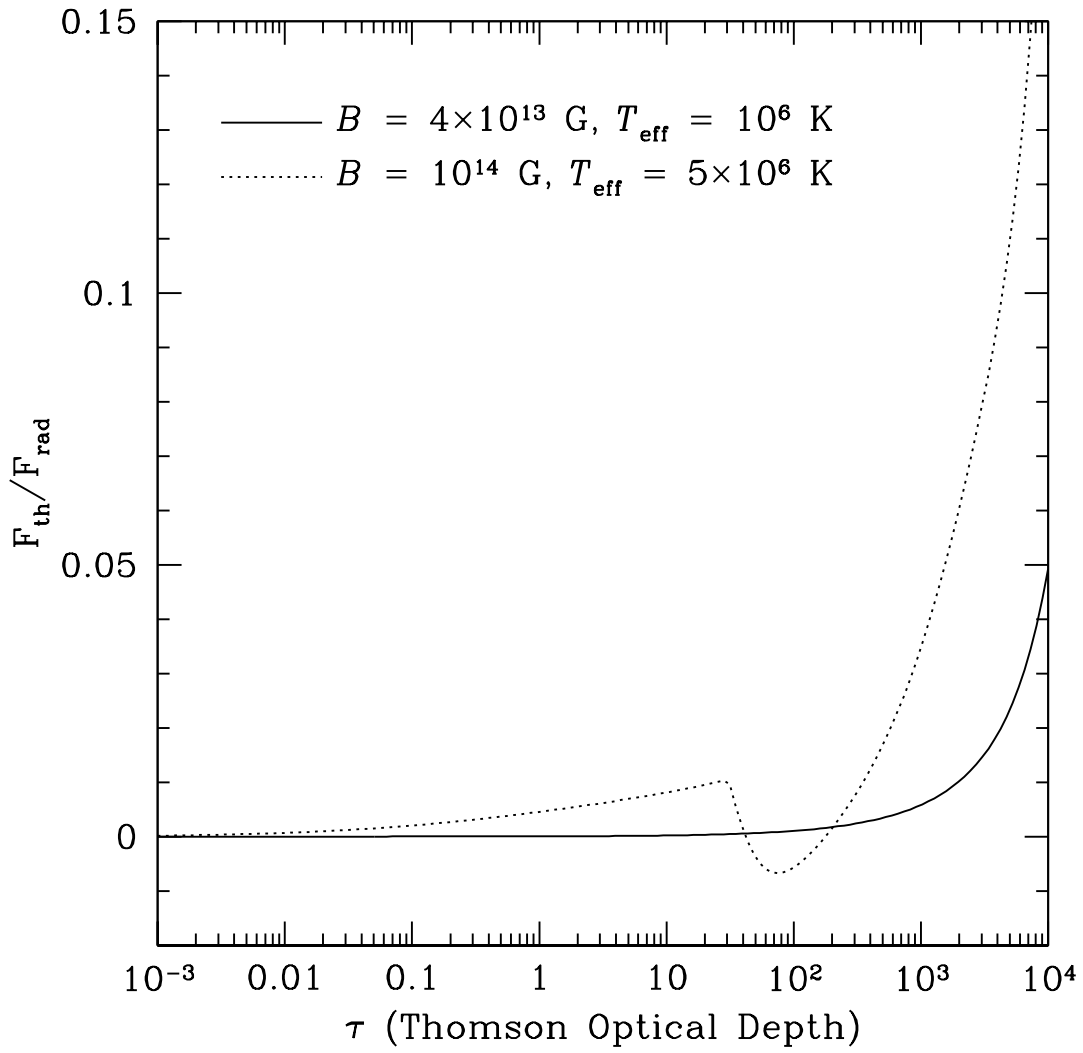

Figure B.1: Ratio of thermal conductive flux to radiative flux for H NS atmosphere models with $B = 4 \times 10^{13}$ G, $T_{\rm eff} = 10^6$ K and $B = 10^{14}$ G, $T_{\rm eff} = 5 \times 10^6$ K. The conductive flux is a small fraction of the total flux except in the deepest layers ($\tau > 10^3$).

REFERENCES

Agüeros, M. A., Anderson, S. F., Margon, B., Posselt, B., Haberl, F., Voges, W., Annis, J., Schneider, D. P., & Brinkmann, J. 2006, AJ, 131, 1740

Ashcroft, N. & Mermin, D. 1976, Solid State Physics (New York: Rinehart and Winston)

Becker, W. & Pavlov, G. G. 2002, preprint (astro-ph/0208356)

Beloborodov, A. M. 2002, ApJ, 566, L85

Blaes, O. & Madau, P. 1993, ApJ, 403, 690

Born, M. & Wolf, E. 1980, Principles of optics. Electromagnetic theory of propagation, interference and diffraction of light (Oxford, UK: Pergamon Press)

Braje, T. M. & Romani, R. W. 2002, ApJ, 580, 1043

Brinkmann, W. 1980, A&A, 82, 352

Bulik, T. & Miller, M. C. 1997, MNRAS, 288, 596

Burwitz, V., Haberl, F., Neuhäuser, R., Predehl, P., Trümper, J., & Zavlin, V. E. 2003, A&A, 399, 1109

Burwitz, V., Zavlin, V. E., Neuhäuser, R., Predehl, P., Trümper, J., & Brinkman, A. C. 2001, A&A, 379, L35

Canuto, V. & Ventura, J. 1972, Ap&SS, 18, 104

Caraveo, P. A., De Luca, A., Mereghetti, S., Pellizzoni, A., & Bignami, G. F. 2004, Science, 305, 376

Chabrier, G. 1993, ApJ, 414, 695

Cline, T. L., Mazets, E. P., & Golenetskii, S. V. 1998, IAUC, 7002, 1

Costa, E., Bellazzini, R., Soffitta, P., di Persio, G., Feroci, M., Morelli, E., Muleri, F., Pacciani, L., Rubini, A., Baldini, L., Bitti, F., Brez, A., Cavalca, F., Latronico, L., Massai, M. M., Omodei, N., Sgro', C., Spandre, G., Matt, G., Perola, G. C., Santangelo, A., Celotti, A., Barret, D., Vilhu, O., Piro, L., Fraser, G., Courvoisier, T. J. ., & Barcons, X. 2006, preprint (astro-ph/0603399)

Costa, E., Soffitta, P., Bellazzini, R., Brez, A., Lumb, N., & Spandre, G. 2001, Nature, 411, 662

De Luca, A., Caraveo, P. A., Mereghetti, S., Negroni, M., & Bignami, G. F. 2005, ApJ, 623, 1051

de Vries, C. P., Vink, J., Méndez, M., & Verbunt, F. 2004, A&A, 415, L31

Drake, J. J., Marshall, H. L., Dreizler, S., Freeman, P. E., Fruscione, A., Juda, M., Kashyap, V., Nicastro, F., Pease, D. O., Wargelin, B. J., & Werner, K. 2002, ApJ, 572, 996

Duncan, R. C. & Thompson, C. 1992, ApJ, 392, L9

Evans, D., Kiebesadel, R., Baros, J., Cline, T., Desai, U., Teegarden, B., Pizzichini, G., Hurley, K., Niel, M., Vedrenne, G., Estulin, I. V., & Mazets, E. P. 1979, IAUC, 3356, 1

Flowers, E. G., Ruderman, M. A., Lee, J.-F., Sutherland, P. G., Hillebrandt, W., & Mueller, E. 1977, ApJ, 215, 291

Gavriil, F. P., Kaspi, V. M., & Woods, P. M. 2002, Nature, 419, 142

Ginzburg, V. 1970, Propagation of Electromagnetic Waves in Plasmas (Oxford: Pergamon Press)

Gnedin, I. N. & Sunyaev, R. A. 1974, A&A, 36, 379

Gnedin, Y. & Pavlov, G. 1974, Sov. Phys. JETP, 38, 903

Gnedin, Y. N., Pavlov, G. G., & Shibanov, Y. A. 1978, Soviet Astronomy Letters, 4, 117

GöğüŞ , E., Woods, P. M., Kouveliotou, C., van Paradijs, J., Briggs, M. S., Duncan, R. C., & Thompson, C. 1999, ApJ, 526, L93

Haberl, F. 2005, in 5 years of Science with XMM-Newton, ed. U. G. Briel, S. Sembay, & A. Read, 39–44

Haberl, F., Motch, C., Buckley, D. A. H., Zickgraf, F., & Pietsch, W. 1997, A&A, 326, 662

Haberl, F., Motch, C., Zavlin, V. E., Reinsch, K., Gänsicke, B. T., Cropper, M., Schwope, A. D., Turolla, R., & Zane, S. 2004a, A&A, 424, 635

Haberl, F., Schwope, A. D., Hambaryan, V., Hasinger, G., & Motch, C. 2003, A&A, 403, L19

Haberl, F., Turolla, R., de Vries, C. P., Zane, S., Vink, J., Méndez, M., & Verbunt, F. 2006, A&A, 451, L17

Haberl, F., Zavlin, V. E., Trümper, J., & Burwitz, V. 2004b, A&A, 419, 1077

Heyl, J. S. & Hernquist, L. 1997, PhRvD, 55, 2449

Heyl, J. S. & Shaviv, N. J. 2002, PhRvD, 66, 3002

Heyl, J. S., Shaviv, N. J., & Lloyd, D. 2003, MNRAS, 342, 134

Ho, W. C. G. & Lai, D. 2001, MNRAS, 327, 1081

—. 2003, MNRAS, 338, 233

—. 2004, ApJ, 607, 420

Ho, W. C. G., Lai, D., Potekhin, A. Y., & Chabrier, G. 2003, ApJ, 599, 1293

Hurley, K., Boggs, S. E., Smith, D. M., Duncan, R. C., Lin, R., Zoglauer, A., Krucker, S., Hurford, G., Hudson, H., Wigger, C., Hajdas, W., Thompson, C., Mitrofanov, I., Sanin, A., Boynton, W., Fellows, C., von Kienlin, A., Lichti, G., Rau, A., & Cline, T. 2005, Nature, 434, 1098

Ibrahim, A. I., Safi-Harb, S., Swank, J. H., Parke, W., Zane, S., & Turolla, R. 2002, ApJ, 574, L51

Ibrahim, A. I., Swank, J. H., & Parke, W. 2003, ApJ, 584, L17

Israel, G., Stella, L., Covino, S., Campana, S., Angelini, L., Mignani, R., Mereghetti, S., Marconi, G., & Perna, R. 2004, in IAU Symposium, ed. F. Camilo & B. M. Gaensler, 247

Itoh, N. 1975, MNRAS, 173, 1P

Jackson, M. S. & Halpern, J. P. 2005, ApJ, 633, 1114

Jones, P. B. 1986, MNRAS, 218, 477

Kadomtsev, B. 1970, Sov. Phys. JETP, 31, 945

Kaminker, A. D., Yakovlev, D. G., & Gnedin, O. Y. 2002, A&A, 383, 1076

Kaplan, D. 2005, private communication

Kaplan, D. L., van Kerkwijk, M. H., & Anderson, J. 2002, ApJ, 571, 447

Kaplan, D. L., van Kerkwijk, M. H., Marshall, H. L., Jacoby, B. A., Kulkarni, S. R., & Frail, D. A. 2003, ApJ, 590, 1008

Kaspi, V. M. 2004, in IAU Symposium, ed. F. Camilo & B. M. Gaensler, 231

Kaspi, V. M., Gavriil, F. P., Woods, P. M., Jensen, J. B., Roberts, M. S. E., & Chakrabarty, D. 2003, ApJ, 588, L93

Kouveliotou, C., Dieters, S., Strohmayer, T., van Paradijs, J., Fishman, G. J., Meegan, C. A., Hurley, K., Kommers, J., Smith, I., Frail, D., & Murakami, T. 1998, Nature, 393, 235

Kouveliotou, C., Strohmayer, T., Hurley, K., van Paradijs, J., Finger, M. H., Dieters, S., Woods, P., Thompson, C., & Duncan, R. C. 1999, ApJ, 510, L115

Kuiper, L., Hermsen, W., den Hartog, P. R., & Collmar, W. 2006, ApJ, 645, 556

Kuiper, L., Hermsen, W., & Mendez, M. 2004, ApJ, 613, 1173

Kulkarni, S. R., Kaplan, D. L., Marshall, H. L., Frail, D. A., Murakami, T., & Yonetoku, D. 2003, ApJ, 585, 948

Lai, D. 2001, Reviews of Modern Physics, 73, 629

Lai, D. & Ho, W. 2003a, Physical Review Letters, 91, 1101

Lai, D. & Ho, W. C. G. 2002, ApJ, 566, 373

—. 2003b, ApJ, 588, 962

Lai, D. & Salpeter, E. E. 1997, ApJ, 491, 270

Lattimer, J. M. & Prakash, M. 2001, ApJ, 550, 426

Lattimer, J. M., Prakash, M., Pethick, C. J., & Haensel, P. 1991, Physical Review Letters, 66, 2701

Lenzen, R. & Truemper, J. 1978, Nature, 271, 216

Marshall, H. L. & Schulz, N. S. 2002, ApJ, 574, 377

McLaughlin, M. A., Lyne, A. G., Lorimer, D. R., Kramer, M., Faulkner, A. J., Manchester, R. N., Cordes, J. M., Camilo, F., Possenti, A., Stairs, I. H., Hobbs, G., D'Amico, N., Burgay, M., & O'Brien, J. T. 2006, Nature, 439, 817

McLaughlin, M. A., Stairs, I. H., Kaspi, V. M., Lorimer, D. R., Kramer, M., Lyne, A. G., Manchester, R. N., Camilo, F., Hobbs, G., Possenti, A., D'Amico, N., & Faulkner, A. J. 2003, ApJ, 591, L135

Medin, Z. & Lai, D. 2006, preprint (astro-ph/0607277)

Meszaros, P. 1992, High-energy radiation from magnetized neutron stars (Chicago: University of Chicago Press)

Meszaros, P., Novick, R., Szentgyorgyi, A., Chanan, G. A., & Weisskopf, M. C. 1988, ApJ, 324, 1056

Meszaros, P. & Ventura, J. 1979, PhRvD, 19, 3565

Mihalas, D. 1978, Stellar atmospheres (San Francisco: W. H. Freeman and Co.)

Mori, K., Chonko, J. C., & Hailey, C. J. 2005, ApJ, 631, 1082

Mori, K. & Hailey, C. J. 2002, ApJ, 564, 914

—. 2003, (preprint (astro-ph/0301161)

Mori, K. & Ruderman, M. A. 2003, ApJ, 592, L75

Motch, C., Sekiguchi, K., Haberl, F., Zavlin, V. E., Schwope, A., & Pakull, M. W. 2005, A&A, 429, 257

Motch, C., Zavlin, V. E., & Haberl, F. 2003, A&A, 408, 323

Mueller, E. 1984, A&A, 130, 415

Neuhauser, D., Koonin, S. E., & Langanke, K. 1987, PhRvA, 36, 4163

Ogata, S. & Ichimaru, S. 1990, PhRvA, 42, 4867

Ogelman, H. 1995, in ASP Conf. Ser. 72: Millisecond Pulsars. A Decade of Surprise, ed. A. S. Fruchter, M. Tavani, & D. C. Backer, 309

Özel, F. 2001, ApJ, 563, 276

—. 2003, ApJ, 583, 402

Paczynski, B. 1992, Acta Astronomica, 42, 145

Paerels, F., Mori, K., Motch, C., Haberl, F., Zavlin, V. E., Zane, S., Ramsay, G., Cropper, M., & Brinkman, B. 2001, A&A, 365, L298

Pavlov, G. G. & Bezchastnov, V. G. 2005, ApJ, 635, L61

Pavlov, G. G., Sanwal, D., & Teter, M. A. 2004, in IAU Symposium, ed. F. Camilo & B. M. Gaensler, 239

Pavlov, G. G. & Shibanov, I. A. 1979, Zhurnal Eksperimental noi i Teoreticheskoi Fiziki, 76, 1457

Pavlov, G. G., Shibanov, I. A., & Iakovlev, D. G. 1980, Ap&SS, 73, 33

Pavlov, G. G., Shibanov, Y. A., Zavlin, V. E., & Meyer, R. D. 1995, in Proceedings of the NATO Advanced Study Institute on the Lives of the Neutron Stars, ed. M. A. Alpar, U. Kiziloglu, & J. van Paradijs, Boston, 71

Pavlov, G. G. & Zavlin, V. E. 2000, ApJ, 529, 1011

Pavlov, G. G. & Zavlin, V. E. 2003, in Texas in Tuscany. XXI Symposium on Relativistic Astrophysics, ed. R. Bandiera, R. Maiolino, & F. Mannucci, 319–328

Pavlov, G. G., Zavlin, V. E., & Sanwal, D. 2002, in Neutron Stars, Pulsars, and Supernova Remnants, ed. W. Becker, H. Lesch, & J. Trümper, 273

Pechenick, K. R., Ftaclas, C., & Cohen, J. M. 1983, ApJ, 274, 846

Pons, J. A., Walter, F. M., Lattimer, J. M., Prakash, M., Neuhäuser, R., & An, P. 2002, ApJ, 564, 981

Popov, S. B., Turolla, R., & Possenti, A. 2006, MNRAS, 369, L23

Potekhin, A. 2006, private communication

Potekhin, A. Y. 1999, A&A, 351, 787

Potekhin, A. Y. & Chabrier, G. 2000, PhRvE, 62, 8554

—. 2003, ApJ, 585, 955

—. 2004, ApJ, 600, 317

Potekhin, A. Y., Chabrier, G., & Shibanov, Y. A. 1999, PhRvE, 60, 2193

Potekhin, A. Y., Lai, D., Chabrier, G., & Ho, W. C. G. 2004, ApJ, 612, 1034

—. 2005, Advances in Space Research, 35, 1158

Prakash, M., Prakash, M., Lattimer, J. M., & Pethick, C. J. 1992, ApJ, 390, L77

Press, W. H., Teukolsky, S. A., Vetterling, W. T., & Flannery, B. P. 1992, Numerical recipes in C. The art of scientific computing (Cambridge, UK: Cambridge University Press)

Rajagopal, M. & Romani, R. W. 1996, ApJ, 461, 327

Rea, N., Israel, G. L., Stella, L., Oosterbroek, T., Mereghetti, S., Angelini, L., Campana, S., & Covino, S. 2003, ApJ, 586, L65

Ruderman, M. 1971, Physical Review Letters, 27, 1306

Sanwal, D., Pavlov, G. G., Zavlin, V. E., & Teter, M. A. 2002, ApJ, 574, L61

Shibanov, I. A., Zavlin, V. E., Pavlov, G. G., & Ventura, J. 1992, A&A, 266, 313

Slane, P., Smith, R. K., Hughes, J. P., & Petre, R. 2002, ApJ, 564, 284

Spitzer, L. 1962, Physics of Fully Ionized Gases (New York: Interscience)

Strohmayer, T. E. & Ibrahim, A. I. 2000, ApJ, 537, L111

Thompson, C. & Duncan, R. C. 1995, MNRAS, 275, 255

—. 1996, ApJ, 473, 322

Treves, A. & Colpi, M. 1991, A&A, 241, 107

Treves, A., Turolla, R., Zane, S., & Colpi, M. 2000, PASP, 112, 297

Trümper, J. E., Burwitz, V., Haberl, F., & Zavlin, V. E. 2004, Nuclear Physics B Proceedings Supplements, 132, 560

Turolla, R., Zane, S., & Drake, J. J. 2004, ApJ, 603, 265

Usov, N., Grebenschikov, Y., & Ulinich, F. 1980, Sov. Phys. JETP, 51, 148

van Kerkwijk, M. H., Kaplan, D. L., Durant, M., Kulkarni, S. R., & Paerels, F. 2004, ApJ, 608, 432

van Kerkwijk, M. H. & Kulkarni, S. R. 2001, A&A, 380, 221

Ventura, J. 1979, PhRvD, 19, 1684

Ventura, J., Nagel, W., & Meszaros, P. 1979, ApJ, 233, L125

Walter, F. M. & Matthews, L. D. 1997, Nature, 389, 358

Walter, F. M., Wolk, S. J., & Neuhauser, R. 1996, Nature, 379, 233

Woods, P. M., Kouveliotou, C., Göğüş, E., Finger, M. H., Swank, J., Markwardt, C. B., Hurley, K., & van der Klis, M. 2002, ApJ, 576, 381

Woods, P. M. & Thompson, C. 2004, preprint (astro-ph/0406133)

Yakovlev, D. G., Gnedin, O. Y., Kaminker, A. D., Levenfish, K. P., & Potekhin, A. Y. 2004, Advances in Space Research, 33, 523

Yakovlev, D. G. & Pethick, C. J. 2004, ARA&A, 42, 169

Zane, S., Cropper, M., Turolla, R., Zampieri, L., Chieregato, M., Drake, J. J., & Treves, A. 2005, ApJ, 627, 397

Zane, S., Turolla, R., Stella, L., & Treves, A. 2001, ApJ, 560, 384

Zane, S., Turolla, R., & Treves, A. 2000, ApJ, 537, 387

Zavlin, V. E. & Pavlov, G. G. 2002, in Neutron Stars, Pulsars, and Supernova Remnants, ed. W. Becker, H. Lesch, & J. Trümper, 263

Zavlin, V. E., Pavlov, G. G., & Trumper, J. 1998, A&A, 331, 821

Ziman, J. M. 1979, Principles of the Theory of Solids (Cambridge, UK: Cambridge University Press)